Lagrangian observations and numerical modelling of hydrodynamics, turbulence, and sediment transport in a tidal river

A thesis

submitted in fulfilment

of the requirements for the Degree

of

Doctor of Philosophy in Earth Sciences

at

The University of Waikato

by

Bérengère S. Dejeans

THE UNIVERSITY OF
WAIKATO
Te Whare Wānanga o Waikato

2023

Abstract

Fluvial-to-marine transition zones in rivers play a critical role in transporting materials, including nutrients and sediments, from land to ocean. These riverine environments located close to estuaries constitute complex dynamical systems, which are affected by the influences of both tidal variations from downstream and freshwater inputs from upstream, with the interaction of multiple physical processes controlling velocities, salinities, mixing, and sediment transport. As such, accurate numerical modelling of the hydrodynamics and sediment movement in these regions can prove challenging. However, it is essential to address this challenge as models are now regularly utilised as a tool to underpin coastal management projects, such as predicting pollutant dispersal, assessing navigability, or undertaking hazard management. Turbulence has been shown to influence many processes involved in the movement of particles and, particularly, sediment transport. Turbulence is notably a key control of flocculation processes (aggregation and disaggregation) of fine cohesive particles in suspension, in particular in marine settings. The variability of turbulence along a stretch of river affects the size of flocs, and thus also the settling velocity and movement of sediment within the water column.

In this thesis, I use numerical modelling to explore hydrodynamics, turbulence, and sediment transport processes within the tidally driven, heavily sediment-laden and meandering Kaipara River, New Zealand. In particular, I investigate the performance of Delft3D-FLOW in modelling flow speeds, turbulence, and sediment transport along a 15-km stretch of the tidally influenced river in a Lagrangian (flow-following) frame of reference by comparing predictions to a unique Lagrangian dataset which offers exceptional spatial resolution

of quantities along the river. Specifically, I examine (1) the ability of the model to reproduce the Lagrangian observations with the commonly used k-ϵ turbulence closure scheme, (2) a comparison of model predictions of hydrodynamics when two turbulence closure schemes are implemented, namely k-ϵ and k-L and (3) the Lagrangian dynamics of sediment transport along the river.

Lagrangian observations and modelling of turbulence along a tidally influenced river

Lagrangian datasets of hydrodynamic and sediment variables were collected along a 15 km-stretch of the river during the ebb tide using 'FlocDrifter' platforms, deployed from different locations. Two platforms were also fixed in an Eulerian frame-of-reference, collecting time series upstream of the river and towards the middle of the studied domain. Delft3D was used, with the two-equation k-ϵ turbulence closure scheme to simulate flows along the river. The model calibration was classified as excellent when predictions were compared with Eulerian measurements; however, on comparison of model predictions with the Lagrangian observations, discrepancies were revealed. Overall, the model could predict flow speeds and the general patterns and the right order of magnitude of dissipation rates of turbulent kinetic energy ϵ along the river. Nevertheless, the model did not always correctly reproduce the observed ϵ, particularly around abrupt meander bends. While such errors in ϵ could be partially connected to errors in predictions of speeds, the omission or the lack of accuracy of other processes (e.g., wind-driven mixing, secondary flow) were likely to explain some of the errors in model predictions. Overlaps in the drifter tracks indicated that the bathymetry and the geometry of the river were the primary controls on the along-river structure of flow and turbulence. The vertical and cross-sectional distributions of dissipation rates of turbulent kinetic energy, turbulent kinetic energy and vertical eddy viscosity were examined and showed that, generally, turbulence varied more in the vertical direction rather than the longitudinal direction, in agreement with previous studies. Overall,

results demonstrated that the flow-following Lagrangian observations allowed identification of variability across multiple length and time scales, which would not necessarily be captured using an Eulerian frame of reference. Moreover, the comparison with Lagrangian observations offers a more stringent validation of model results over large (riverine) spatial scales than a traditional Eulerian approach.

Evaluation of the performance of two turbulence closure schemes in a Lagrangian frame of reference along a fluvial-to-marine transition zone

The well-known 'closure problem' of turbulence means that numerical computation of turbulent quantities requires assumptions and simplifications of the flow dynamics. Statistical approaches, which have been found to be relatively computationally efficient, are commonly used. These approaches are based on the Reynolds-Averaged Navier-Stokes (RANS) equations, which are usually first simplified, and then solved through use of a turbulent closure scheme. This work compares numerical model predictions of flow speeds and dissipation rates of turbulent kinetic energy to a unique set of Lagrangian observations, collected along a meandering tidal river (the Kaipara River in the North Island of New Zealand). Two turbulence closures schemes (the k-L and the k-ϵ schemes) are implemented in the model, with both producing very similar predictions. Indeed, both the one-equation k-L and the two-equation k-ϵ turbulence closure schemes could reproduce the overall along-river structure and the right order of magnitude of flow speeds and ϵ. Nevertheless, the smaller-scale patterns were not accurately captured by either closure scheme, with larger differences to observations occurring at bends. Moreover, the k-L turbulence closure scheme performed slightly better than the k-ϵ turbulence closure scheme in predicting the along-river changes in dissipation rates of turbulent kinetic energy. This result suggests that, while most modelling studies use the 'default' more sophisticated formulation for turbulence closure, sim-

pler closure schemes can perform similarly and sometimes better, hence saving computational resources.

Controls on the flow-following distribution of suspended sediment concentrations in a tidally driven river

Sediment movement, deposition, and erosion within rivers and coastal environments are complex physical processes which vary widely depending on forcing regimes; however, accurate representation of these processes in numerical models is crucial to predict the geomorphological evolution of these regions. We use observations and numerical modelling to explore the controls on the distribution of suspended sediment concentration along a tidal river. Model runs with variable implementations of advection, erosion, and deposition processes revealed that the main source of suspended sediments was resuspension from the river bed, rather than advection from upstream which formed a smaller secondary contribution. The comparison with the high-resolution Lagrangian dataset provided a particularly strenuous test of model performance, and the model was found to do an excellent job of reproducing the rate and magnitude of the downstream increase in SSCs, especially when considering a number of simplifications made in model setup and boundary conditions. While patterns were very similar, small (5 %) differences in the predictions of SSC were found between the k-ϵ and k-L closure schemes. Abrupt local increases in SSC were observed in transitions from bends to straight sections of the river, and conversely, sudden local decreases in SSC were observed on the entrance to bends. These flow-following changes in SSC over medium spatial scales (O(km)) were found to be strongly correlated with shear velocities within the model. However, some of the km-scale variability seen in the observations was not reproduced by the model, with differences in these cases attributed to other physical processes which were not incorporated (e.g., additional freshwater inputs and wind- or wave-driven resuspension). Model predictions remained remarkably reliable even for locations where flocs were present in the obser-

vations, despite not including a parameterisation for the flocculation process. Results indicated that conditions were sufficiently energetic (shear velocities $\gg$ floc settling velocities) to prevent settling of even the larger flocs.

Acknowledgements

This PhD journey would not have been possible without the support of many people.

First of all, I would like to express my deepest gratitude to my chief supervisor Associate Professor Julia Mullarney, without who this endeavor would not have been possible. I will never be able to express how grateful I am for all of her support in every aspect of this journey. Secondly, I would like to express my deepest appreciation to my second supervisor, Dr Iain MacDonald, whose support was also crucial to this thesis.

I am also thankful to NIWA for funding this project.

I would like to extend many thanks to Glen Reeve for helping with the numerical model and field work. I also would like to thank Dave Bremner, Rod Budd, Scott Edhouse, Sam Parkes, and Mark Pritchard for providing assistance with the field work. I also would like to thank Mark Pritchard for his help with the model.

I am thankful to Callum Walley and Anthony Shaw for their help with the use of NeSI.

I also would like to extend my sincere thanks to Karin Bryan, Conrad Pilditch and Shari Gallop for their support.

I would like to express my great appreciation for the administration support at the university, especially Vicki and Fiona.

This PhD journey has been anything but a smooth ride and, although I am the main author, I could never have done it without the support of many people. I was told that doing a PhD was hard and it has been! What I had

not realized before undertaking this journey was that life around you never stops, and keeping a balance has proved at times impossible for me. However, instead of giving up on me, some people have carried me and helped me more than I ever expected. Words will never be able to express how grateful I am to those people... Although it is not possible for me to rank their support, I want to express my most sincere thank to Hannah Julian. I also want to extend my gratitude for their invaluable help to Julia Mullarney, Danielle, Courtney, Erik, Victor, Peter, Anna-Lena, Karin Bryan and Dennis, to name a few.

I also want to thank my friends not only for putting up with me but also for their continued support, especially Reza, Hannah, Danielle, Chloe, Marianne, Nasim, Liam, and Danche. I want to express a special thank you to Regan and his wife for their extreme generosity.

I want to say a huge thank you to all of the Coastal Marine Group over the years, including Victor, Peter, Ben, Ben, Mariana, Zhanchao, Wagner, Hemanth, Vinay, Amin, Sanne, Shahab, Steph, Vera and John.

Last but not least, I want to express my greatest thanks to my parents and brothers, for their unconditional support. A special thanks to my mom and my dad who are the best parents anyone can have.

Table of Contents

List of Figures

List of Tables

Chapter 1

Introduction

1.1 Background and introduction

1.1.1 The role of rivers

Rivers play a crucial role in delivering terrestrial materials, such as nutrients and sediments, to oceans (e.g., Milliman and Meade, 1983; Walling and Fang, 2003; Meybeck and Vörösmarty, 2005). Consequently, these fluvial-to-marine transition zones are often productive ecosystems which support fisheries and recreational activities, while facing concurrent pressures from both anthropogenic activities (e.g., dam building altering sediment supply, flood control works, Walling, 2006) and climatic changes in precipitation patterns. Numerical modelling of flows within river systems is a key tool used by environmental and resource managers for purposes such as predicting pollutant dispersal, maintenance of navigability, or hazard management (e.g., Knox, 2000; Johnson et al., 2009). As these pressures increase, the ability to accurately and quickly model river flows becomes ever more critical.

Close to the ocean, rivers constitute dynamically complex environments with the influences of freshwater input from upstream and tides from the ocean side driving large temporal and spatial variations in velocities and salinities. Mixing and transport processes occur across a variety of scales – from smaller eddy scales (at which the turbulent kinetic energy is dissipated as heat by viscosity) (Tennekes and Lumley, 1972) to the macroscale (which corresponds to the largest energetic vortices, at which the effect of viscosity is negligible) (e.g., Church, 2007; Franca and Brocchini, 2015). For management purposes, models over river lengths of many kilometers are often required. However, the ability of models to capture the fundamental hydrodynamics of processes which influence flow and water characteristics across this range of scales poses a number of challenges, and numerical models are only as good as our understanding and representation of the underlying processes on which the models rely (e.g., Mosselman, 2012).

Flows within meandering rivers are complex and have been widely studied (e.g., Blanckaert, 2009; Ottevanger et al., 2012; Sukhodolov, 2012; Taye and Kumar, 2022). Within a bend, the centrifugal force balances the gravitational and frictional forces, by increasing the water elevation at the outer bank while decreasing the water elevation at the inner bank; the pressure difference then drives the flow laterally. Water near the surface has strong momentum and moves from the middle of the cross-section of the channel toward the outer bank and then downward. Near the bed, the water has low momentum and flows from the outer bank toward the inner bank and then upward (e.g. Blanckaert and De Vriend, 2004; Sukhodolov, 2012). The presence of secondary flows in addition to the primary flows, which interact with helical cells, flow separation, and effects of the geometry, induces additional complexity to the flow structure (e.g., Abad and Garcia, 2009; Blanckaert, 2009, 2010; Sukhodolov, 2012). Field measurements (e.g., Sukhodolov, 2012) and laboratory studies (e.g., Blanckaert and Graf, 2001) have provided excellent resolution of turbulent features around bends. However, although useful to understand meandering river systems, results from field and laboratory experiments can be difficult to adapt to different areas.

Numerical modelling has been shown to be a powerful tool, which is relatively easily transferable between systems. Modelling free-surface flows and sediment transport in open channels has been widely undertaken using one- (e.g., Vieira and Wu, 2002) or two-dimensional approaches (e.g., Hung et al., 2009), which are particularly useful when dealing with large spatial scales and/or long time scales. However, these approaches cannot resolve more complex structures, including secondary flows. Conversely, three-dimensional models using techniques such as Direct Numerical Simulation or Large Eddy Simulation are able to capture these features, but are very computationally expensive and not always practical, especially for the prediction of flows over larger areas (e.g., Siviglia and Crosato, 2016).

The transport of sediment, as well as momentum, heat and salt in aquatic

environments, is strongly affected by turbulence (e.g., Burchard et al., 2008). Turbulence alters the settling velocity of fine cohesive particles (muds and silts) by enhancing aggregation of particles (flocculation) at low turbulence levels, while promoting break-up of aggregated particles (flocs) at higher levels (e.g., Winterwerp, 1998). These processes thus influence transport, erosion, and deposition of particles, which, eventually, shape the morphology of channels and basins (Dade and Friend, 1998; Church, 2006; Wang et al., 2012). Accurately representing turbulence in numerical models is thus a crucial step to numerically predict settling and deposition of sediments and bed aggradation and degradation (e.g., Papanicolaou et al., 2008).

Over the years, drifters have been used for various purposes, including to understand hydrodynamics (e.g., Charria et al., 2013; Spencer et al., 2014) or to help monitor pollution (e.g., Johnson et al., 2003). In the past, drifters have been commonly used for the investigation of currents (e.g., Davis, 1985; McPhaden et al., 1991; Sabet and Barani, 2011) and wave breaking (e.g., Pascal et al., 2011) in the deep ocean. Additionally, some designs have been shown to be suitable in the study of shallow (water depths 0.2-1 m) coastal environments (e.g., Johnson et al., 2003; Schmidt et al., 2003; Mullarney and Henderson, 2013; Suara et al., 2018) and in rivers (e.g., Postacchini et al., 2015; Tinka et al., 2012). Moreover, for suitable drifter designs, instruments such as Acoustic Doppler Current Profilers (ADCPs) can be mounted and have been used to provide estimates of the dissipation rate of turbulent kinetic energy (e.g., Maurizi et al., 2004; Mullarney and Henderson, 2012; Thomson, 2012). The main advantage of using drifters is that they can capture processes in a flow-following (Lagrangian) frame of reference. For example, Lagrangian datasets can help to investigate the influence of antecedent conditions in flocculation (e.g., MacDonald and Mullarney, 2015). Combining instruments, such as Acoustic Doppler Velocimeters (ADVs) or ADCPs, with drifters also allows for collection of large quantities of data at high spatial resolutions in a limited amount of time when compared with Eulerian deployment of the same

instruments (e.g., Stockdale et al., 2008; Fuentes-Pérez et al., 2022). The main disadvantage is that drifters generate data that change in both space and time, requiring significant effort for data processing (e.g., Mullarney and Henderson, 2012; MacDonald and Mullarney, 2015). Another restriction in the use of drifters is the lack of prototype designs easily available (e.g., Hut et al., 2020).

The present thesis focuses on the modelling of flows and, in particular, characteristics of turbulence and sediment concentrations along a tidally influenced river. A key feature of this work is that we explore flows in a Lagrangian frame-of-reference. This chapter briefly reviews turbulent flows and the modelling thereof, before defining the overarching research questions and describing the approach used in this thesis.

1.1.2 Turbulence

1.1.2.1 Properties of turbulent flows

Open-channel flows are typically characterised by large Reynolds numbers (Re >1,000), hence are turbulent in the majority of cases. Characteristics of turbulent flows include rapid diffusion (diffusivities of momentum heat and salt are several orders of magnitude larger than those due to molecular diffusion alone), dissipation (the conversion of energy into heat by viscous stresses), non-linearity (however, turbulent flows are often simplified by assuming isotropy), randomness or irregularity, and fluctuations in three-dimensional vorticity (particularly, the three dimensionality of turbulence leads to the vortex stretching mechanism) (e.g., Tennekes and Lumley, 1972). Flows can be described by a system of equations, called the Navier-Stokes equations, which outline the conservation of momentum in a viscous fluid, the conservation of mass (continuity equation) and the conservation of energy, along with an equation of state.

The energy cascade is inherent to turbulent systems and refers to the energy transfer from a macro- to a micro-scale (Coufort et al., 2005). This energy

transmission is characterized by three length scales: the Taylor macro-scale Λ, an integral scale for energy-containing eddies, absorbing the kinetic energy from the mean flow, the Taylor micro-scale λ, which characterises the inertial subrange eddies, and the Kolmogorov micro-scale λ_K, which corresponds to the smallest size of turbulent eddies at which the turbulent kinetic energy (TKE) is dissipated into heat by viscosity. The latter length scale can be expressed as (Tennekes and Lumley, 1972):

$$\lambda_K = \left(\frac{\nu^3}{\epsilon}\right)^{\frac{1}{4}}, \tag{1.1}$$

where ν is the kinematic viscosity of the fluid and ϵ is the average rate of dissipation of turbulent kinetic energy.

1.1.2.2 Turbulence modelling

The accuracy of 3D model predictions is strongly dependent on the turbulence models implemented. There is not one uniformly accepted modelling approach to turbulence, but various empirical or statistical approaches are applied, each of them based on different assumptions. A common strategy to model turbulent flow is to use an 'eddy viscosity' (a quantity analogous to molecular quantities of large magnitude) to represent turbulent mixing. The statistical approach is particularly convenient due to the random character of turbulence. However, when solving the equations of motion statistically, there are more unknowns than equations (e.g., Tennekes and Lumley, 1972; Burchard et al., 2008). This problem is called the closure problem of turbulence. In all cases, the non-linearity of the equations means that features of the flow pattern depend on both the initial and boundary conditions of the flow. Some of the most commonly used approaches to model turbulence (e.g., Burchard et al., 2008) include:

- Empirical turbulence modelling: This approach focuses on the conservation of energy in the oceanic mixed layer (e.g., Kraus and Turner, 1967;

Denman, 1973). Empirical models solve the Reynolds-Averaged Navier-Stokes (RANS) equations, which are first simplified using the boundary layer approximation. The turbulent formulae are then expressed based on empirical understanding of the fluxes in geophysical boundary layers (Burchard et al., 2008);

- Direct Numerical Simulation (DNS): Discretization techniques are used to solve the Navier-Stokes equations. The main limitation of this approach is the need to resolve many scales, therefore DNS requires significant numerical resources (e.g., Shih et al., 2000);

- Large Eddy Simulation (LES): This technique is based on the Navier-Stokes equations by, first, spatial-filtering the equations so that the larger-scale turbulent eddies (containing energy) can be calculated while the micro-scale eddies are parameterized (e.g., Ferziger et al., 2002). LES is not often used in coastal and oceanographic environments as this technique requires significant computing capacity. Indeed, high-resolution coastal models can have grid cells size reaching about 0.5 to 1 km while solving large eddy scales would require grid cells of a couple of meters (both horizontally and vertically). The LES approach is therefore limited to small areas (i.e., a few kilometres) (e.g., Scotti, 2010);

- RANS-based turbulence models or statistical turbulence modelling: This approach solves the Reynolds-Averaged Navier-Stokes (RANS) equations with ensemble means. In order to simplify such models, and decrease the computational resource required, the hydrostatic-pressure assumption in the vertical direction is often made (e.g., Deltares, 2020; Lai and Wu, 2019). The hydrostatic assumption can be used in estuaries where the vertical velocity is much smaller than the horizontal speed, and in rivers where the water depth is much smaller than the width of the river. The RANS equations are then often further simplified by applying some local equilibrium assumptions, and closed by means of parameterizations (e.g.,

Burchard et al., 2008). Within Delft3D, there are four closure schemes, which vary in the way they calculate the turbulent kinetic energy and the dissipation rate of turbulent kinetic energy: constant, algebraic, k-L (one transport equation for k) and k-ϵ (two transport equations for k and ϵ).

1.1.2.3 Influence of turbulence on sediment transport

The settling velocity of a particle is the property that controls its vertical movement within the water column, including deposition and resuspension, and consequently the suspended sediment concentration (SSC) within the aquatic environment. Generally larger in size, non-cohesive particles (e.g., sand) tend to stay as individual particles while being transported within the water column. Conversely, cohesive sediments, which correspond to a mixture of finer particles (e.g., clay or silt) and organic matter, experience electrochemical and biochemical attraction between one another leading to aggregation (referred to as flocculation) and breakup (e.g., Winterwerp and van Kesteren, 2004). Studies have shown that turbulence promotes collisions of particles and, consequently, floc formation, until a critical turbulence intensity is reached, after which turbulence tends to increase the breakup of flocs (e.g., Winterwerp, 1998). Flocculation changes the size, composition and density of the particles, therefore affecting their settling velocity (Winterwerp, 1998). Previous work has shown that flocculation was primarily a function of sediment availability but was also dependent on the sources of the particles (i.e., whether they came from river or sea floor) and on the presence of organic matter (Safak et al., 2013). Three main mechanisms have also been shown to promote aggregation (e.g., McCave, 1984; Winterwerp, 1998), namely Brownian motion, differential settling (i.e., a particle with a low settling velocity will sink more slowly than a particle with a larger settling velocity which can lead to collisions), and shear effects. Brownian and differential settling have been shown to be negligible in estuarine and coastal waters (McCave, 1984; Winterwerp, 1998).

1.1.3 Research objectives

The overall aim of this thesis is to explore relationships between turbulence closure schemes, hydrodynamics, turbulence strength, and sediment transport, in a tidally influenced river. In particular, we aim to assess numerical model performance, by comparing with observations in both Lagrangian and Eulerian frames of references. With the present thesis, I will answer the following three sets of research questions.

1. Is there any advantage to using a Lagrangian approach for the validation of a hydrodynamic model? Can a hydrodynamic model reproduce (a) overall trends and (b) small-scale variability in Lagrangian observations of flow speeds and dissipation rates of turbulent kinetic energy when using the commonly applied k-ϵ turbulence closure scheme? Can we distinguish between different controls on the large- and the small-scale hydrodynamics?

2. Is the more sophisticated two-equation k-ϵ turbulence closure scheme better at reproducing Eulerian and Lagrangian speeds and dissipation rates of turbulent kinetic energy than the simpler one-equation k-L turbulence closure scheme?

3. What are the dominant controls on suspended sediment transport in a tidally influenced river? Does the Lagrangian approach allow for examination of the processes involved in the erosion and deposition of sediment in the river? Do flocculation processes strongly influence the distribution of suspended sediment concentration in the water column?

1.1.4 Approach used in this thesis

A model of the tidally influenced, heavily sediment-laden Kaipara River is developed using Delft3D-FLOW, initially using the widely used k-ϵ turbulence closure scheme. The choice of using the Delft3D model was based on widespread usage by practitioners such as environmental consultants or regional councils. Delft3D, in addition to being a freely available open source software,

has been shown to be efficient and stable (Symonds et al., 2016; Li et al., 2021). The model is firstly calibrated following a 'classic' Eulerian approach, comparing model predictions of time series of water levels and speeds to observed data, to achieve a reasonable calibration. Then, dynamics and modelling results are explored in a Lagrangian framework.

An important (but not straightforward) distinction is generally made in sediment transport studies, which often distinguish the bed-load (e.g., Rahuel et al., 1989; Chiari and Rickenmann, 2011) versus the suspended load (Rijn, 1984). The present thesis focuses on the suspended load.

1.1.5 Introduction to Delft3D

The Delft3D-FLOW module is the hydrodynamic module of the Delft3D software suite which solves the two-dimensional (2DH, i.e., depth-averaged) and three-dimensional (3D) unsteady flow and sediment transport equations. Delft3D can be used in areas where the horizontal and time scales are significantly larger than the vertical scales, e.g., in coastal, estuarine, riverine environments as well as lagoons and lakes (Deltares, 2020). Delft3D has been extensively validated for use in shallow waters (e.g., coastal and estuarine environments) (e.g. Roelvink and Van Banning, 1995; Elias et al., 2001). Although Delft3D enables the use of a depth-averaged approach (therefore solving the depth-averaged equations), the present thesis investigates turbulence and sediment transport, which means the vertical variations observed within the fluid are of interest and we therefore focus on three-dimensional modelling.

1.1.5.1 Governing equations

Delft3D is an integrated modelling system, resolved through the finite-difference scheme, which resorts to solving the RANS equations for an incompressible fluid in shallow water using the Boussinesq assumptions (only the pressure term accounts for the effect of variable density) (Deltares, 2020). In order to simplify further the equations describing the flow, Delft3D models also assumes

hydrostatic flow (in the vertical momentum equation, the vertical accelerations are neglected). Hydrostatic models have been previously shown to sometimes be superior to nonhydrostatic models, especially in their reproduction of the vertical distribution of the streamwise velocity (Parsapour-Moghaddam and Rennie, 2017; Ullmann, 2008). Delft3D also assumes the incompressibility of the flow, giving the following equations (Deltares, 2020):

$$\frac{\partial \zeta}{\partial t}+\frac{1}{\sqrt{G_{\xi\xi}}\sqrt{G_{\eta\eta}}}\frac{\partial\left((d+\zeta)U\sqrt{G_{\eta\eta}}\right)}{\partial \xi}+\frac{1}{\sqrt{G_{\xi\xi}}\sqrt{G_{\eta\eta}}}\frac{\partial\left((d+\zeta)V\sqrt{G_{\xi\xi}}\right)}{\partial \eta}=(d+\zeta)Q, \tag{1.2}$$

which is the continuity equation in sigma coordinates, where ζ is the water level above the horizontal plane of reference, $\sqrt{G_{\xi\xi}}$ and $\sqrt{G_{\eta\eta}}$ are coefficients used to transform curvilinear to rectangular co-ordinates, d is the depth below the horizontal plane of reference, ξ are the horizontal co-ordinates and η are the curvilinear co-ordinates. U and V are the depth-averaged velocities:

$$U=\frac{1}{d+\zeta}\int_{d}^{\zeta} u\,dz=\int_{-1}^{0} u\,d\sigma, \tag{1.3}$$

and

$$V=\frac{1}{d+\zeta}\int_{d}^{\zeta} v\,dz=\int_{-1}^{0} v\,d\sigma, \tag{1.4}$$

where u is the flow velocity in the x- or ξ-direction and v is the flow velocity in the y- or η-direction, σ is the scaled vertical co-ordinate:

$$\sigma=\frac{z-\zeta}{d+\zeta}, \tag{1.5}$$

and Q represents the contributions per unit area (owing to the discharge or withdrawal of water, evaporation and precipitation):

$$Q=\int_{-1}^{0}(q_{in}-q_{out})d\sigma+P-E, \tag{1.6}$$

where q_{in} and q_{out} are the local sources and sinks of water per unit of volume [1/s], respectively, and P and E are the non-local source terms of precipitation and evaporation, respectively.

The momentum equations in the horizontal directions are:

$$\frac{\partial u}{\partial t}+\frac{u}{\sqrt{G_{\xi\xi}}}\frac{\partial u}{\partial \xi}+\frac{v}{\sqrt{G_{\eta\eta}}}\frac{\partial u}{\partial \eta}+\frac{\omega}{d+\zeta}\frac{\partial u}{\partial \sigma}-\frac{v^2}{\sqrt{G_{\xi\xi}}\sqrt{G_{\eta\eta}}}\frac{\partial \sqrt{G_{\eta\eta}}}{\partial \xi}+\frac{uv}{\sqrt{G_{\xi\xi}}\sqrt{G_{\eta\eta}}}\frac{\partial \sqrt{G_{\xi\xi}}}{\partial \eta}-fv = -\frac{1}{\rho_0\sqrt{G_{\xi\xi}}}P_\xi+F_\xi+\frac{1}{(d+\zeta)^2}\frac{\partial}{\partial\sigma}\left(\nu_V\frac{\partial u}{\partial\sigma}\right)+M_\xi, \tag{1.7}$$

and

$$\frac{\partial v}{\partial t}+\frac{u}{\sqrt{G_{\xi\xi}}}\frac{\partial v}{\partial \xi}+\frac{v}{\sqrt{G_{\eta\eta}}}\frac{\partial v}{\partial \eta}+\frac{\omega}{d+\zeta}\frac{\partial v}{\partial \sigma}+\frac{uv}{\sqrt{G_{\xi\xi}}\sqrt{G_{\eta\eta}}}\frac{\partial \sqrt{G_{\eta\eta}}}{\partial \xi}-\frac{u^2}{\sqrt{G_{\xi\xi}}\sqrt{G_{\eta\eta}}}\frac{\partial \sqrt{G_{\xi\xi}}}{\partial \eta}+fu = -\frac{1}{\rho_0\sqrt{G_{\eta\eta}}}P_\eta+F_\eta+\frac{1}{(d+\zeta)^2}\frac{\partial}{\partial\sigma}\left(\nu_V\frac{\partial v}{\partial\sigma}\right)+M_\eta, \tag{1.8}$$

where ω is the vertical velocity, f is the Coriolis parameter, ρ_0 is the density of water, P_ξ and P_η are pressure gradients. F_ξ and F_η represent the unbalance of horizontal Reynold's stresses, ν_V is the vertical eddy viscosity, M_ξ and M_η represent the contributions due to external sources or sinks of momentum.

In Delft3D-FLOW, the three-dimensional suspended sediment transport resolves the three-dimensional mass balance (advection-diffusion) equation for the suspended sediment (Deltares, 2020):

$$\frac{\partial c^{(l)}}{\partial t}+\frac{\partial uc^{(l)}}{\partial x}+\frac{\partial vc^{(l)}}{\partial y}+\frac{\partial (w-w_s^{(l)})c^{(l)}}{\partial z}-\frac{\partial}{\partial x}(\epsilon_{s,x}^{(l)}\frac{\partial c^{(l)}}{\partial x})-\frac{\partial}{\partial y}(\epsilon_{s,y}^{(l)}\frac{\partial c^{(l)}}{\partial y})-\frac{\partial}{\partial z}(\epsilon_{s,z}^{(l)}\frac{\partial c^{(l)}}{\partial z})=S^{(l)}, \tag{1.9}$$

where $c^{(l)}$ is the mass concentration of the sediment fraction (l), $\epsilon_{s,x}^{(l)}$, $\epsilon_{s,y}^{(l)}$ and $\epsilon_{s,z}^{(l)}$ are the eddy diffusivities of the sediment fraction (l), w is the flow velocity in the z-direction, w_s is the sediment settling velocity of the sediment fraction (l) and $S^{(l)}$ is the source and sink term representing the exchange with the bed

(i.e., deposition and entrainment).

The suspended sediment transport is calculated following a similar approach to all of the other conservative constituents (e.g., salinity or heat) but it also comprises other inherent processes. Indeed, the computation of sediment transport also includes the action of gravity which is taken into account through the definition of a settling velocity for the sediments, the exchange of particles between the water column and the bed (which also influences the bed morphology and therefore the hydrodynamic computations) and the impact of sediments on the density and therefore on turbulence damping (Deltares, 2020).

1.1.5.2 Turbulence in Delft3D

In most instances, the turbulent scales of motion cannot be solved directly due to the coarseness of the grid and the time step, and the turbulent processes are therefore 'sub-grid'. The turbulent quantities are space- and time-averaged. Appropriate assumptions are required in order to close the RANS equations. In Delft3D-FLOW, four turbulent closure schemes can be used: constant, algebraic, k-L and k-ϵ. The present thesis focuses on the two closure schemes involving transport equations, the k-L turbulence closure model and the k-ϵ turbulence closure model. The k-L model is a first order turbulence closure scheme and includes a transport equation (1.10) for the turbulent kinetic energy k while the mixing length L is computed analytically (Deltares, 2020):

$$\frac{\partial k}{\partial t}+\frac{u}{\sqrt{G_{\xi\xi}}}\frac{\partial k}{\partial \xi}+\frac{v}{\sqrt{G_{\eta\eta}}}\frac{\partial k}{\partial \eta}+\frac{w}{d+\zeta}\frac{\partial k}{\partial \sigma}=\frac{1}{(d+\zeta)^2}\frac{\partial}{\partial \sigma}(D_k\frac{\partial k}{\partial \sigma})+P_k+P_{kw}+B_k-\epsilon, \tag{1.10}$$

where the dissipation term D_k is:

$$D_k=\frac{\nu_{mol}}{\sigma_{mol}}+\frac{\nu_{3D}}{\sigma_k}, \tag{1.11}$$

the production term P_k is:

$$P_k = \nu_{3D} \frac{1}{(d+\zeta)^2} [(\frac{\partial u}{\partial \sigma})^2 + (\frac{\partial v}{\partial \sigma})^2], \tag{1.12}$$

P_{kw} is the turbulent energy production due to the action of wave, which is neglected in the present thesis, and the buoyancy flux B_k is defined as:

$$B_k = \frac{\nu_{3D}}{\rho \sigma_\rho} \frac{g}{H} \frac{\partial \rho}{\partial \sigma}, \tag{1.13}$$

where ν_{3D} is the part of eddy viscosity due to turbulence model in the vertical direction, ρ is the density of water, σ_ρ is the Prandlt-Schmidt number for density (σ_ρ=0.7), and H is the total water depth (positive downward).

The dissipation of turbulent kinetic energy, ϵ, is then defined as:

$$\epsilon = c_D \frac{k\sqrt{k}}{L}, \tag{1.14}$$

where

$$c_D \simeq 0.1925, \tag{1.15}$$

and L is the mixing length, which is the maximum distance over which a parcel of fluid will preserve its original features before mixing into the surrounding fluid and is defined as:

$$L = \kappa(z+d)\sqrt{1 - \frac{z+d}{H}} F_L(Ri), \tag{1.16}$$

in which κ is the Von Kármán constant ($\kappa \approx 0.41$), z is the Cartesian coordinate in the z-direction and F_L(Ri) is a damping function which depends on the Richardson number Ri as

$$F_L(\mathrm{Ri}) = \begin{cases} e^{-2.3Ri}, & \mathrm{Ri} \geq 0, \\ (1-14Ri)^{0.25}, & \mathrm{Ri} < 0. \end{cases} \tag{1.17}$$

The k-ϵ model is a second order turbulence closure model, meaning that

both the TKE and ϵ are computed using a transport equation (Deltares, 2020). The TKE is computed with Equation 1.10 and ϵ using:

$$\frac{\partial \epsilon}{\partial t}+\frac{u}{\sqrt{G_{\xi\xi}}}\frac{\partial \epsilon}{\partial \xi}+\frac{v}{\sqrt{G_{\eta\eta}}}\frac{\partial \epsilon}{\partial \eta}+\frac{w}{d+\zeta}\frac{\partial \epsilon}{\partial \sigma}=\frac{1}{(d+\zeta)^2}\frac{\partial}{\partial \sigma}(D_\epsilon\frac{\partial \epsilon}{\partial \sigma})+P_\epsilon+P_{\epsilon w}+B_\epsilon-c_{2\epsilon}\frac{\epsilon^2}{k} \tag{1.18}$$

with

$$D_\epsilon=\frac{\nu_{3D}}{\sigma_\epsilon}, \tag{1.19}$$

the production term P_ϵ is:

$$P_\epsilon=c_{1\epsilon}\frac{\epsilon}{k}P_k, \tag{1.20}$$

$\mathrm{P}_{\epsilon w}$ is the dissipation term due to wave (neglected here), and the buoyancy flux B_ϵ is defined as:

$$B_\epsilon=c_{1\epsilon}\frac{\epsilon}{k}(1-c_{3\epsilon})B_k, \tag{1.21}$$

where $c_{1\epsilon}$, $c_{2\epsilon}$ and $c_{3\epsilon}$ are calibration constants:

$$c_{1\epsilon}=1.44 \tag{1.22}$$

$$c_{2\epsilon}=1.92 \tag{1.23}$$

and

$$c_{3\epsilon}=\begin{cases} 0 \text{ unstable stratification} \\ 1 \text{ stable stratification} \end{cases}. \tag{1.24}$$

The mixing length is then calculated using:

$$L=c_D\frac{k\sqrt{k}}{\epsilon}. \tag{1.25}$$

1.1.6 Field site and data collection

1.1.6.1 Study site

The present thesis is based on a data set collected in the Kaipara River, a 94,700-hectare drowned-valley system, which is located at the southern end of the Kaipara Harbor, in the North Island of New Zealand (175.45°E, 36.67°S) (MacDonald and Mullarney, 2015). The estuary has a local ecological significance due to the presence of some rare and unique species (e.g., subtidal *Zostera* and tube building worms *Owenia*, *Macrolymenella*, respectively) (Heath, 1975; Haggitt et al., 2008). The work in this thesis is focused on a section from about 15 km upstream of the Kaipara River to the entrance of the estuary, therefore comprising the zone of transition between freshwater and salty water. The tidal range observed at the downstream edge of the study domain is approximately 3 m (which means the Kaipara river is mesotidal). Inside the study area, the river ranges between 50 and 200 m wide with mean and maximum depths along the thalweg of 4.5 m and 9.2 m, respectively. The river is largely meandering, with bends of different curvature. During the time of the experiment, the SSC increased from 50 mg.L^{-1} upstream to approximately 850 mg.L^{-1}, with a mean concentration of about 300 mg.L^{-1} (MacDonald and Mullarney, 2015).

1.1.6.2 Data collection and processing

The dataset used in this work was generated using a novel design of a subsurface drifter deployed in the Kaipara River (Figure 1.1). Three deployments were undertaken during 1-3 October 2013, during the ebb stage of the tidal cycle. During each deployment, up to three 'Floc Drifters' were released in a Lagrangian mode (Figure 1.1c) from three different locations in the river and were advected downstream for approximately 4 hr. The drifters were sitting about 1.5 m under the water surface and were each equipped with a GPS, a floc camera ('FlocCam'), a downward-looking pulse-coherent Acoustic Doppler Current

Profiler (ADCP, 2-MHz Nortek Aquadopp), which measures 3D velocity short (0.73 m-long) profiles at 8 Hz, with vertical bin sizes of 25 mm (during post-processing, bins with correlation of less than 50 % were removed), an Acoustic Doppler Velocimeter (ADV, Nortek Vector), which collected single-point measurements of the 3D velocity components at a sampling rate of 16 Hz, and a Sea-Bird Electronics SBE-37 MicroCAT Conductivity-Temperature-Depth (CTD) probe sampling at a rate of 0.167 Hz. An Optical Backscatter Sensor (OBS) was also attached to the ADV and sampled at 5 Hz. In order to acquire the water velocities, horizontal motions of the drifter were computed (by differencing GPS positions) and subtracted from the ADCP measurements. Owing to the use of pulse-coherent instruments, there were uncertainties in velocities, which were corrected using an unwrapping routine (e.g., Lhermitte and Serafin, 1984; Lohrmann et al., 1990; Zedel et al., 1996). The dissipation rates of turbulent kinetic energy, ϵ (in $W.kg^{-1}$ or $m^2.s^{-3}$), time series were calculated using the structure function method of Wiles et al. (2006) on the velocity profiles from the ADCP over windows of 64 s (e.g., Mullarney and Henderson, 2013). Velocities collected by the ADV corresponding to beams with correlations less than 90 % or signal-to-noise ratio below 20 were removed (which corresponded to less than 2.5 % of the data). More details regarding the Floc Drifter platform, instrumentation and post-processing can be found in MacDonald and Mullarney (2015). During the time of the experiment, in addition to the three Lagrangian drifter platforms, three near-bed ADCPs (RDI 1,200 kHz Workhorse) and Sea-Bird Electronics SBE-37 MicroCAT Conductivity-Temperature-Depth sensors were positioned at fixed locations (upstream, center and downstream of the river domain; Figure 1.1d). The ADCPs collected profiles of velocities at 1 Hz with 0.25 m vertical resolution. The frequency of the fixed CTD sensors was 0.1667 Hz. Data from the fixed locations were averaged over 10 minutes to be used for model calibration.

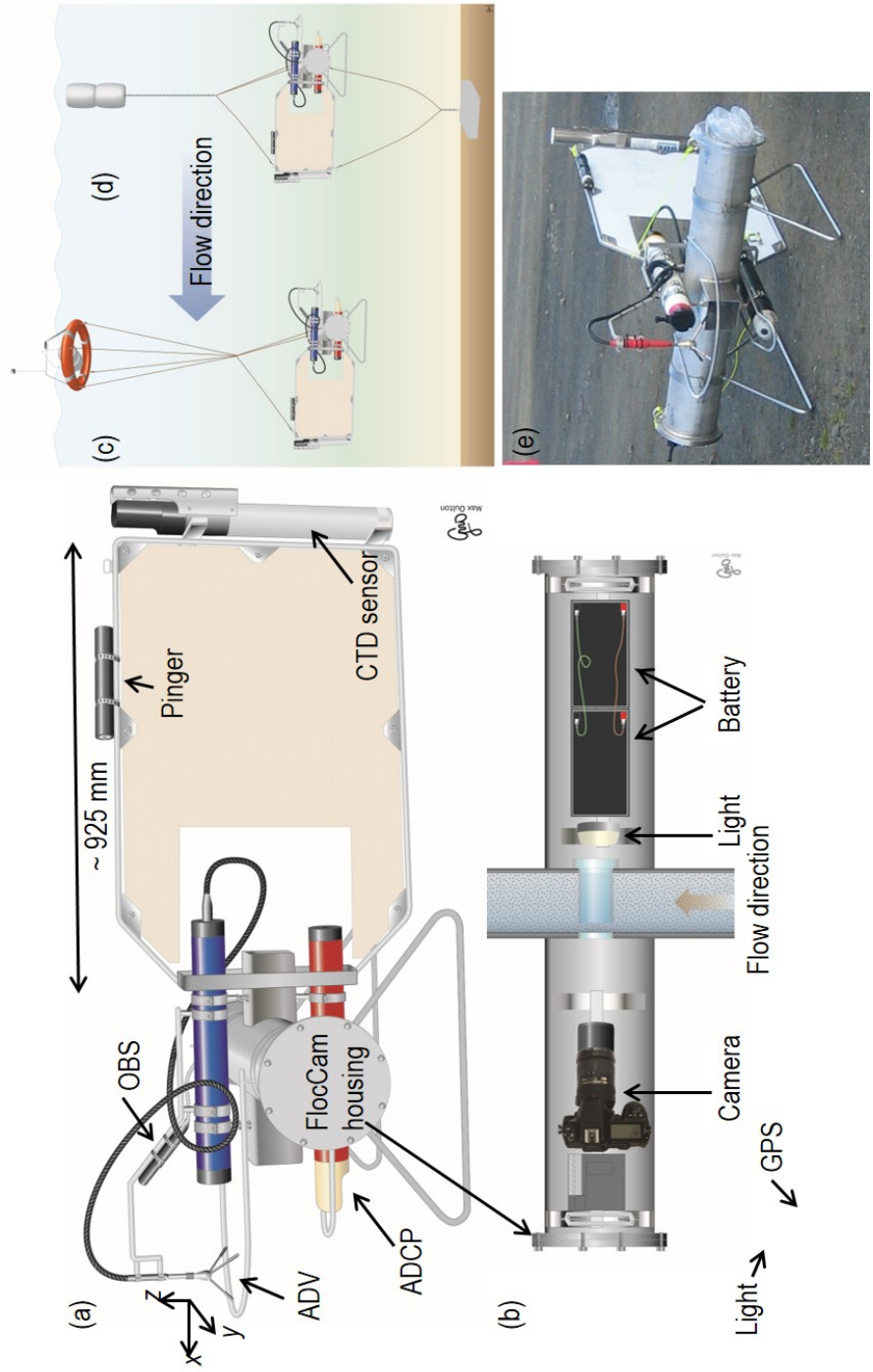

Figure 1.1: Schematic of (a) the FlocDrifter body (approximately to scale), (b) the FlocCam system in underwater housing, and the complete FlocDrifter platform in (c) Lagrangian and (d) Eulerian deployment modes; and (e) photograph of drifter (before right-hand end cap of camera housing was attached) (after MacDonald and Mullarney, 2015).

1.1.7 Thesis outline

The following three chapters are written as standalone documents with each chapter forming a submission to an international peer-reviewed journal.

- In a second chapter, a model of the tidally driven heavily sediment-laden meandering Kaipara River is developed and calibrated using a 'classic' Eulerian approach, by comparing water levels and speeds predicted by the model with observations. The model is run with the two-equation k-ϵ turbulence closure scheme. Results of the model are then compared with high-resolution Lagrangian observations of speed and ϵ collected by the drifting platforms described in Section 1.1.6.2 in order to assess the performance of the model and identify deficiencies. This work was published in *Water Resources Research* in 2022.

- In a third chapter, numerical results of the model, run with both the two-equation k-ϵ and the simpler one-equation k-L turbulence closure models, are presented and compared with the Lagrangian dataset of speed and ϵ in order to assess which model performs better. This work will be submitted to a peer-reviewed journal.

- In a fourth chapter, sediment transport is added to our Kaipara model, which is run with both k-ϵ and k-L closure schemes. The goal is to investigate the controls on sediment transport in the river. As in the previous chapters, the model results are studied in a Lagrangian frame of reference. This work will be submitted to a peer-reviewed journal.

- In Chapter 5, the main findings of this work are summarised and we make suggestions for future work.

Chapter 2

Lagrangian observations and modelling of turbulence along a tidally influenced river

Contribution of authors

Chapter 2 duplicates a paper of the title "Lagrangian observations and modelling of turbulence along a tidally influenced river" by Bérengère S. Dejeans, Julia C. Mullarney and Iain T. MacDonald, which was published in the peer-reviewed journal *Water Resources Research* in 2022. The majority of text and figures are identical to the published version with the exception of a few small changes as suggested by the examiners of this thesis. I developed the numerical model with Delft3D, with the input of Glen Reeve and Mark Pritchard. Iain MacDonald and Julia Mullarney provided me with the field observations. I wrote MATLAB scripts to process the data and make all the figures for this manuscript. My co-authors, Julia Mullarney and Iain MacDonald helped me with the analyses of the data, the interpretation of the results and provided me with feedback, direction and editorial help. The paper was reviewed by Professor Jeff Nittrouer and two anonymous reviewers.

Abstract

We examine and model the patterns of velocities and turbulence from flow-following measurements along a tidally influenced river, collected from the heavily sediment-laden Kaipara River, New Zealand, using Lagrangian 'Floc Drifter' platforms released at different locations and times. Numerical modelling was undertaken in Delft3D with the k-ϵ turbulence closure scheme. While model calibration using Eulerian measurements was classified as excellent, results explored in a Lagrangian framework revealed deficiencies in model performance. Generally, the model reproduced flow speeds and patterns of dissipation rates of turbulent kinetic energy ϵ of the right order of magnitude, but did not always correctly reproduce the observed ϵ, particularly around abrupt meander bends. These discrepancies were attributed partly to errors in velocity predictions, but also indicated that other processes (omitted or not accurately represented in our model) such as wind-driven mixing and secondary flow strongly influenced turbulence dynamics. Predicted ϵ were relatively consistent across different tidal phases and days, suggesting the bathymetry and geometry of the river were the greatest control on the along-river structure of turbulence. The vertical and cross-sectional distributions of turbulent quantities (ϵ, k and ν) displayed larger variations vertically than longitudinally and agree with previous studies. Results show that flow-following measurements offer a stringent validation for numerical modelling of hydrodynamics over large (riverine) spatial scales at a temporal and spatial resolution not possible with traditional Eulerian measurements. Ultimately, robust numerical predictions of velocities and turbulence are critical to accurately model and predict the dispersal and fate of fine-sediments in aquatic

environments.

2.1 Introduction

Turbulence has a pronounced effect on many aspects (erosion, deposition, vertical mixing, flocculation) of sediment transport in estuaries and coastal waters, and many coastal management projects rely on the ability to accurately predict the dispersal and settling of such particles, which are mainly governed by the settling velocity. For cohesive sediments, flocculation (i.e. the aggregation of particles) adds substantial complexity to modelling by altering the size, composition and hence settling velocity of particles over time. Flocculation has been shown to be largely affected by turbulent shear, among other factors (e.g., Winterwerp, 1998; Manning and Dyer, 1999; Kumar et al., 2010). Therefore, robust numerical model predictions of the structure of turbulence within the water column are required as a first step for modelling of flocculation and cohesive sediment transport.

Turbulence can be described over multiple lengthscales in riverine environments: horizontally (width of the river channel), vertically (depth of the channel) and over the Kolmogorov microscale λ_K, i.e. the smallest turbulent eddies (Yokosi, 1967). Studies on flows within riverine environments have shown the importance of meander bends, and particularly the effects of their curvature and amplitude (e.g., Whiting and Dietrich, 1993a,b; Abad and Garcia, 2009; Blanckaert and Graf, 2001; Sukhodolov, 2012) and of riverbed bathymetry (e.g., Sukhodolov, 2012). When modelling sediment transport, calculations require the inclusion of sub-grid scale turbulent processes. A commonly used approach is based on the Reynolds-Averaged Navier-Stokes (RANS) equations, which are solved using means of parameterization to close the system. Simplifying the equations often includes the assumption of local equilibrium, i.e. assuming that turbulence is in equilibrium with local environmental conditions (which results in a linear system of equations), and the application of

the boundary layer assumption, which disregards all of the horizontal mixing terms (e.g., Tennekes and Lumley, 1972; Burchard et al., 2008).

The work presented in this paper focuses on the flow-following prediction of the distribution of turbulence within a river by a three-dimensional numerical model solving the Reynolds-averaged Navier-Stokes equations. The k-ϵ turbulence closure scheme is used, in which the turbulent kinetic energy k and the dissipation rate of turbulent kinetic energy, ϵ, are defined based on the transport equations and the value of the mixing length L is subsequently derived (Deltares, 2020). The aim of the present work is to explore the performance of a 'standard' model in a Lagrangian frame of reference. More precisely, we used the Delft3D suite, which is widely used for coastal and estuarine engineering purposes, to develop a model, which was calibrated following a standard Eulerian approach and we conducted a detailed comparison of model results with a high-resolution Lagrangian dataset.

The use of drifters has been proven to serve various purposes, including, for instance, pollution monitoring (e.g., Johnson et al., 2003) or description of hydrodynamics (e.g., Charria et al., 2013; Spencer et al., 2014). Drifters have been used in the past in order to study currents (e.g., Davis, 1985; McPhaden et al., 1991; Sabet and Barani, 2011) and the breaking of waves (e.g., Pascal et al., 2011) in the deep ocean but have also proved to be suitable to investigate shallower environments (e.g., Johnson et al., 2003; Schmidt et al., 2003; Mullarney and Henderson, 2013; Suara et al., 2018) including rivers (e.g., Tinka et al., 2012; Postacchini et al., 2015). Other work has also used drifters in order to derive Lagrangian measurements of turbulence (e.g., Maurizi et al., 2004; Thomson, 2012; Mullarney and Henderson, 2012).

The dependence of turbulence within rivers on river curvature and bathymetry has previously been explored through laboratory experiments, field studies and numerical modelling. Laboratory experiments have demonstrated that the spatial variability of the flow was strongly influenced by the curvature and the bathymetry of channels (Blanckaert, 2010, 2011). These dependen-

cies have been supported by field measurements; e.g. Sukhodolov (2012) who explored the cross-channel variability of velocity, TKE and turbulent shear stress within a relatively large river reach (about 30 m wide). While the cross-channel morphology (riffle-pool) was found to be a dominant control on the turbulence, they noted a need for additional data to determine the appropriate length scales for upscaling of results). Similarly, frequency field measurements in a meander collected by Engel and Rhoads (2017) revealed the vertical structure of velocity and turbulence is strongly driven by the topography of the seabed and of the geometry of the bend. Turbulence in meandering rivers has also been studied via 3D RANS-based hydrodynamic models. Surface slope and secondary flows are often well predicted using a k-ϵ turbulence closure scheme (e.g., Demuren and Rodi, 1986; Wormleaton and Ewunetu, 2006; Parsapour-Moghaddam and Rennie, 2017) even for strongly curved bends (Gholami et al., 2014). These studies have also shown that different turbulence models predicted slightly different simulated flow; for instance, de Almeida and Ota (2020) demonstrated that the k-ϵ closure scheme could reliably reproduce the velocity all along the domain in their 2D-simulation of a curved channel whereas the other model they tested, the Elder Model (an algebraic model), could not reproduce the velocity field both in sections of high curvature and in straight portions of the channel. Similarly, other studies have found that 3D velocity structure (and hence predictions of solute transport) are sensitive to the selected turbulence closure scheme, mainly due to the difficulty in perfectly reproducing the flow separation (Kim et al., 2020). While previous studies have focused on the across-river structure of turbulence around a single bend and reveal complex and often contradictory results (Engel and Rhoads, 2017), the along-river distributions of turbulence are relatively less explored - particularly for longer sections covering tens of kilometers. Here, we use high-resolution Lagrangian field observations to validate a numerical model and to explore the flow-following distributions of turbulence along a river. Turbulence in meandering rivers has also been studied via modelling approaches, including

models based on the RANS equations (e.g., Rameshwaran and Naden, 2004; Wormleaton and Ewunetu, 2006; Fischer-Antze et al., 2009; Gholami et al., 2014; de Almeida and Ota, 2020; Kim et al., 2020), which rely on the performance of the turbulence models. More recently, the impact of turbulence closure schemes on the flow in curved channels has been investigated (e.g., de Almeida and Ota, 2020; Kim et al., 2020). However, few studies have used high-resolution Lagrangian field observations to validate a numerical model and to explore the flow-following distributions of turbulence along a river.

In the present work, the assessment of the model performance is done by comparing output of a key turbulence parameter, ϵ, with unique, high-spatial-resolution observations collected in a Lagrangian frame of reference along a tidally influenced river. The flow-following approach thus allows the resolution of the distribution of turbulence over different spatial scales, from the whole river domain to meander bends and to smaller features, such as pools, which have been shown to affect flow structures (e.g., Abad and Garcia, 2009; Sukhodolov, 2012), but which would not necessarily be captured by a set of Eulerian observations. The use of a Lagrangian dataset means measurements account for upstream conditions, which have been shown to play an important role in transport of fine sediments (Dyer, 1989). Braithwaite et al. (2012) have observed that the flocculation model proposed by Winterwerp (1998) required the inclusion of a phase lag giving particles the time to adjust to changes in turbulence, hence there is a need for accurate modelling of Lagrangian observations to improve sediment transport calculations. A preliminary model set up and findings are introduced in Dejeans et al. (2017). The model presented here uses a much higher grid resolution and the current manuscript provides a more detailed and extensive description of the performance of the model in a Lagrangian frame of reference. Model results are also compared in detail with findings from past studies. The discussion also examines the benefits and complications of the use of Lagrangian measurements.

The structure of the manuscript is as follows: Section 2.2 describes the

study site and the experimental observations from a tidal river. In Section 2.3, we give the details of the model set up and its calibration. While in Section 2.4, model predictions of velocity and dissipation of turbulent kinetic energy are presented and compared with observations. Discussion and conclusions are presented in Sections 2.5 and 2.6, respectively.

2.2 Study area and data collection

2.2.1 Study site

The dataset used in this study was collected in the Kaipara River, which is a large (94700 ha) drowned-valley system located at the southern end of the Kaipara Harbour, in the North Island of New Zealand (174.45° E, 36.67° S, Figure 2.1) (MacDonald and Mullarney, 2015). The estuary is of significant local ecological importance due to the presence of some rare (e.g., subtidal *Zostera*) and even unique (e.g. tube building worms *Owenia*, *Macroclymenella*) species among the marine communities (Haggitt et al., 2008; Heath, 1975). This study focuses on the section of the Kaipara river from approximately 15-km upstream to the entrance to the estuary, and thus includes the transition zone between freshwater to salty water. Although the shoreline classification by Davies (1964) defines the Kaipara harbour as macrotidal, the tidal range at the downstream end of the study area (corresponding to the river mouth) is about 2 m. Within the experiment domain, the river width varies between about 50 and 200 m; the average depth along the thalweg and the deepest point are 4.5 m and 9.2 m below MSL, respectively. The river is characterized by large meandering bends in multiple directions. Calibrated optical backscatter measurements on the drifters showed that suspended sediment concentration (SSC) generally tended to augment from around 50 $\mathrm{mg.L^{-1}}$ upstream to downstream, with an average of about 300 $\mathrm{mg.L^{-1}}$ and most of the values did not exceed 400 $\mathrm{mg.L^{-1}}$ during the time of the experiment (MacDonald and Mullarney, 2015).

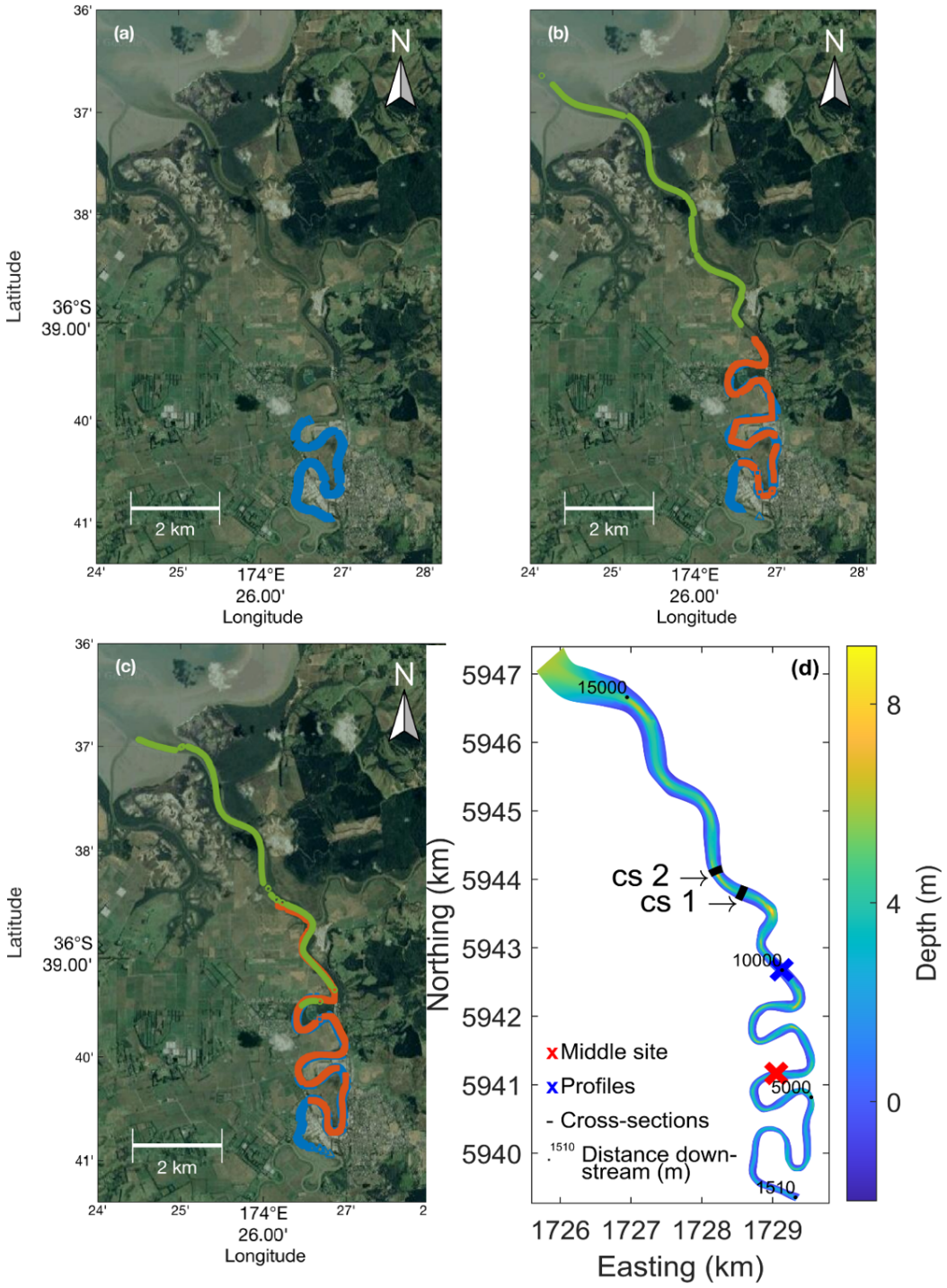

Figure 2.1: Tracks of the different drifters (blue, orange and green) deployed on October (a) 1st, (b) 2nd (c) 3rd 2013 on Google Earth and (d) bathymetry and location of the middle site (red cross), cross-sections (black lines) and profiles (blue cross). Locations provided for the central drifter on day 2 (orange, b) are only estimates (within $\lesssim 10$ m of chase-boat locations) owing to a defective GPS after 112 minutes on that day.

2.2.2 Data collection and processing

Data was collected within the Kaipara River over three deployments during 1-3 October 2013. Each deployment lasted for the ebb stage of the tidal cycle and consisted of deploying up to three 'Floc Drifters' in the Kaipara River (Figure 2.2). The drifters were released in a Lagrangian mode, from three different locations in the river, at the beginning of an ebb tide and travelled downstream for ~ 4 hr (Table 3.1). Each GPS-tracked drifter platform sits approximately 2 m under the water surface and is composed of a floc camera ('FlocCam'), a pulse-coherent 2-MHz Nortek Aquadopp Acoustic Doppler Current Profiler (ADCP), collecting short profiles of 3D velocity components, a Nortek Vector Acoustic Doppler Velocimeter (ADV), to measure 3D velocity components at single points (at a sampling rate of 16 Hz), a Sea-Bird Electronics SBE-37 MicroCAT Conductivity-Temperature-Depth (CTD) probe with a sampling rate of 0.167 Hz and an Optical Backscatter Sensor (OBS). The present paper focuses on the hydrodynamics and so the sediment data (from the FlocCam and OBS) are not presented herein. The downward-looking ADCP recorded velocities over a 0.73-m long profiles at 8 Hz with vertical bin sizes of 25 mm. Data was sampled near continuously over bursts of 512 s, with a 3-s gap between bursts. Post-processing of the data included removing bins with correlations less than 50 percent. Moreover, horizontal motion of the drifter was obtained by differencing GPS positions and removed from the ADCP measurements to obtain horizontal water velocities. Uncertainties in velocity due to the use of pulse coherent instruments were corrected (e.g., Lhermitte and Serafin, 1984; Lohrmann et al., 1990; Zedel et al., 1996)). Times at which the phase shift between pulses could not be determined were discarded. Time series of the dissipation rates of turbulent kinetic energy, ϵ (in W.kg^{-1} or m^2.s^{-3}), were estimated using the structure function method of Wiles et al. (2006) on the velocity profiles collected with the ADCP over windows of 64 s (e.g., Mullarney and Henderson, 2013). Velocities recorded by the ADV corresponding

to beams with low correlations (i.e. $< 90\,\%$) or low signal-to-noise ratio (i.e. $< 20\,\%$) were removed, which accounted for less than $2.5\,\%$ of the data. Salinity was derived from the CTD data (Hill et al., 1986). Further details of the Floc Drifter platform, instrumentation and post-processing techniques can be found in MacDonald and Mullarney (2015). In addition to the three Lagrangian Floc Drifter platforms, three near-bed ADCPs (RDI 1200 kHz Workhorse) and Sea-Bird Electronics SBE-37 MicroCAT Conductivity-Temperature-Depth sensors were deployed at fixed locations in the upstream, centre and downstream sections of the experimental domain (Figure 2.1). The ADCPs recorded a profile of velocities at 1 Hz with 0.25 m vertical resolution. The fixed CTD sensors sampled at 0.1667 Hz. Data collected in the river were averaged to provide 10-min temporal resolution to calibrate the model.

Table 2.1: FlocDrifters released and retrieval times.

Release date	Drifter	Release time	Recovery time	Length of section covered
01/10/2013	Drifter 01	10:08:53	14:24:30	5.2 km
02/10/2013	Drifter 01	10:24:13	14:44:30	7.2 km
02/10/2013	Drifter 02	10:32:09	14:41:42	7.1 km
02/10/2013	Drifter 03	11:22:13	14:54:33	6.6 km
03/10/2013	Drifter 01	10:42:51	15:03:35	7.4 km
03/10/2013	Drifter 02	10:52:28	15:31:16	9.0 km
03/10/2013	Drifter 03	11:48:33	15:27:41	7.9 km

2.3 Numerical model description

2.3.1 Model set up

A hydrodynamic model of the Kaipara River was set up using the Delft3D-FLOW software package (Deltares, 2020). Delft3D solves the Reynolds-Averaged Navier-Stokes (RANS) equations for an incompressible fluid using the shallow water and Boussinesq assumptions and has been extensively validated (e.g., Elias et al., 2001).

The model domain covers about 15 kilometers in length of the Kaipara river, from the location of the upstream ADCP to the mouth of the river,

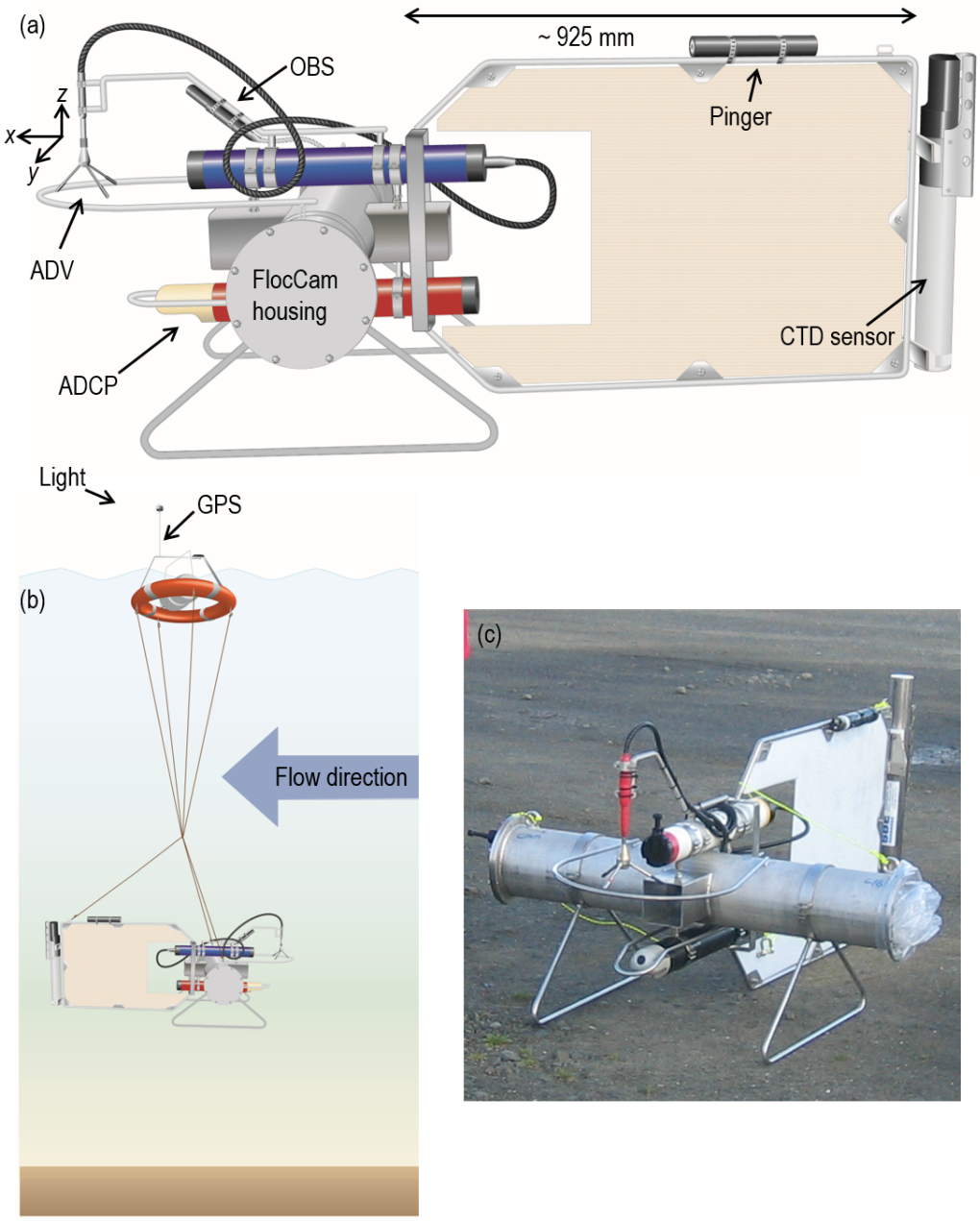

Figure 2.2: Schematic of (a) a FlocDrifter platform, deployed in (b) Lagrangian mode ; and (c) photograph of the drifter (after MacDonald and Mullarney, 2015).

artificially extended by about 500 m into the estuary basin (Figure 2.1d). The grid consisted of 6770-along river and 50-across river rectangular grid cells of size approximately 2.4×2.1 m. In the vertical direction, a σ-model is used, so the number of layers remains constant throughout the whole domain, and, consequently, the thickness of each layer varies with the position and time Deltares (2020). In the present model, 20 equal-sized σ-layers (5% of water

depth) were used. The model latitude was specified as 37° S. Bathymetry (Figure 2.1c) was interpolated from a combination of LIDAR data provided by the Auckland Regional Council and two single-beam echosounder surveys conducted in 2013 and 2017. Two open boundaries were defined. The downstream edge of the grid was forced with a time series of water levels from observations collected by the Pouto Point tide gauge located near the mouth of the Kaipara harbour (with a phase offset to account for tidal propagation). The upstream boundary was forced by the current speeds collected by the fixed ADCP deployed during the fieldwork campaign (see Section 2.2.2). The winds were observed to be very light during the deployment of the instruments on the three days and no wind forcing was applied. Model simulations were run for a total of six days. The three-day time series boundary conditions were repeated twice (starting at mid tide), to allow for a three-day 'spin-up' time, followed by the three days corresponding to the observations (i.e. 1 Oct to 3 Oct, 2013). At the two boundaries, both salinity and temperatures were set as time-varying but vertically uniform using the observations collected during the field experiment (see Section 2.2.2). The background horizontal viscosity and diffusivity were both set to $1\,\mathrm{m}^2.\mathrm{s}^{-1}$ and the background vertical viscosity and diffusivity were set to zero (i.e. the model default values). The model used the $k-\epsilon$ turbulence closure scheme. The time step of the numerical simulation was set to 0.2 min and the model results were output every time step during the time of the experiment. Additional details may be found in Dejeans et al. (2017). Additionally, results of a sensitivity analysis performed on the grid refinement can be found in Appendix A.1.

2.3.2 Model calibration

As the model forcing at open boundaries was derived from observations collected at the ends of the domain, the calibration of the model was achieved by comparing the predictions with observations of water levels and depth-averaged velocities from the central observation point (red cross on Figure 2.1c). A range

of uniform and spatially varying Chézy coefficients were used to test the model performance. The best calibration was achieved with a uniform Chézy coefficient of $50\,\mathrm{m}^{1/2}.\mathrm{s}^{-1}$. Figure 2.3 shows model predictions plotted against the corresponding observations from the middle site. Some of the discrepancies are likely to be attributed to the interpolation of the bathymetry in certain areas of the domain, which might fail to represent some of the smaller features which could explain the delay between predictions and observations (Figure 2.3). Mean absolute errors (MSE) were 0.232 m for water levels, and 0.024 and $0.002\,\mathrm{m.s}^{-1}$ for the horizontal and vertical components of current velocity, respectively, corresponding to Brier skill scores (BSS) of 0.675, 0.793 and 0.578. Thus, the calibration was classified as 'excellent' using the scheme of Sutherland et al. (2004). Some of the flow characteristics have been shown to be sensitive to grid cell sizes (e.g., Ralston et al., 2017; Bomers et al., 2019). The aim of the present study is to investigate the performance of a relatively standard model in a Lagrangian frame of reference. We conducted a number of simulations to examine the sensitivity of the results to grid sizes (using grid sizes from about $15 \times 3\,\mathrm{m}$ to about $2 \times 1.5\,\mathrm{m}$). While a more detailed calibration was precluded by the dataset collected (which predominantly consisted of Lagrangian measurements), the model was not overly sensitive to grid size and the 2×1.5 m resolution model showed a reasonable ability to reproduce the water elevation and the depth-averaged velocity components, and was therefore considered to be sufficient for this purpose, given the computational resources available. Further refinement of grid not only lengthened model run times, but also substantially increased time to post-process model output.

2.3.3 Model validation

Since no additional data were available to more comprehensively validate the Kaipara model developed for the purpose of the present research, the numerical approach was additionally validated by comparing Delft3D results with laboratory measurements of flow in a sharp bend reported by Blanckaert in

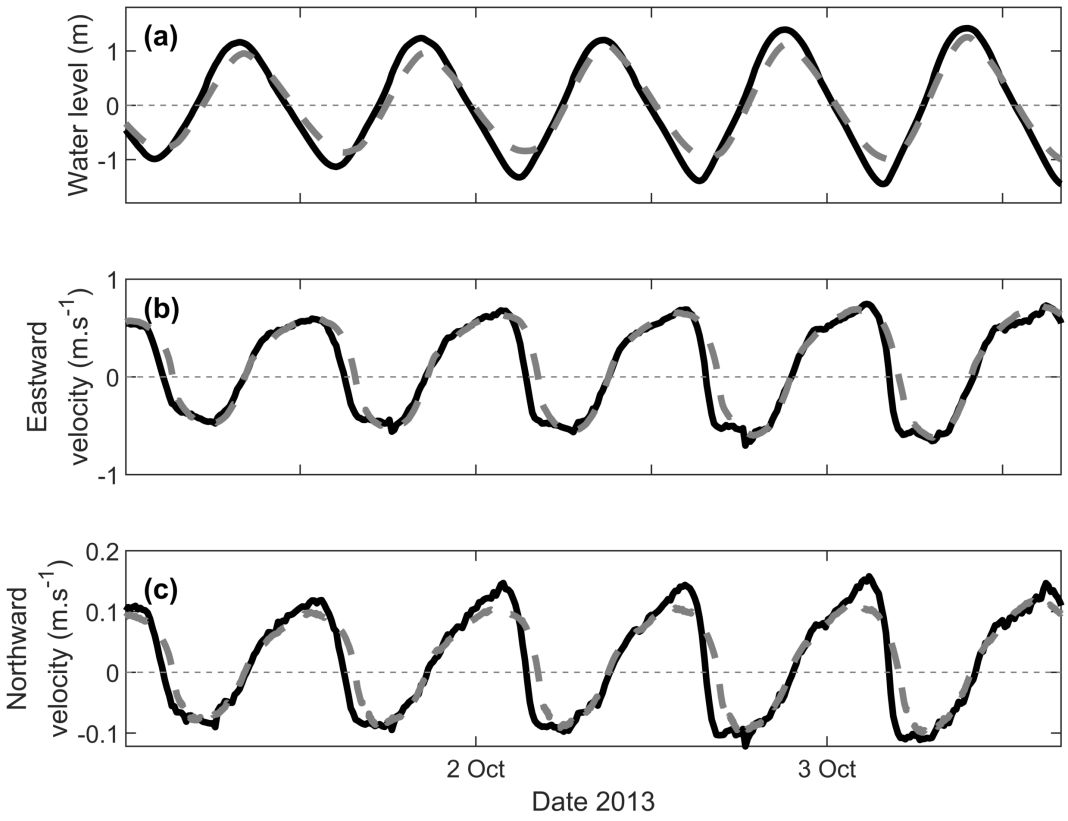

Figure 2.3: Observed (thick black lines) and predicted (dashed grey lines) water levels (a), depth-averaged East (b) and North velocity components at the middle site (red cross on Figure 2.1), averaged over 10 minutes.

2009 and 2012. We created a Delft3D model to reproduce numerically the flume experiment conducted by Blanckaert (2009, 2012). The grid was created so that the aspect ratios (horizontal to vertical) were close to those used in the Kaipara model of the present paper. Despite some limitations, we conclude that the Delft3D approach is satisfactory for the purpose of the present study. Details are given in Appendix.

2.3.4 Data processing

In order to compare the numerical model predictions with the observations collected in a Lagrangian frame of reference, at each time step, the predicted values of the parameters of interest (e.g. velocity, turbulent energy dissipation (ϵ) were extracted from the grid cell corresponding to the measured GPS locations of each drifter. The values were extracted from the σ-layer corre-

sponding to the depth of the drifter below the surface. On occasion the drifter location corresponded to a dry cell close to the edge of the model domain owing to slight errors in GPS positioning or the interpolated bathymetry in the shallow regions. The values at these times were excluded from the analysis. We note that, since the velocity could not be reproduced perfectly, selecting the grid cell by using the GPS location of the observations does not provide strictly 'flow-following' predictions relative to the model. However, extracting the model results from the locations corresponding to the drifter positions at each time step ensures that the observed and predicted velocities are compared at the same location all along the drifters' tracks and prevent a potential intensification of the errors as the drifter moves downstream.

2.4 Results

Winds were generally light during the experiment: data from two nearby weather stations located about 30 km SE from the study site for day 1 and 30 km NE for days 2 and 3 were collected (two stations were needed in order to cover the three days of the experiment because of the availability of the data; however, sections of overlapping data on day 2 revealed winds were similar between stations). The wind observations indicated mean (maximum) speeds of about 4.3 (10.8), 4.3 (9.7), 4.4 (8.9) $\mathrm{m.s^{-1}}$ during the drifter releases on days 1, 2 and 3, respectively. According to measurements taken $\sim$25 km upstream of the drifters' release location, the river discharge was relatively low ($4.3\,\mathrm{m^3\,s^{-1}}$ decreasing to $2.6\,\mathrm{m^3\,s^{-1}}$) during the time of the deployment.

2.4.1 Velocities and salinity

As discussed in Section 2.3.2, the model performs well when comparing predicted and observed water levels and depth-averaged velocities using a 'standard' Eulerian approach (see Figure 2.3). Therefore, we focus here on the structure and model-data comparison of flow variables in a Lagrangian frame

of reference, as the drifters are advected downstream. As mentioned in Section 2.3.4, the Lagrangian comparisons correspond to observed values averaged over a small (73 cm) profile and predicted values were taken from the corresponding model layer.

Figure 2.4 shows an example of comparison of the flow-following predicted velocities (black crosses) and the corresponding (in terms of both time and position) observations (grey stars). Generally, velocities tend to be slower around the bends (indicated by dashed lines) and increase along straighter sections of the river both in the observations and the predictions (e.g. Figure 2.5 a and b). While the observations exhibit greater variability, in general the overall magnitude and gradual increase in flow speeds downstream are relatively well-reproduced. Table 2.2 gives the mean absolute errors between model predictions and observations. However, some features are not well-reproduced by the model. In particular, abrupt changes in velocities are often not predicted by the model, especially around the meanders (e.g. around 5000 m on Figure 2.4 b).

Table 2.2: Mean squared errors (MSE) of the model predictions of horizontal flow speeds and of the dissipation of turbulent kinetic energy (ϵ).

Day	Drifter	MSE of velocities ($m.s^{-1}$)	MSE of $\log_{10}\epsilon$ ($m^2.s^{-3}$)
01/10/2013	01	0.0105	0.1969
02/10/2013	01	0.0129	0.2675
02/10/2013	02	0.0091	0.2434
02/10/2013	03	0.0128	0.1503
03/10/2013	01	0.0152	0.4095
03/10/2013	02	0.0178	0.4113
03/10/2013	03	0.0162	0.2801

During each day, some sections of the river were measured by two drifters, but at different times. Similarly sections of the river were repeatedly covered over multiple days, giving an insight into the controls on variability of the flow characteristics as tidal conditions changed. Generally, both observations and predictions show flow patterns are consistent both across different stages of the same tide (not shown) and across different days (e.g. Figure 2.6), suggesting

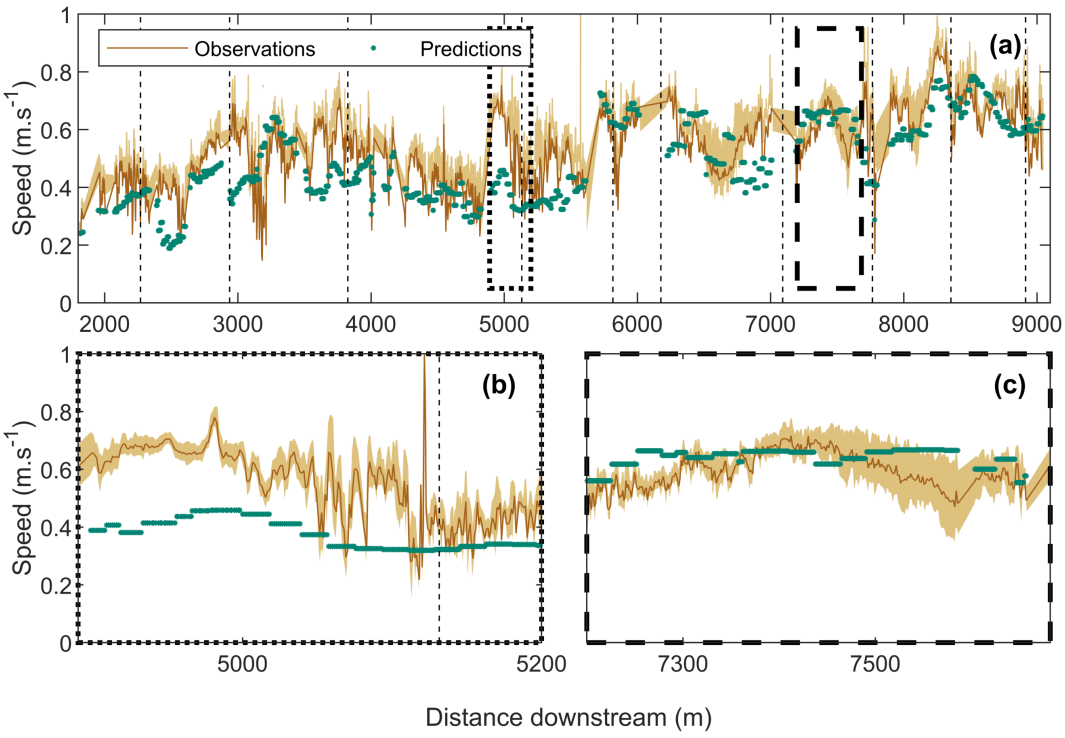

Figure 2.4: Example of the Lagrangian distribution of horizontal flow speeds observed during the experiment (depth-averaged over a 73-cm profile, brown line) and predicted by the model (green crosses) - (a) Example of the drifter deployed furthest upstream, on October 3rd 2013. (b) an example of a section where the velocities are poorly predicted by the model and (c) a section where the velocities are relatively well reproduced. Note: vertical dashed lines in (a) indicate a bend in the river and the grey areas represent the standard deviation calculated over the 73-cm profiles over which the speed values were depth-averaged.

that the predominant control on the flow structure is the bathymetry and geometry of the river. Nevertheless, variations between times are apparent at some locations in the observations, but are not reproduced by the model. For instance, Figure 2.6 shows that around 3000 m, flow velocities reach a local maximum on day 3 (peak reaching about 0.6 m.s^{-1}) whereas a local minimum can be observed around the same location on day 1 (reaching about 0.3 m.s^{-1}). The model, however, predicts local minima of flow velocities for all three days, suggesting the local maxima observed on day 1 can be attributed to a factor not taken into account into the model (e.g. wind).

As the drifters were close to flow-following, the observed salinity did not

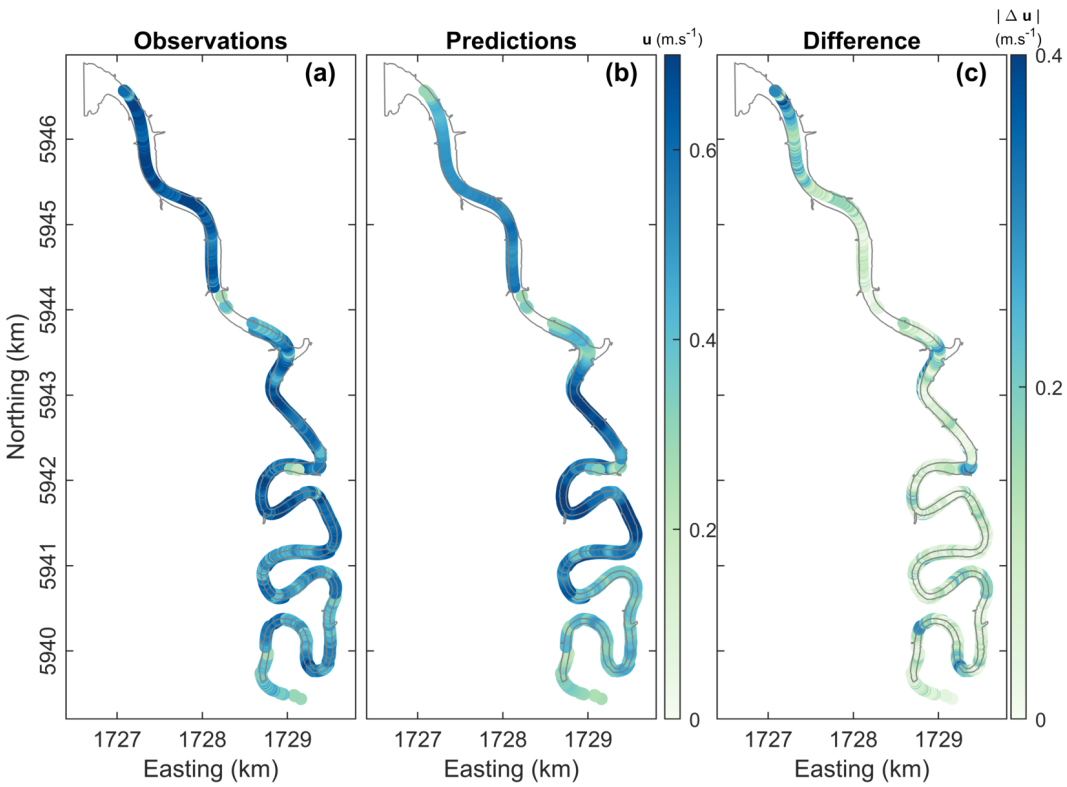

Figure 2.5: (a) Observed (depth-averaged over a 73-cm profile) and (b) predicted horizontal flow speeds and (c) absolute difference between observations and predictions for day 3. A few points (less than 1%) had differences between observations and predictions above 0.4 $\mathrm{m.s^{-1}}$ and appear in dark blue.

change along the track of each drifter. The salinity was from close to 0 for the upstream-most drifter to around 10 psu for the drifter released closest to the river mouth. However, because of the slight under-predictions of the velocities by the model, there is a delay for the predicted flow to reach the grid cells corresponding to the locations of the observations, therefore, since salinity increases gradually downstream, the model slightly over-predicts the Lagrangian salinities (results not shown here).

To explore quantitative links between the discrepancies between model and observations and the river curvature, we calculate a local sinuosity index along the river. The index, SI is defined as along-channel length/straight-line distance between two points, with values centred in a moving window of fixed along-channel distance of 100 m (thus a value of $SI = 1$ indicates a perfectly straight section) (Figure 2.7a). The raw data, corresponding to the three

drifters on the three days, are quite widely spread (Figure 2.7b, light grey crosses) and have therefore been bin-averaged (into bins of width $\Delta SI = 0.004$) in order to highlight a potential relationship between the errors in velocity predictions and sinuosity. However, no significant quantitative relationship could be determined between errors in velocity predictions and sinuosity (Figure 2.7b). We note that while absolute values of the local sinuosity index depend on the size of the along-river window, the relationships between variables were not found to be sensitive to window size.

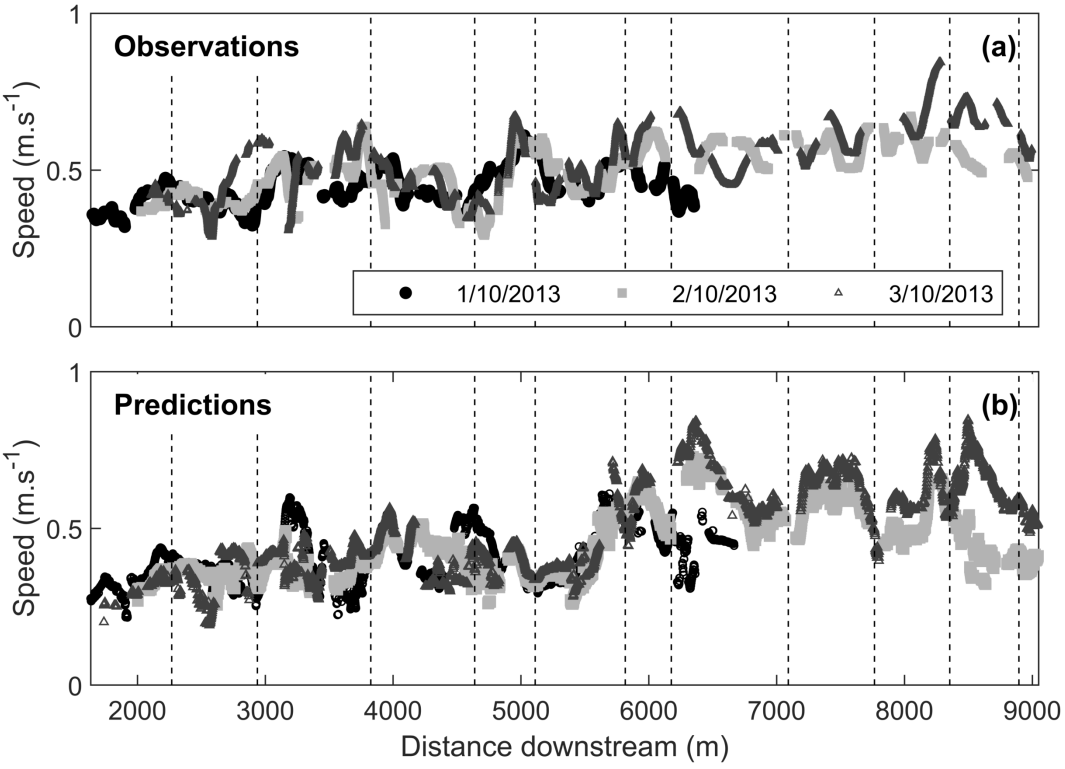

Figure 2.6: (a) Observations of horizontal flow speeds collected on day 1 (black circles), day 2 (light grey squares) and day 3 (dark grey triangles) by the drifter released upstream of the domain and (b) the corresponding numerical model predictions. Observations (a) have been smoothed with a 21-pt running mean. Note: vertical dashed lines in the panels above indicate a bend in the river.

2.4.2 Dissipation rate of turbulent kinetic energy

Overall, the model generates the same order of magnitude of values for the dissipation rate of turbulent kinetic energy as the observations along the river. The model also reproduces some of the general patterns of the distribution

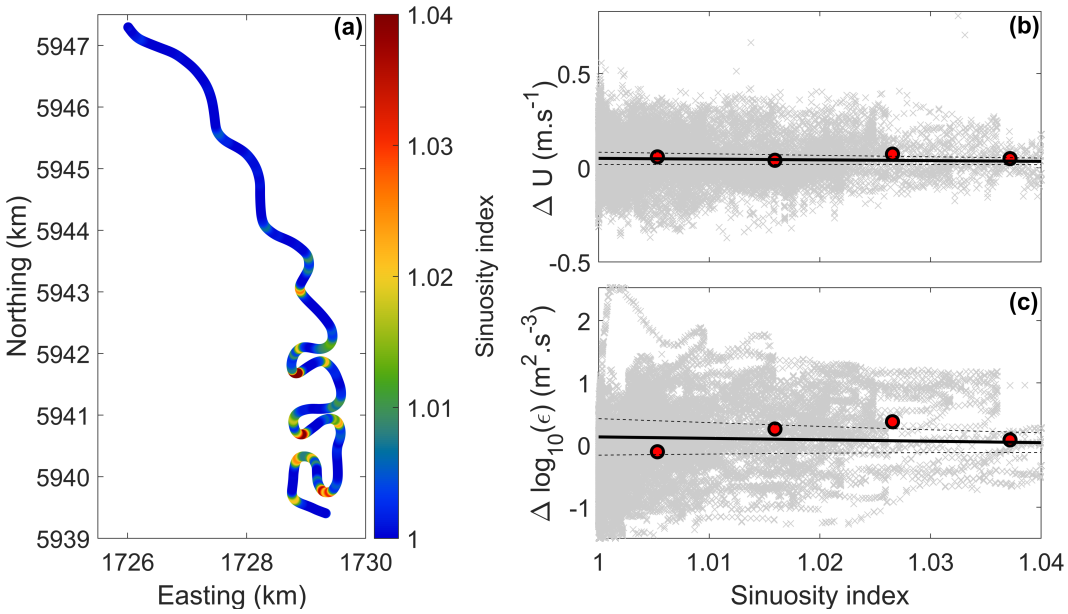

Figure 2.7: (a) Along-river sinuosity index. Differences between observed and predicted flow-following (b) horizontal flow speeds and (c) dissipation rates of turbulent kinetic energy. All data is shown in grey, circle are bin-averaged data (bins in sinuosity index of width 0.004), with linear fit shown in thick black lines (with (b) $r^2 = 0.27$, p-value= 0.13 and (c) $r^2 = 0.13$, p-value= 0.30). The dashed lines show 95 % confidence intervals.

of turbulent energy dissipation observed along the river, with better model performance further downstream, where the model captures the general pattern, although slightly under-predicts the magnitude (e.g. Figures 2.8 and 2.9, which show results from day 3). The values of modelled ϵ range between 5.23×10^{-7} and $1.5 \times 10^{-3}\,\mathrm{m^2.s^{-3}}$ whereas the observations vary between 2.75×10^{-6} and $4.57 \times 10^{-4}\,\mathrm{m^2.s^{-3}}$. The model mainly underpredicts turbulent dissipation (with an average difference between predictions and observations of $7.25 \times 10^{-5}\,\mathrm{m^2.s^{-3}}$ and reaching a maximum of about $1.5 \times 10^{-3}\,\mathrm{m^2.s^{-3}}$ locally, Table 2.2).

Despite general order-of-magnitude agreement, most of the smaller scale structures in the distribution of ϵ are not well reproduced by the model, with the largest discrepancies between model and observations occuring at bends (Figure 2.9). The predicted ϵ is consistently smaller around the bends (which can be seen, for example, on day 3 at the upstream part of the domain on Figures 2.8 and 2.9c in the model predictions, whereas the observations

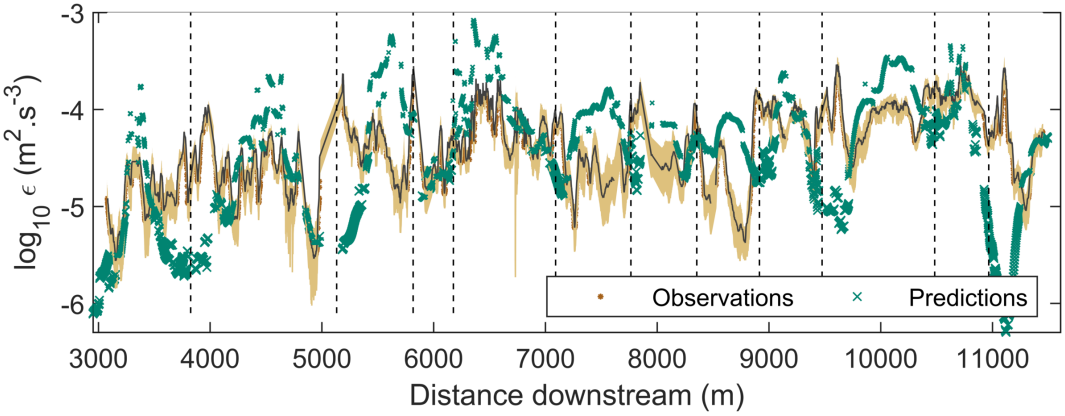

Figure 2.8: Observed (brown circles) dissipation rates of turbulent kinetic energy from the drifter released at the most upstream location on day 3 (values depth-averaged over a 73-cm profile) and the corresponding predictions (green crosses). Note: vertical dashed lines in the panel above indicate a bend in the river and the grey areas represent the standard deviation calculated over the 73-cm profiles over which the ϵ values were depth-averaged.

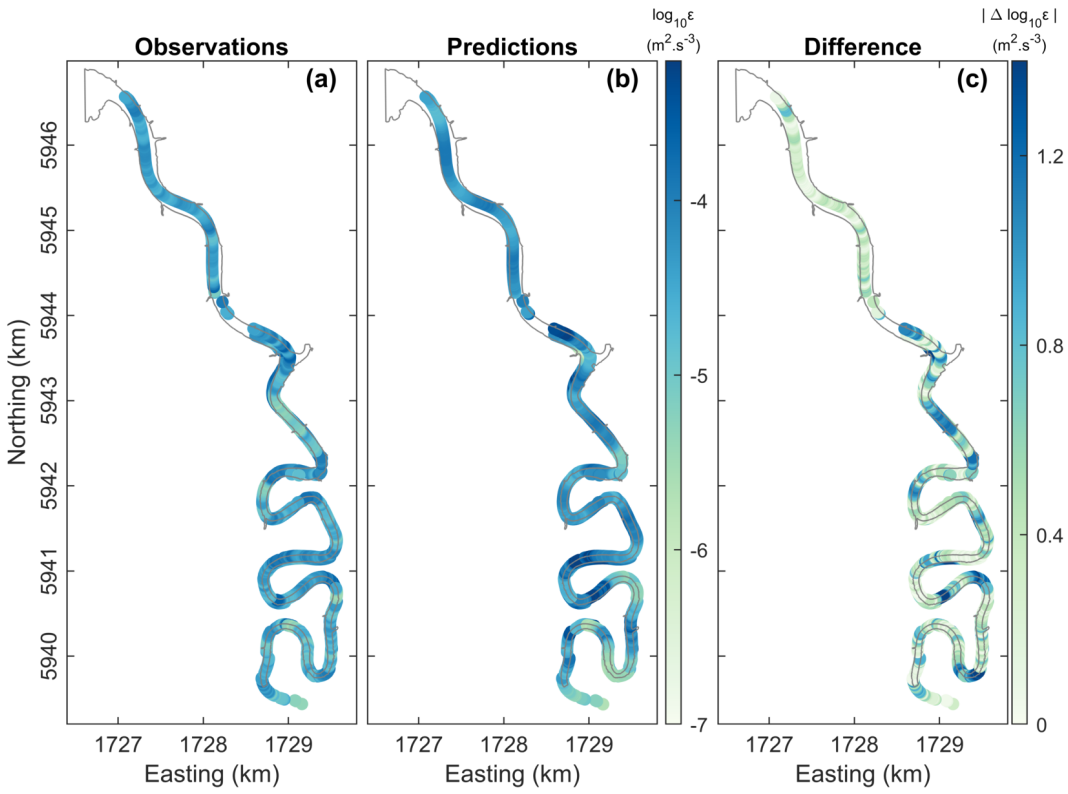

Figure 2.9: (a) Observed (depth-averaged over a 73-cm profile) and (b) predicted dissipation rates of turbulent kinetic energy and (c) absolute difference between observations and predictions on day 3. A few points (less than 1%) had differences between observations and predictions above $1.4\,\mathrm{m}^{-2}.\mathrm{s}^{-3}$ and appear in dark blue.

show larger dissipation rates ϵ at these locations). As with the along-river distribution of velocities, predicted dissipation rates between the overlapping sections are often similar, despite the fact that rates correspond to different phases of the tidal cycle. However, at some locations, the observed dissipation rates of turbulent kinetic energy are not always consistent between the days. For instance, around 6000 m, the upstream drifter records observed ϵ around $5.0 \times 10^{-5}\,\mathrm{m^2.s^{-3}}$ on days 1 and 3 but observations drop to almost $6.0 \times 10^{-6}\,\mathrm{m^2.s^{-3}}$ on day 2, which is not reproduced by the model (e.g. Figure 2.10).

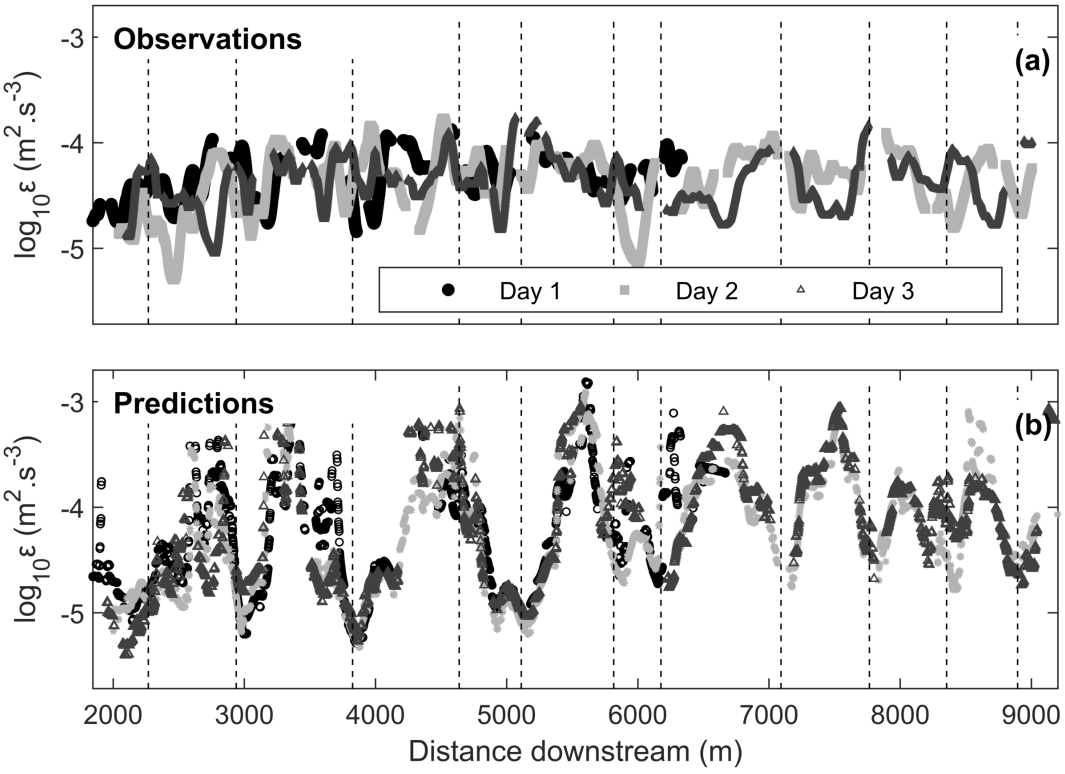

Figure 2.10: (a) Observations of turbulent energy dissipation rates collected on day 1 (black circles), day 2 (light grey squares) and day 3 (dark grey triangles) by the drifter released from the most upstream location and (b) the corresponding model predictions. Data smoothed with a 21-pt running mean. Note: vertical dashed lines in the panels above indicate a bend in the river.

The potential quantitative relationship between errors in model predictions of ϵ and sinuosity have also been investigated (Figure 2.7c). The raw data (all drifters on all data, Figure 2.7c, light grey crosses) also exhibit substantial scatter, and the bin-averaged results also do not exhibit any strong quantitative

relationship between sinuosity and errors. However, a qualitative assessment of the results, as displayed for instance in Figures 2.8 and 2.9c, tends to show that the model consistently performs relatively poorly around the bends.

2.4.3 Vertical structure of velocities and turbulence dissipation

The model also provides an opportunity to examine full-depth vertical profiles of relevant parameters including velocity and energy dissipation. Full-depth vertical velocity and ϵ profiles were not obtained in the field; however, the ADCP observations provide the vertical distribution of those two parameters along short profiles (about 0.73 m). Figure 2.11 compares examples of short observed (solid lines) and full-depth predicted (dashed lines) profiles of flow speeds (Figure 2.11b) and ϵ (Figure 2.11c) at four different times and locations. As expected, velocity profiles generally display a logarithmic shape and tend to decrease with depth (e.g. Figure 2.11b). The four profiles tend to be underpredicted compared to the observations. The vertical profiles of dissipation predicted by the model are also close to a logarithmic shape, with larger ϵ near the bed. This trend is globally consistent with ADCP observations, which show that ϵ increases with depth (noting again that observed profiles did not encompass the full water column). All four profiles show the trend seen in the observations of increasing dissipation rates with depth (Figure 2.11c). Two of the model predictions of ϵ are of the same order of magnitude as observations (green and purple). However, the dissipation rate is underpredicted for two of the profiles (blue and orange). The discrepancy of the green profile is likely owing to turbulence generated by small waves as the profile is located along a straight stretch of the river. Although the vertical distributions show a general tendency to underpredict speed and energy dissipation, the orders of magnitude of predictions are close to observations.

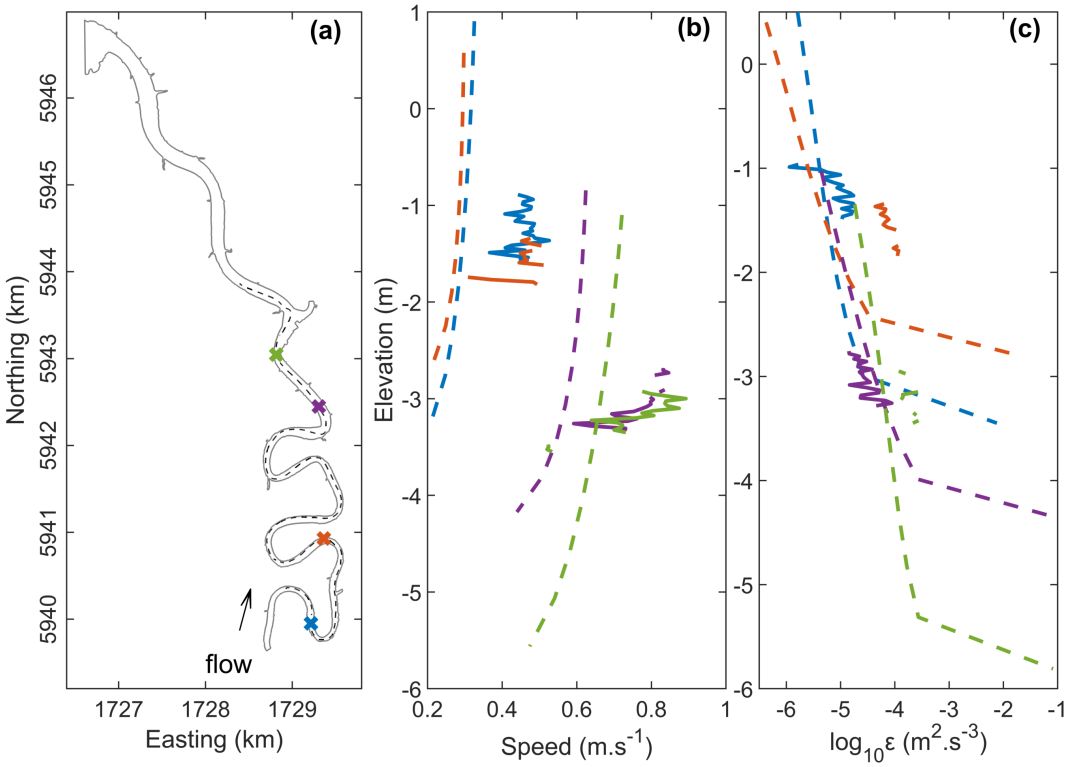

Figure 2.11: Examples of vertical profiles of speed and turbulent energy dissipation rates at four different locations. The crosses on (a) represent the location of the profiles of speed and ϵ shown on (b) and(c), respectively. The solid lines are the observations and the dashed lines are the model predictions.

2.5 Discussion

Generally, the flow following distribution of the model predictions is reasonably consistent between different days and at different times of an individual tide, both for velocity and turbulent dissipation rates, which suggests that the geometry and bathymetry of the river is the main driver influencing turbulence in the model (e.g. of the drifter released upstream on Figure 2.10). However, some variability appears in the observations between the different days which is not reproduced by the model. Some of the differences can probably be explained by the lack of wind forcing in the model. Past studies have indeed shown that winds can induce vertical mixing and favour the destratification of the water column (e.g., Chao, 1988). When breaking, waves are likely to increase the production of TKE near the surface by transfer of momentum

(Thorpe, 1995; Burchard et al., 2008). During the field experiments, although the winds were generally weak (MacDonald and Mullarney, 2015), on occasion small wind-waves were observed on straighter sections with sufficient fetch. Thus, it is likely that winds can contribute to some of the differences in observations between days, however, it is unlikely all of the discrepancies between observations and predictions of velocities and energy dissipations are driven by the winds. The distribution of dissipation rates varied several orders of magnitude along the river, with the greatest values located in the section of the domain displaying the sharpest bends. The effects of bathymetry in meandering rivers, and especially the presence of shoals and 'pools' (i.e. deeper parts of the river), on turbulent flows have been described by Sukhodolov (2012) and match the results from the present model, generally displaying smaller turbulence in deepest pools. Overall, the general order of magnitude of energy dissipation predicted by the model is similar to the observed values. However, the performance of the model in predicting ϵ is quite uneven along the river. Indeed, some of the observations appear to be relatively well reproduced by the model but variation across smaller temporal and spatial scales do not seem to be captured. For instance, in Figure 2.8, between 5900 and 6500 m, the model reproduces the general increase in turbulence observed around the bend but does not show the local maximum at around 6050 m. Although no clear quantitative relationship could be established between the errors in velocities and the sinuosity of the river, bin-averaged differences between observed and predicted ϵ show a slight linear correlation with increasing sinuosity. This correlation between sinuosity and errors in predictions of turbulence is anticipated based on the reported difficulties of the Delft3D RANS approach in sharp bends (Van Sabben, 2010). For the benchmark experiments of flow in a sharply curved channel (Blanckaert, 2009; Blanckaert et al., 2012), RANS-based simulations by both Van Sabben (2010) and Zeng et al. (2008) were unable to simulate coherent structures such as streamwise-oriented vortices and shear layer eddies (attributed in part to the inability to resolve turbulence

anisotropy). However, more recent work focused on hybrid approaches such as Detached Eddy Simulation (DES) offers substantial potential. High-resolution DES simulations by Koken et al. (2013) of the Blanckaert (2009) laboratory experiments were able to successfully capture the complex structure of the secondary flow and accurately reproduce the observed streamwise vorticity fields. The results from their very fine-scale eddy-resolving models were then used to suggest modified parameterisations for sediment entrainment for incorporation into RANS-based models (Koken et al., 2013). Previous use of a similar correction factor for turbulence effects has been shown to yield substantial improvements in morphological predictions in open channel flow (e.g., Kraft et al., 2011).

The model also allowed examination of the vertical structure of turbulence. We note that the model validation has shown that the model does not accurately reproduce the vertical distribution of TKE, especially in the bends (see Figure A.3 in A). However, the overall shapes of the predicted vertical profiles of ϵ, k and ν are relatively similar to profiles found in past studies. We note that the model results discussed here are only numerical predictions and could not be compared to observations along cross-sections as these were not part of the observations collected. However, the model predictions of eddy diffusivity, eddy viscosity, turbulent kinetic energy and dissipation of turbulent kinetic energy in the vertical were broadly consistent with field observations, such as the ones collected in a deep channel by (Sukhodolov, 2012) and model simulations, including results from two-equation turbulence models such as the ones reported by (Warner et al., 2005). Indeed, similarly to the predictions of model (e.g. Figure 2.12c), past studies have observed the dissipation of turbulent kinetic energy ϵ to be minimum at the water surface and to increase with depth, with an approximately logarithmic shape (e.g., Warner et al., 2005). The vertical distribution of the turbulent kinetic energy k in the present work is also consistent with past studies. More precisely, the increase in k is close to linear with depth for most of the water column (from about 0.5 m below the surface

to 0.5 m above the bed), with smaller variation at the surface and the bed (e.g. Figure 2.12c). Consistent with field observations (e.g., Sukhodolov, 2012) and model predictions (e.g., Warner et al., 2005), both vertical eddy viscosity and diffusivity are minimum at the surface, reach a maximum around mid-depth and another minimum at the seabed. Alternatively, Feddersen et al. (2007), who calculated the dissipation of turbulent kinetic energy based on ADCP observations in relatively shallow environment (nearshore region where the mean water depth was about 3 m), showed that the turbulent dissipation reached a maximum near the water surface. This maximum is, however, probably induced by wind as previously mentioned which is not taken into account in the present model. Similar to the predictions of the present model, Feddersen et al. (2007) observed that values of ϵ tend to increase with depth and reach a second maximum close to the bed, which they explained by the reduction of the turbulent length scale towards the bed. Additionally, field measurements collected in other meandering rivers showed turbulent kinetic energy to be relatively small at the free water surface and to increase toward the riverbed (e.g., Abad et al., 2008; Sukhodolov, 2012). The values of TKE in the present work (which shows a maximum TKE of about $4 \times 10^{-3}\,\mathrm{m^2.s^{-2}}$) are larger than the values observed by Sukhodolov (2012) (who shows a maximum TKE of about $1.6 \times 10^{-3}\,\mathrm{m^2.s^{-2}}$ and an increase of about 2 orders of magnitude from the water surface towards the seabed) but are similar to the values observed by Abad et al. (2008) (maximum TKE of about $9.0 \times 10^{-3}\,\mathrm{m^2.s^{-2}}$ with an increase of about 3 orders of magnitude from the water surface).

Despite many simplifications in model forcing, on the whole, the calibrated model qualitatively and quantitatively reproduces the general pattern of the Lagrangian distribution of the velocity and the turbulent energy dissipation collected by the drifters. Drifters have proven valuable in the past, including, more recently, in shallow environments (e.g., Schmidt et al., 2003; Suara et al., 2018; Heer et al., 2020). However, a unique feature of the present work is the comparison of Lagrangian observations of turbulence with model predictions.

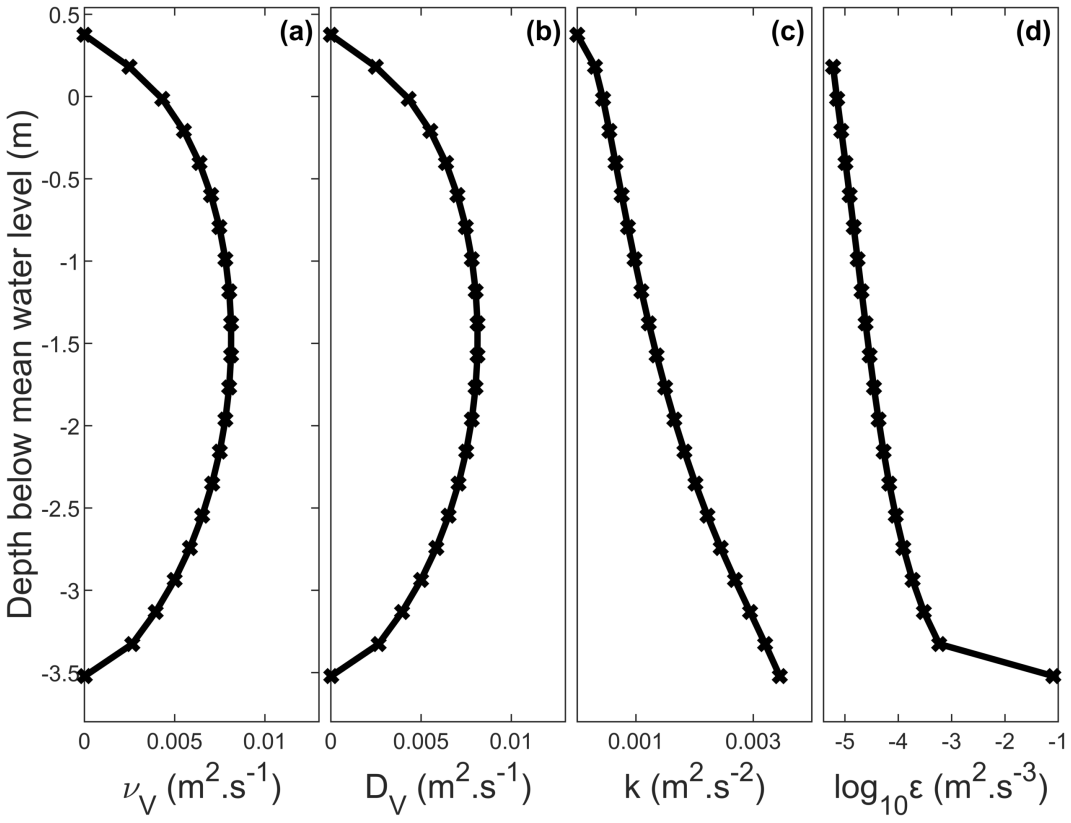

Figure 2.12: Examples of vertical profiles of (a) vertical eddy viscosity (b) vertical eddy diffusivity, (c) turbulent kinetic energy and (d) dissipation rate of turbulent kinetic energy predicted by the model at the location marked by a blue cross on Figure 2.1.

Although no cross-sectional data were included in the validation of the model (as the field deployment favoured the collection of an extensive Lagrangian dataset over cross-sections), we believe that the similarity between the Lagrangian predictions and the observations strengthens the confidence in model results. This approach provides an insight into the performance of the model over the full along-river scale and at different times. Lagrangian observations showed that dissipation of turbulent kinetic energy could vary up to 2 orders of magnitude over the whole domain; for instance, on the third day, the drifters recorded values of ϵ between about 2.0×10^{-6} and $9.4 \times 10^{-4}\,\mathrm{m^2.s^{-3}}$ (Figure 2.8). Strong variations in ϵ can also be observed at smaller scales, and notably around the bends, as previously noted. For instance, around the 5000 m, the dissipation of k changes from about 3.2×10^{-6} and $2.5 \times 10^{-4}\,\mathrm{m^2.s^{-3}}$ on the third day along about 100 m (e.g. Figures 2.8 and 2.9a). Results computed by

the model show that the dissipation of turbulent kinetic energy increases quite significantly from the surface to the water bed (variations of up to 3 orders of magnitude). With Eulerian deployments, it would be logistically challenging to capture these different scales of variability in turbulence, requiring many instruments, positioned at least every 100 m along the river. Observing such variability of turbulence over different spatial scales using drifting instruments is therefore much more efficient in terms of resources.

2.6 Conclusions

Turbulence plays a crucial role in sediment transport in estuaries and coastal waters. Our ability to manage riverine environments depends in part on our ability to model fine-sediment dispersal and settling. A key component of this modelling is the accurate representation of turbulence within our hydrodynamics and sediment transport models.

Within the framework of the present study, a model of the tidally driven Kaipara River was developed with the Delft3D software, using the $k - \epsilon$ turbulence closure scheme. A 'typical' calibration approach using Eulerian time series data of water levels and depth-averaged velocities gave excellent results. However, in a novel approach the model results were also compared with the Lagrangian observations of velocities and dissipation rate of turbulent kinetic energy along almost 15 km of the river over three flood tides (occurring on three different days).

While in general, the model reproduces relatively well the observed velocities recorded by the drifters and order of magnitude estimates of the dissipation rate of turbulent kinetic energy. The model did fail to reproduce some of the observed smaller-scale patterns of variability. The observations showed that dissipation rates varied significantly over short temporal and spatial scales, with the structure controlled largely by the bathymetry and geometry of the river. Predicted estimates of dissipation rates were typically lower than ob-

served. The model also tended to under-estimate dissipation on bends, possibly owing to missing or incorrectly represented processes (e.g. secondary flow).

Characteristics of turbulent flow in meandering channels have been extensively studied in the past. Such works have usually been based either on field experiments, including the successful use of drifters to derive turbulent quantities, and hydrodynamic modelling, which have proven to be powerful tools to investigate the flow over large spatial scales and long time scales. However, this paper has presented a novel approach, consisting of using a very high-resolution Lagrangian dataset, which encompasses both a relatively large spatial scale (reaching about 15 km) and long time scale, to observe the performance of a standard hydrodynamic model. This Lagrangian approach provides a robust mechanism enabling to explore how well the model reproduces the observations over a wide range of scales and helps highlight how turbulence can evolve over different scales.

Acknowledgments

This work has been supported by NIWA's core programme Catchment to Estuaries in the Freshwater and Estuaries Centre. We thank Glen Reeve for his assistance with the initial set up of the model. We also thank Dave Bremner, Rod Budd, Scott Edhouse, Sam Parkes, Mark Pritchard and Glen Reeve for their assistance with the field work. We also thank Prof. Koen Blanckaert for giving us access to the dataset of their laboratory experiment in order to further validate our model. We also thank Jeff Nittrouer and two anonymous reviewers for their careful reading and insightful feedback to this manuscript. The Lagrangian observations and predictions of flow speed and dissipation rates of turbulent kinetic energy can be found at zenodo.org. [Data set]. Zenodo. http://doi.org/10.5281/zenodo.4296975

Chapter 3

Evaluation of the performance of two turbulence closure schemes in a Lagrangian frame of reference along a fluvial-to-marine transition zone

Contribution of authors

Chapter 2 duplicates a paper entitled "Evaluation of the performance of two turbulence closure schemes in a Lagrangian frame of reference along a fluvial-to-marine transition zone", by Bérengère S. Dejeans, Julia C. Mullarney and Iain T. MacDonald, which will be submitted to *Water Science and Engineering* in 2023. I developed the Delft3D numerical model. Iain MacDonald and Julia Mullarney provided me with the field observations. I wrote codes in Matlab in order to process and analyse the model results, as well as making all the figures. My co-authors, Julia Mullarney and Iain MacDonald help me with data analysis, interpretation of results, and paper writing by providing me direction and helpful comments.

Abstract

Various strategies can be adopted to model turbulence, relying on different principles of flow dynamics. Statistical methods, which are usually more computationally efficient than other methods, all rely on the Reynolds-Averaged Navier-Stokes (RANS) equations. After assumptions and simplifications, the RANS equations can be closed using different turbulent closure schemes, which vary in their prescription of turbulent quantities. The present paper uses a Lagrangian approach to provide a robust comparison of predictions of speed and dissipation rates of turbulent kinetic energy ϵ given by two of the closure schemes implemented in Delft3D, namely k-L and k-ϵ, with a unique set of Lagrangian observations collected along the meandering tidal Kaipara river. Our results show that predictions were not sensitive to the closure scheme; both were able to predict the right order of magnitude and general pattern of flow speeds and dissipation rates of turbulent kinetic energy. However, neither scheme could accurately reproduce variations in ϵ across smaller-scales. Additionally, the discrepancies between model predictions from both closure schemes and observations are shown to be larger around the bends compared to the straighter sections of the river domain. The performance of the k-L closure scheme was slightly better than the k-ϵ scheme, implying that even though modelling studies often select the 'default' more sophisticated turbulence closure scheme, simpler formulations of turbulence might give similar or even better results, and save on computational time and resources.

3.1 Introduction

Riverine and coastal environments are increasingly stressed by the input of pollutants, nutrients and sediments (e.g., Hyland et al., 1999; Yuan et al., 2001; Elliott and Quintino, 2007). For those working in the environmental management area, the ability to accurately predict movement and mixing of water masses with numerical hydrodynamic models is a crucial tool. This transport of momentum, heat, salt and sediment is often strongly influenced by turbulence in aquatic environments (e.g., Burchard et al., 2008). In particular, turbulence in rivers can influence flocculation processes, which subsequently affects the delivery and deposition of sediments to downstream coastal environments.

Flow dynamics can be described by a set of equations comprising the momentum equations, the continuity equation (conservation of mass) and the conservation laws for heat and salt. In numerical models typically used by practitioners, one common way to represent turbulent processes is through use of the Reynolds-Averaged Navier-Stokes (RANS) equations, which are a derivation of the Navier-Stokes equations in which the Reynolds decomposition (separating the quantities into mean value and a fluctuating part) has been applied before ensemble-averaging the result. This process leads to the apparition of new unknown second moments in the equations, namely the Reynolds stress, the turbulent heat flux and the turbulent salt flux (e.g., Burchard et al., 2008). In order to make the RANS equations solvable over numerical grids, multiple assumptions and simplifications are made (Sander, 1998), such as the assumption that the system is in local equilibrium. Additionally, the next usual step is to neglect the horizontal mixing terms (called the boundary layer assumption, noting this assumption is only realistic if the activity of the horizontal eddy is well resolved, typically requiring subgriding the numerical resolution) (Burchard et al., 2008). Lastly, the turbulent kinetic energy, TKE or k, the turbulent length scale, L, and the dissipation rate of turbulent kinetic

energy, ϵ, are then either defined as algebraic relations, as transport equations, or as a combination of both algebraic and transport equations in order to close the system of RANS equations (Burchard et al., 2008). Various closure schemes are used, including algebraic (e.g., Burchard and Bolding, 2001), Mellor-Yamada (e.g., Nakanish, 2001), k-L (e.g., Shuai and Agarwal, 2019), k-ω (e.g., Moshonkin et al., 2018), and k-ϵ (e.g., Horstman et al., 2013). While other approaches, such as Direct Numerical Simulation (DNS) or Large Eddy Simulation (LES), can be used to provide better resolution and the ability to solve over smaller scales (e.g., near surface mixed layers) (e.g., Ferziger et al., 2002; Burchard et al., 2008), one advantage of statistical (RANS) techniques is that they tend to be more computationally efficient. Hence, these approaches are often used, particularly to investigate the flow within meandering channels (e.g., Kim et al., 2020).

The divergence between model results obtained using different turbulence closure schemes has been of interest for some years (e.g., Launder et al., 1973). The k-ϵ and the Mellor-Yamada level 2.5 schemes (also a two-equation closure scheme which differs from the k-ϵ in its prescription of the turbulence length scale) were applied to different scenarios (e.g. free convection, stratified boundary layer flow), and the results were compared with observations taken in the lower and upper mixed layer of the North Sea, showing that both turbulence models gave similar predictions (Burchard and Petersen, 1999). However, significant differences between results obtained from different turbulence closures have also been reported (e.g., Wilson et al., 2002). Indeed, comparisons between predictions from a constant eddy viscosity, Elder (which computes the turbulent viscosity using two algebraic equations), and k-ϵ models with observations collected from a laboratory channel, revealed that the constant eddy viscosity model performed less well than Elder and k-ϵ schemes when reproducing the mean flow parameters when in presence of inbanks or low overbanks.

Previous work comparing turbulence closure schemes has focused on the ef-

fects of the chosen scheme on predictions of velocity (e.g., de Almeida and Ota, 2020; Khanarmuei et al., 2020; Mardani et al., 2020). A number of studies use a predominantly qualitative comparison. For example, a study investigated model results of an idealized channel with different sinuosities and found that there were larger differences between results from the k-ϵ, k-ω, and SST k-ω turbulence closure schemes for meander bends with larger sinuosity (Kim et al., 2020). The work qualitatively compared cross-sectional distributions of the model results and found that the choice of turbulence closures clearly affected the water circulation around the bend. More precisely, the study showed that the k-ϵ and the k-ω could not predict the flow separation properly either by not being able to simulate the emergence of the flow separation or by underpredicting the flow reattachment. Many of the previous comparisons between models are also based on 2D models, and therefore often tend to underestimate the diffusion especially in meandering parts of rivers (e.g., de Almeida and Ota, 2020). Another work compared results of a Telemac 2D-model run using three different turbulent closure schemes (constant viscosity, Elder Model and k-ϵ Model) with laboratory observations of the velocity field from a channel composed of bends and straight sections (de Almeida and Ota, 2020). Although the most sophisticated k-ϵ model could reproduce the observations better overall, only the Elder model, simpler in its formulation (as it is based on algebraic relationships) compared to k-ϵ (based on transport equations), proved to be able to predict the anisotropic characteristics of turbulence. ROMS and Delft3D modelling software packages have also been compared by Putzu et al. (2019) who showed that velocity profiles, vertical eddy viscosity and tangential stresses at the bed in a simulation of an inclined rectangular channel were dependent on the turbulent closure schemes. They concluded that neither the k-ω or the k-ϵ closure schemes implemented in ROMS could reproduce the velocity in the bottom layer. Similarly, the k-ϵ closure in Delft3D did not accurately reproduce the velocity at the bed; however, the algebraic and k-L closures did provide satisfactory results in terms of

bed stresses and should therefore be preferred over other schemes, particularly in studies of open channel flows.

A relatively new approach to investigate model performance is to use a Lagrangian frame of reference, which enables the investigation of larger areas and longer time frames which can help improve the validation of hydrodynamic models (Khanarmuei et al., 2019, 2020; Mardani et al., 2020). In a recent study, a Delft3D model of the tidal Kaipara River was developed and validated and assessed the performance of the k-ϵ model in terms of speeds and turbulent dissipation (Dejeans et al., 2022). The results included comparisons of model predictions to observations following an Eulerian approach which yielded a reasonable calibration ('excellent' on a specific classification scheme (Sutherland et al., 2004)). However, a Lagrangian approach revealed deficiencies in predictions over different scales; for instance, some of the patterns of horizontal speed observed along the bends could not be reproduced as well as the patterns observed along straight sections of the river.

The present paper extends on the work of Dejeans et al. (2022), and assesses the performance of two turbulence closure models (k-L and k-ϵ) implemented in Delft3D. More precisely, this work compares the predictions of dissipation rates of turbulent kinetic energy (and velocity) predicted by the hydrodynamic modelling suite Delft3D with high-resolution flow-following observations, in a Lagrangian frame of reference.

3.2 Methods

3.2.1 Study site and data collection

A Lagrangian dataset was collected in the tidally influenced Kaipara River in 2013 using a custom FlocDrifter platform (MacDonald and Mullarney, 2015). Three drifters were deployed in the downstream 15-km of the Kaipara River, which is a heavily sediment-laden meandering river at the Southern end of the Kaipara estuary, a 94,700-ha drowned-valley system, in the North Island of

New Zealand. Within the study area, the width of the river goes from 50 m to 200 m; the depth along the thalweg reaches a maximum of 9.2 m and averages to 4.5 m below MSL. Between one and three drifting platforms were each released from a different location of the river at the beginning of the ebb stage of the tidal cycle on 1-3 October 2013. The platforms were positioned about 1.5 m under the surface of the water and followed the current for about 4 hours each day (Figure 3.1a-c, Table 3.1) (MacDonald and Mullarney, 2015; Dejeans et al., 2022). The three drifter platforms were instrumented with a GPS, a pulse-coherent 2-MHz Nortek Aquadopp Acoustic Doppler Current Profiler (ADCP), to gather short profiles of 3D velocity components, a Nortek Vector Acoustic Doppler Velocimeter (ADV), to collect 3D velocity components at single points (at a sampling rate of 16 Hz), a Sea-Bird Electronics SBE-37 MicroCAT Conductivity-Temperature-Depth (CTD) probe (whose sampling rate was 0.167 Hz). The dissipation rate of TKE was calculated from the short profiles collected with the ADCP using the structure function of Wiles et al. (2006) over 64-s windows.

Table 3.1: FlocDrifters released and retrieval times (Dejeans et al., 2022).

Release date	Drifter	Release time	Recovery time	Length of section covered
01/10/2013	01	10:08:53	14:24:30	5.2 km
02/10/2013	01	10:24:13	14:44:30	7.2 km
	02	10:32:09	14:41:42	7.1 km
	03	11:22:13	14:54:33	6.6 km
03/10/2013	01	10:42:51	15:03:35	7.4 km
	02	10:52:28	15:31:16	9.0 km
	03	11:48:33	15:27:41	7.9 km

3.2.2 Model set up

The presented work is based on a model of the Kaipara River developed with the Delft3D-FLOW software package, which resolves the RANS equations for an incompressible fluid by applying the shallow water and Boussinesq assumptions (Deltares, 2020). Delft3D has been extensively validated for use in estuarine and coastal environments (e.g., Roelvink and Van Banning, 1995; Elias

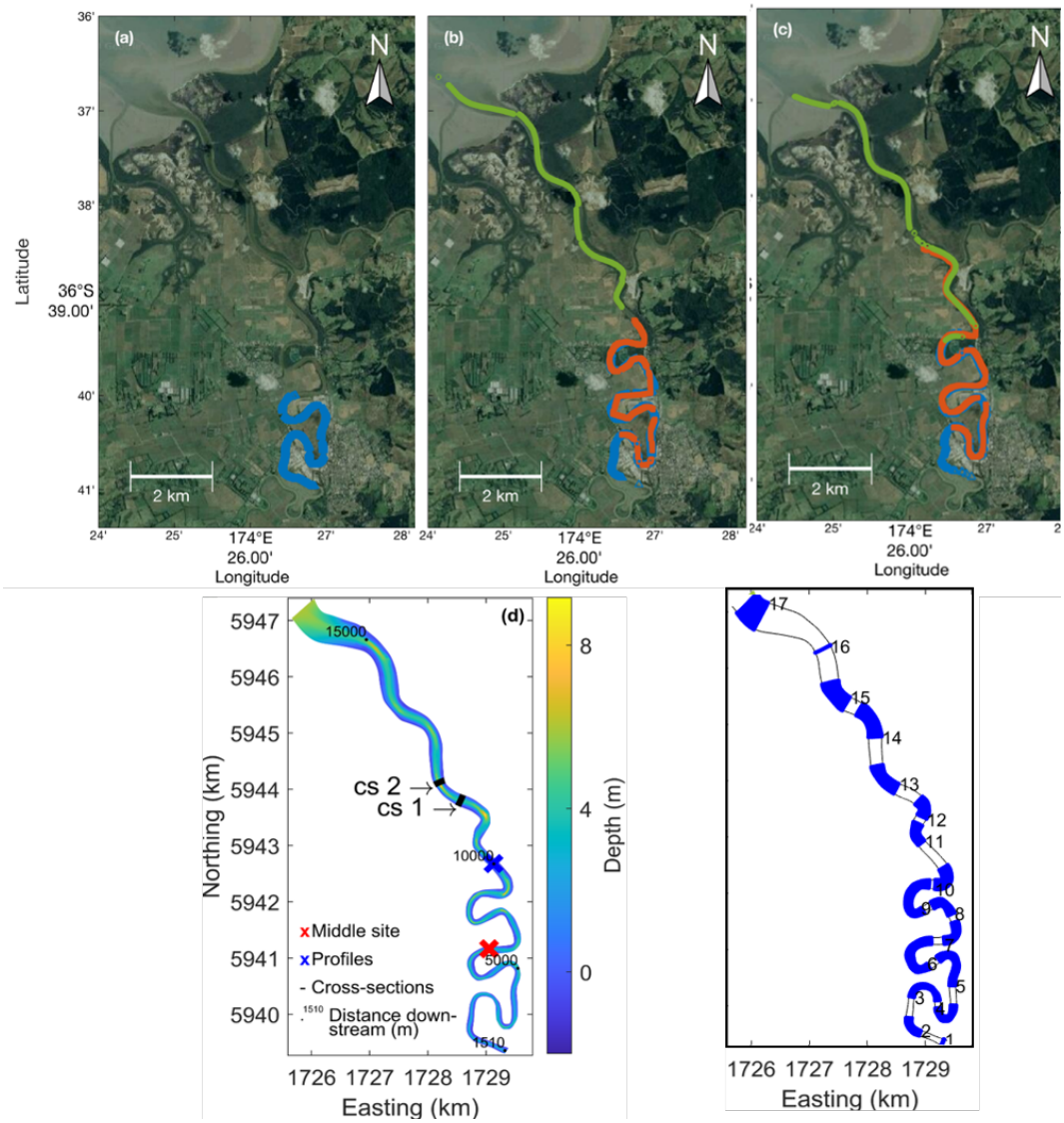

Figure 3.1: (a, b, c) Drifter tracks on October 1st, 2nd and 3rd, respectively. The three colours show drifters released at approximately the same time from three different locations along the Kaipara River in the North Island of New Zealand. (d) Bathymetry of the Delft3D model and locations of the 'middle site' (red cross) and of cross-sections (black lines). (e) River bends (blue shading).

et al., 2001). The model set up has been presented in detail in Dejeans et al. (2022) but is summarized here for completeness. The study grid encompasses about 15 km along the Kaipara River, from an upstream point where a fixed ADCP was located to the river entrance in the estuary, which was extended artificially by about 500 m downstream (Figure 3.1d). Horizontally, the grid comprises 6770 × 50 rectangular grid cells, of size approximately 2.4 × 2.1 m.

Vertically, the model has 20 equal-sized σ-layers, whose thickness, by definition, varies with depth (each cell amounting 5% of the water depth at each time). Open boundaries were used to force the model both upstream and downstream. The upstream boundary was forced by measured observations of current speeds collected by an ADCP during the drifters' deployment, while the downstream open boundary was forced by a time series of water level (data collected from the Pouto Point tide gauge close to the river mouth). The simulation time was 7 days in total, including 4 days of 'spin-up' for the model to reach a state of equilibrium preceding the three days the observations were taken, namely from October 1st to October 3rd 2013. The upstream current speeds observed during the three days of the experiment were replicated to force the model during the spin-up time. The simulation time step was 0.2 min and results were output at every time step. The model was calibrated by comparing Eulerian water levels and depth-averaged velocities observed at a site in the middle of the river length (red cross on Figure 3.1).

We apply both the k-L and k-ϵ closure schemes with Delft3D to compute the vertical eddy viscosity coefficient ν_V and the vertical eddy diffusivity coefficient D_V. The k-L turbulence closure model analytically defines the mixing length L and computes the kinetic energy k using a transport equation. The k-ϵ model uses a transport equation to solve for both k and ϵ (Deltares, 2020).

3.2.3 Model runs and data processing

The present work aims to compare the k-ϵ and the k-L closure schemes, which allow for direct comparison with ϵ computed from the observations. The calibrated model was run twice, changing only one parameter - the turbulence closure scheme, and using the set up described in Section 4.2.2, selecting successively the k-ϵ and the k-L closure schemes. Model results were extracted at each time step from the grid cell corresponding to the location of the drifter (both horizontally and vertically). Then, the same model was run with the only difference in parameterization being the selection of the k-L closure scheme.

Delft3D does not directly output the dissipation of turbulent kinetic energy when run with the k-L closure scheme. In that instance, ϵ was computed using the following equation (Deltares, 2020):

$$\epsilon = c_D \frac{k\sqrt{k}}{L}, \tag{3.1}$$

with

$$L = \frac{\nu}{c'_\mu \sqrt{k}}, \tag{3.2}$$

where

$$c'_\mu = 0.09^{\frac{1}{4}}, \tag{3.3}$$

and where the eddy viscosity ν and the turbulent kinetic energy k are direct outputs of the model.

We chose to quantify the performance of the k-L and k-ϵ by computing some standard errors, including the bias in the mean, the bias in the median, the Mean Absolute Error (MAE) and the Root Mean Absolute Error (RMSE). Those errors where plotted against either binned velocities of $0.1\,\mathrm{m.s^{-1}}$ defined as follows:

$$0.1(i-1) < v_{o_i} \leq 0.1i \tag{3.4}$$

where v_{o_i} are observed velocities belonging to the bin i; or against the maximum sinuosity within bend j. The different velocity error statistics for each bin i or sinuosity bin j are defined here:

$$\mathrm{Bias}_{mean} = \frac{1}{n_i} \sum_i (v_{p_i} - v_{o_i}), \tag{3.5}$$

$$\mathrm{Bias}_{median} = \frac{1}{n_i} (\sum_i (\mathrm{median}(v_{p_i}) - \mathrm{median}(v_{o_i})), \tag{3.6}$$

$$\mathrm{MAE} = \frac{1}{n_i} \sum_i |v_{p_i} - v_{o_i}|, \tag{3.7}$$

$$\mathrm{RMSE}_i = \sqrt{\frac{1}{n_i}\sum_i (v_{p_i} - v_{o_i})^2}, \tag{3.8}$$

where v_{p_i} are predicted velocities belonging to the bin i, and, n_i is the number of values in bin i.

In order to examine the influence of the channel geometry on turbulence, the river was divided into bends and straight sections. This categorization of the channel was done by first calculating a local sinuosity index, SI, at each grid cell along the river domain, which corresponds to the ratio of the along-channel length by the distance of the corresponding straight line between two points, using a moving window corresponding to a fixed along-channel distance of 100 m (a SI of 1 therefore means the section is perfectly straight). More details can be found in a previous paper (Dejeans et al., 2022). A sinuosity threshold of 1.0007 was set as a threshold value to classify the study area into 16 bends and 15 straight sections as shown in Figure 3.1e.

3.3 Results

Model performance of the tidally driven meandering Kaipara River was initially validated by comparing observations of water levels and flow speeds to Eulerian measurements from the middle of the domain (red cross, Figure 3.1) (Dejeans et al., 2022). For all model runs, the performance of the model (for water levels and flow speeds) was classified as 'excellent' (Sutherland et al., 2004), regardless of the turbulence closure scheme applied. While this calibration was limited (in terms of number of sites - owing to most instruments being deployed on drifters), it nonetheless provided confidence that the basic model performance was sufficient to then be assessed under a more stringent Lagrangian validation.

The Lagrangian distribution of along-river horizontal flow speeds was not found to be sensitive to the turbulence closure scheme. An example of the comparison of predictions against observations of horizontal speed is presented

in Figure 3.2. All models reproduce the overall along-river distribution and the right order of magnitude in terms of horizontal flows (noted in Dejeans et al. (2022) for the k-ϵ scheme). Moreover, speeds are slower around the bends and faster along the straight sections of the river, a trend which is well captured by the model (e.g., Figure 3.2, blue stars). However, there are times when observations are not well reproduced by the model, and these discrepancies are larger in the vicinity of the bends (e.g., around 6,500 m on Figure 3.2, blue stars). Generally, results using the k-L scheme follow the same trend as those using the k-ϵ scheme, although the former predicts slightly slower speeds (e.g., Figure 3.2, orange crosses). Furthermore, Figure 3.3 (top) shows the Root Mean Squared Errors (RMSE) of the Lagrangian speeds versus speed (binned into 0.1 $\mathrm{m.s^{-1}}$ intervals). Errors decrease with flow speeds until about 0.54 $\mathrm{m.s^{-1}}$ and then subsequently increase with faster speeds (Figure 3.3, top).

Similarly, the turbulent closure scheme appears to only have a relatively small effect on predictions of turbulent energy dissipation. Figure 3.4 provides an example of the upstream distribution of ϵ from a single day (black dots) and the corresponding k-L and k-ϵ model predictions (blue stars and orange crosses). Both schemes show that the model is capable of reproducing the same order of magnitude and some of the main structures as the observations; however, neither model accurately reproduce patterns of variability on the smaller scale, especially around the bends (e.g., Figure 3.4, blue squares). The distribution of the dissipation rates of k generated by the k-L model follows the same structure as the k-ϵ model while predicting $\log_{10}\epsilon$ up to 1.2 $\mathrm{m^2}.s^{-3}$ larger and, on average, 0.07 $\mathrm{m^2}.s^{-3}$ larger (e.g., Figure 3.4, blue stars). Similarly to the work done with speeds, the errors in predictions of ϵ are computed in the Lagrangian framework as:

$$RMSE_i = \sqrt{\frac{1}{n_i}\sum_i (\log_{10}\epsilon_{p_i} - \log_{10}\epsilon_{o_i})^2} \tag{3.9}$$

where ϵ_p and ϵ_o are the predicted and observed dissipation of turbulent kinetic

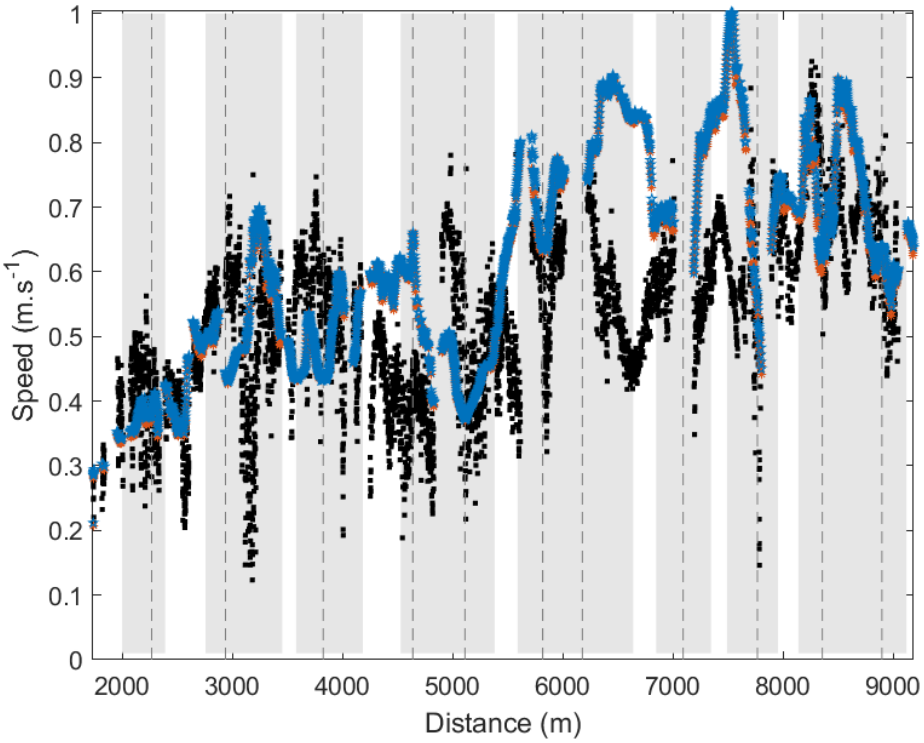

Figure 3.2: Example of horizontal flow speeds observed by the drifter released upstream on day 3 (black dots) and the corresponding model predictions using the k-L (blue stars) and the k-ϵ (orange crosses) models. Note: The shaded grey rectangles and dashed lines represent the location of the bends and the bend apexes, respectively.

energy, respectively (so $\log_{10}\epsilon_p$-$\log_{10}\epsilon_o$=1 corresponds to an order of magnitude difference). Figure 3.3 (bottom) shows that, although the distribution of the RMSE of $\log_{10}\epsilon$ with regard to the binned speeds of the two turbulence closure models k-L and k-ϵ displays the same trend as the distribution of the RMSE of speeds (Figure 3.3, top), the errors in $\log_{10}\epsilon$ tend to increase more in the k-L model than the k-ϵ model.

Classifying the sections of the river as bends and straights (see methods below) highlights the discrepancies in predictions. Figure 3.5 gives the bias in the mean, bias in the median, Mean Absolute Error (MAE) and Root Mean Squared Error (RMSE) of the Lagrangian flow speed and ϵ between the observations and both models' predictions within the bends against the maximum sinuosity of each bend. All four errors show that sharper bends globally cor-

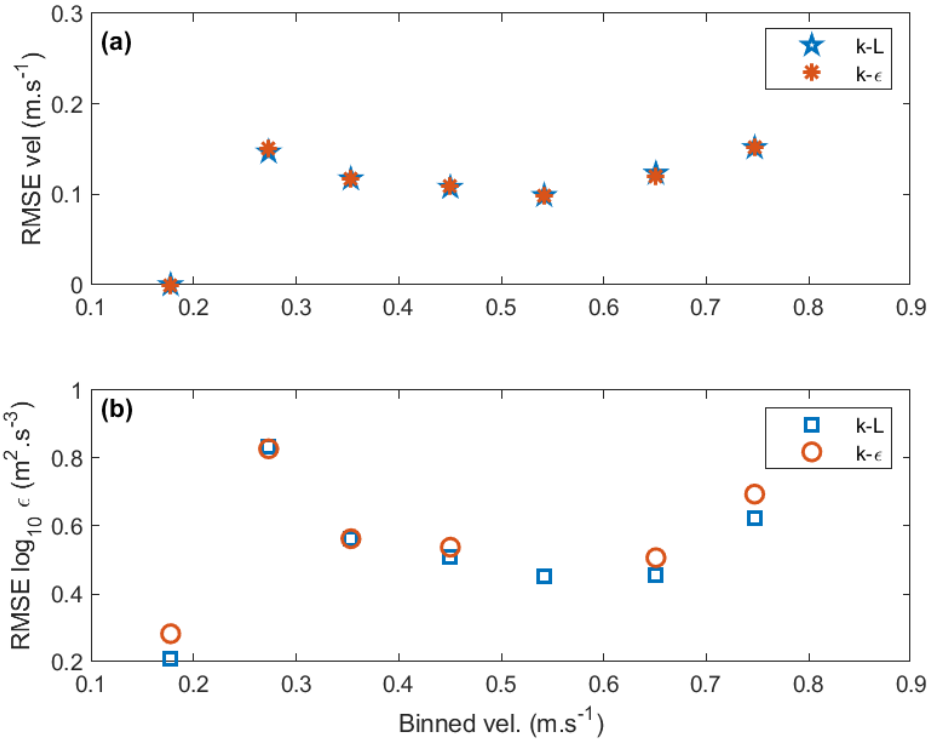

Figure 3.3: Lagrangian RMSE of (a) along-channel speeds (crosses and stars) and (b) ϵ (circles and squares) between observations and model predictions obtained with the k-L (orange markers) and the k-ϵ (blue markers) closure schemes with regards to the observed Lagrangian speeds binned over 0.1 m.s^{-1} over the time of the experiments.

respond to larger errors in predictions of both speed and ϵ (Figure 3.5). In terms of flow speed, and as noted previously, both the k-L and the k-ϵ models behave similarly, regardless of the indicator. In terms of $log_{10}\epsilon$, the bias in the mean and bias in the median both show that the k-ϵ model (Figure 3.5, orange crosses) tends to underpredict the observations inside the bends more than the k-L model (Figure 3.5, blue stars). The MAE and the RMSE, however, show that, within the bends, the errors in $\log_{10}\epsilon$ are slightly larger when predicted by the k-ϵ model (Figure 3.5, orange circles) than by the k-L model (Figure 3.5, blue squares).

We also compare the cross-sectional distribution of the computed quantities between models (noting that there were no cross-sectional observations). Generally, both turbulence closures behave similarly in terms of predictions of

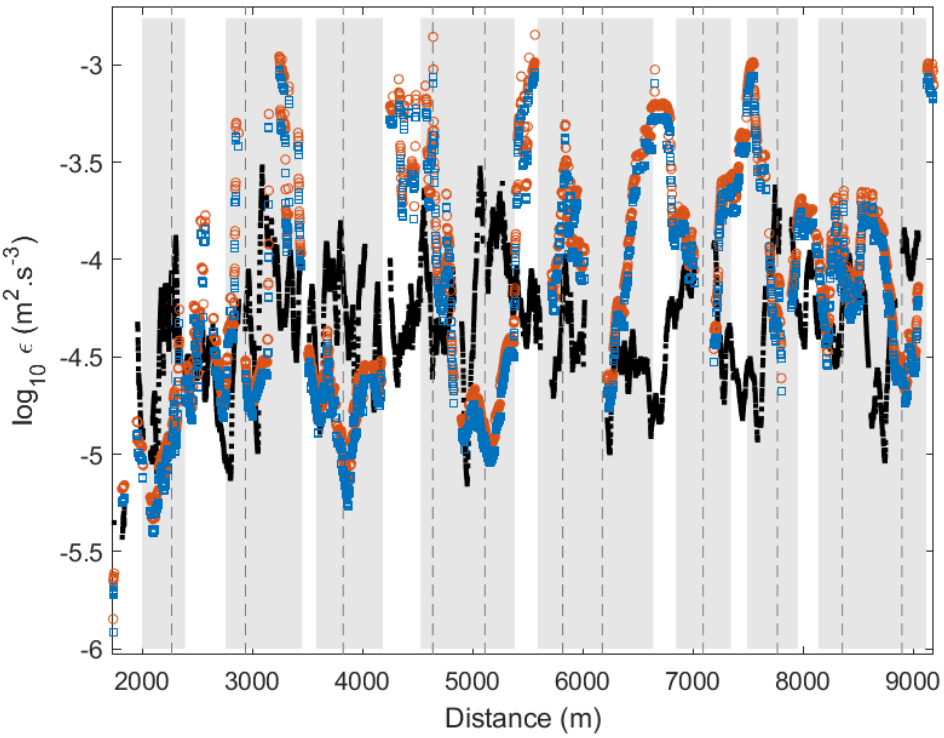

Figure 3.4: Example of turbulent energy dissipation observed by the drifter released upstream on day 3 (black dots) and the corresponding model predictions according to the k-L (blue stars) and the k-ϵ (orange crosses) models. Note: The shaded grey rectangles and dashed lines represent the location of the bends and the bend apexes, respectively.

horizontal flow speeds, with values reaching a maximum at the surface where the water depth is the largest, decreasing either side of the thalweg (up to 0.4 m.s^{-1} less than the maximum value on the edges of the grid) and declining up to about 0.2 m.s^{-1} with increasing depth (e.g., Figure 3.6a and b). In terms of the lateral distribution of ϵ, the two closure schemes give overall similar results. However, the k-L model fails to predict values for ϵ in the first 20 cm below the sea surface. Otherwise, both closure schemes show that the dissipation of TKE tends to be lowest at the sea surface and increase by about 4 orders of magnitude with depth. The example of the sharpest point of one of the bends is given in Figure 3.6c and d.

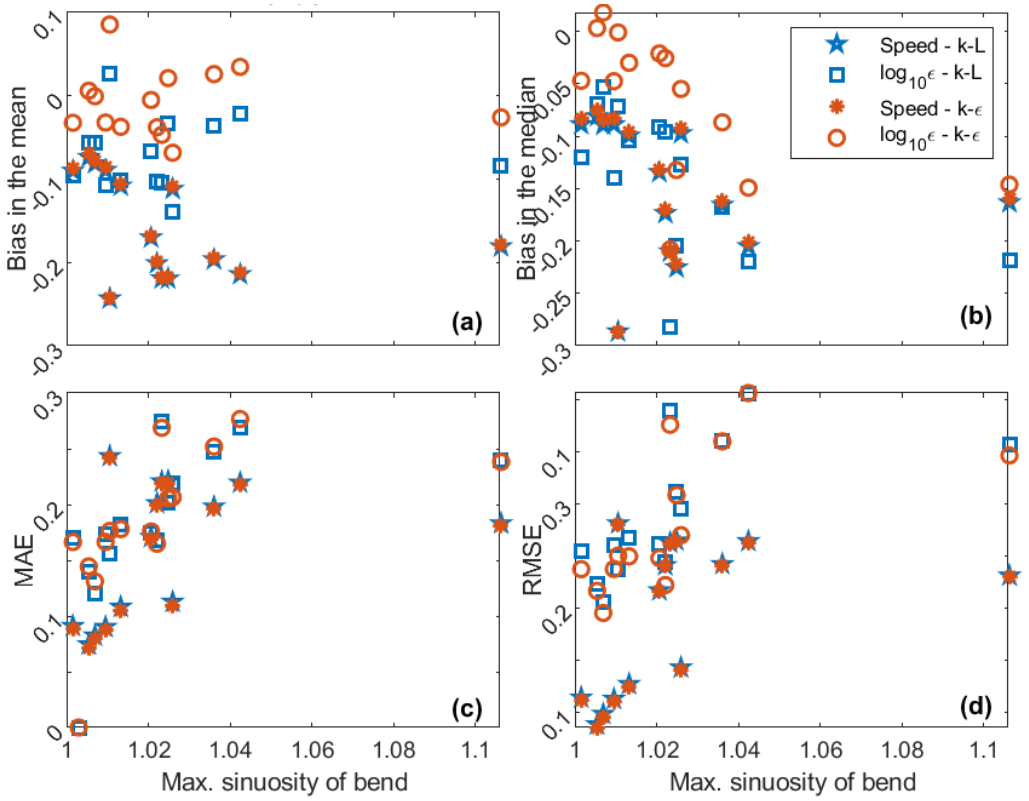

Figure 3.5: Bias (a) in the mean, (b) in the median, (c) MAE and (d) RMSE of the Lagrangian speed (crosses and stars) and energy dissipation (circles and squares) between the observations and the predictions of both the k-L (orange markers) and the k-ϵ (blue markers) closure schemes against the maximum sinuosity of each of the river bends as defined in Figure 3.1.

3.4 Discussion

There were negligible differences between predictions of speed of the model by the different turbulence closure schemes (Figures 3.2, 3.3). The Lagrangian comparisons of the model results with the observations showed that the k-L and k-ϵ closure schemes both reproduce the right order of magnitude of speeds but fail to reproduce the variability over small scales (i.e., over a couple of hundreds meters, see e.g., Figure 3.2). The results presented here also show that larger errors in speed between the model and the observations are generally located within the bends and, more precisely, tend to increase with the sinuosity of the river, regardless of the closure scheme. Indeed, although a previous study (Dejeans et al., 2022) only showed a qualitative relationship between

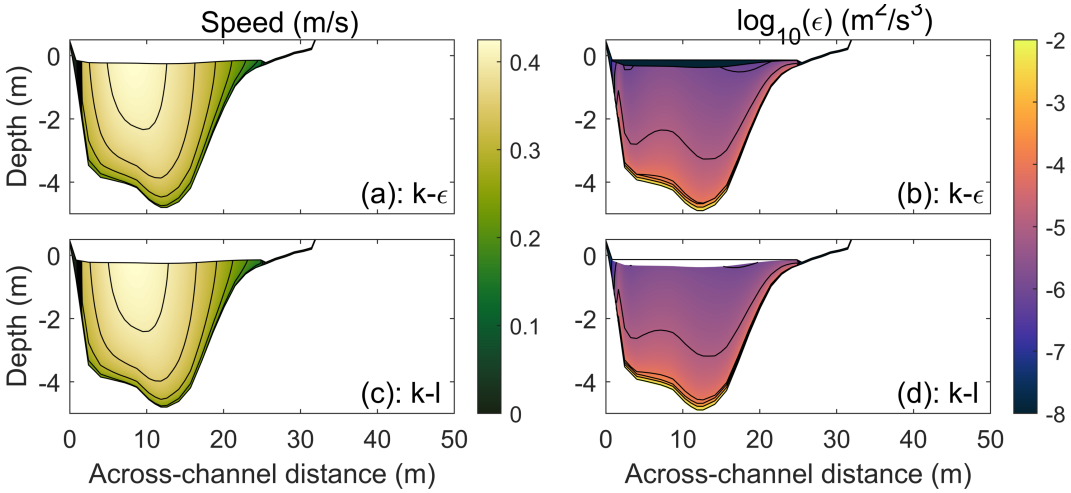

Figure 3.6: Cross-sectional distribution of (a and c) along-channel speed and (b and d) energy dissipation of turbulent kinetic energy within the sharpest point of the eighth bend (see Figure 3.1e) computed using the (a and b) k-ϵ and the (c and d) k-L closure schemes at the beginning of the deployment on the third day. Contours represent (a and c) 0.05 $\mathrm{m.s^{-1}}$ and (b and d) -1 $\mathrm{m^2.s^{-3}}$. We note that the very dark colour in b corresponds to $\log_{10}\epsilon \approx O(10^{-14})$.

the sinuosity of the river and the errors in the models, Figure 3.5 (bottom left and right) illustrates that classifying the river into straight portions and bends reveals a positive trend between model errors and sinuosity of the bends, suggesting that the errors are mainly located within the meandering parts of the channel and that the more acute bends correspond to the larger errors. This positive trend is not affected by the closure scheme (orange crosses and blue stars on Figure 3.5). The difference of model performance depending on the geometry of the sections is in agreement with Eulerian comparisons in previous works, e.g. Wilson et al. (2002), who found that flow parameters were easier to reproduce in straight sections than in meanders. Another investigation also compared different closure schemes in a model channel with varying sinuosity and found that, in an Eulerian frame of reference, another two-equation closure scheme, namely k-ω, predicted Eulerian flow characteristics (and especially flow separation) more accurately than the k-ϵ closure scheme, which, although most commonly used, is not always the more accurate turbulence closure scheme (Kim et al., 2020).

Similarly, when considering the distribution of dissipation rate of TKE predicted along-river, the general pattern and order of magnitude are reproduced by both closure schemes; however, the smaller structures (on scales of about a couple of hundred meters) of the observed ϵ are not well predicted by either closure scheme (e.g., around 5,000 m on Figure 3.4). The difficulty of reproducing turbulent energy dissipation across different closure schemes has been reported in the past for Eulerian comparisons and has predominantly been attributed to the flow separation that cannot be well predicted by models such as k-ϵ (Kim et al., 2020). As with flow speeds, classifying the river into straight sections and bends reveals a positive correlation between the errors in ϵ and the sinuosity (Figure 3.5, bottom left and right, orange circles and blue squares), which is also likely due to the difficulty of the model to predict flow separation. Although cross-sectional model predictions cannot be compared to observations in the present case, the predictions of the vertical distribution of flow speed and ϵ within the water column derived from both closure schemes suggest that neither closure schemes accurately predict the flow in sharper areas of the river as neither show the presence of flow separation.

Similarity in results of ϵ predicted by different closure schemes has also been observed in the past in a variety of environments (e.g., Burchard and Petersen, 1999; Wijesekera et al., 2003; Kim et al., 2020). For instance, two previous studies gathered observations of stratified and mixed flows from both laboratory and field experiments and compared these to numerical model results from two turbulence models, namely k-ϵ and Mellor-Yamada, and found minimal differences between schemes (Burchard et al., 1998; Burchard and Petersen, 1999). Another work compared four turbulent models, k-ϵ, k-ω, k-kl and a novel two-equation turbulence closure for four test cases in a rectangular channel (Warner et al., 2005). Regardless of the scenario, all schemes demonstrated similar and reasonable abilities in reproducing the experimental data.

Nevertheless, despite similarity in patterns or values of parameters, there

were some subtle differences in the predicted dissipation rates of TKE. Values from the k-L closure scheme are consistently slightly higher by an average of $0.07\,\mathrm{m}^2.s^{-3}$ than with the k-ϵ scheme (e.g., Figure 3.4), which is in agreement with results from past studies. An example is a study that found that one of the closure schemes, the Mellor-Yamada, tended to underestimate mixing and bottom stresses compared to the other three investigated closures (Warner et al., 2005). Model performance varied with location, e.g. k-L performs better around 3,600-4,000 m (Figure 3.4) whereas k-ϵ performs better around 7,200-7,800 m (Figure 3.4). Although the Mean Absolute Errors (MAE) are similar for the two turbulent closure schemes (Figure 3.5, bottom left, orange circles and blue squares), the Root Mean Squared Errors are generally slightly higher for the k-ϵ closure (Figure 3.5, bottom right, blue squares). Thus, the slightly better overall performance of the k-L closure model agrees with and extends the work by de Almeida and Ota (2020) which used a 2D model they compared to experimental results of an experimental channel. Indeed, they showed that simpler turbulence models could give results as good or even better than more sophisticated models. Furthermore, our results also align with the work of Broomans (2003), who also compared results from the k-L and the k-ϵ models implemented in Delft3D, and developed test cases in which the model errors are globally higher when using the k-ϵ rather than the k-L turbulence model.

3.5 Conclusion

This paper focuses on Delft3D model predictions of speed and turbulence and compares results from the k-L and k-ϵ closure schemes. The comparison is based on a unique and large Lagrangian dataset collected in the meandering Kaipara river, NZ, allowing observations over different scales. Predictions of flow speeds computed by both turbulent models are very similar to one another which, as found in previous works, are relatively close to observations. In terms of dissipation of turbulent kinetic energy, the k-L closure scheme gener-

ally performs slightly better than k-ϵ although the differences between the two predictions are consistently small. The differences between model predictions, of both speed and ϵ, and observations tend to, overall, increase around the bends. Our results therefore extend previous works, mainly based on Eulerian observations, on laboratory experiments and over smaller scales, by confirming the geometry of the river plays an important role in model performance and showing that k-L performs moderately better than k-ϵ in reproducing turbulence in a relatively large-scale Lagrangian framework. This result suggests that, although a lot of modelling studies use the 'default' closure scheme, which is often the most sophisticated of the turbulence models implemented in the software package in use (e.g., k-ϵ for Delft3D-FLOW), other simpler models might perform better, therefore saving computation time and capacity.

Chapter 4

Controls on the flow-following distribution of suspended sediment concentrations in a tidally driven river

Contribution of authors

Chapter 4 duplicates a paper of the title "Controls on the flow-following distribution of suspended sediment concentrations in a tidally driven river", by Bérengère S. Dejeans, Julia C. Mullarney, Iain T. MacDonald and Glen M. Reeve, which will be submitted to *Journal of Geophysical Research - Earth Surface* in 2023. The Delft3D numerical model was developed by myself, Bérengère Dejeans, with the input from Glen Reeve. Field data was provided by Iain MacDonald and Julia Mullarney. I wrote Matlab scripts to process and analyse model outputs and the field observations. My co-authors, Julia Mullarney and Iain MacDonald provided suggestions on data analysis, interpretation of results, and also provided feedback on the the writing of this chapter.

Abstract

Sediment transport shapes riverine and coastal environments, across multiple spatial and temporal scales. Here, we use a numerical model and field observations to explore the underlying processes influencing the movement and deposition of fine muddy particles in a tidal river. In particular, we focus on flow-following Lagrangian measurements of suspended sediment concentrations (SSC) in the fluvial-to-marine transition zone of the Kaipara River, New Zealand. A systematic exploration of simulations with different processes implemented revealed that the sediment in suspension mainly resulted from erosion from the bed, with advection from upstream playing a smaller role. Despite multiple simplifications, the model was able to reproduce the magnitudes and trends of concentrations along the river in the Lagrangian frame-of-reference, which constituted a particularly stringent test of model performance. Mid-scale (O(km)) variability in the model predictions of SSC was relatively consistent between tides, and was found to be driven by rapid changes in shear velocity associated with the transition of flow between bends and straight sections. The sudden local increases or decreases in SSC occurred over distances of $\sim$100 m in the straight sections and bends, respectively. However, the model underpredicted the magnitude of these changes, and differences to observations were attributed to the lack of additional freshwater inputs and wind forcing in the model. Surprisingly, since flocculation was not included in our model, predictions of SSC were generally underestimated at times when larger flocs were present in the field data. However, the calculated shear velocities suggested that, at those times, either vertical mixing was sufficient to reduce floc settling or additional resuspension from the bed occurred.

4.1 Introduction

Sediment transport within the fluvial-to-marine transition zone is controlled by a myriad of complex physical and biogeochemical processes. The movement and deposition of sediment shape riverine and coastal geomorphology, and also influence rates of carbon burial, the health of benthic ecosystems, water quality, and navigability (e.g., Hedges and Keil, 1995; Harrison et al., 2007; Roy and Sinha, 2014). Sediment input to, and the dynamics of, these regions are strongly affected by human activities (e.g., dredging, damming, flood protection measures) (Walling, 2006), and these systems can be particularly vulnerable to effects of climate change such as sea level rise, and changes in storminess or precipitation. Thus, understanding the underlying sedimentary mechanisms and the interaction processes between them is crucial for any coastal management project or for setting our ability to predict changes under future forcing regimes (e.g., Grady et al., 2013; Van Manh et al., 2015).

Numerical modelling of sediment transport relies on being able to accurately predict the balance between erosion, accretion, and the advection and dispersion of particles (owing to turbulence and settling) within the water column (James et al., 2010). Numerical model formulations can vary widely depending on the model purpose and the nature and complexity of the problem (e.g., chemical versus physical transport, bedload versus suspended load) (e.g., Papanicolaou et al., 2008). For river engineering or environmental management purposes, model approaches are often constrained by computational resources (including time for simulations) and data availability.

Three-dimensional process-based models in meandering channel flows have been predominantly validated through comparisons to laboratory data. In their study, Wu et al. (2000) compared predicted flows and sediment transport under equilibrium flow conditions to measurements taken from a laboratory channel with 180° bend by Odgaard and Bergs (1988). The simulations used the k-ϵ turbulence closure scheme and solved for both the suspended- and

the bed-load (the interaction between suspended- and bed-load is taken into account by the net deposition/entrainment flux of sediment at the top of bed-load layer). When compared to cross-stream profiles of velocities and bed profiles at different points around a 180° bend, the work demonstrated that the model was able to reproduce both flow and sediment transport, and bed level. However, as the laboratory transport was dominated by bed-load, testing of the suspended-load could not be examined in detail. Lai and Wu (2019) proposed a new 3D hydrostatic numerical flow and sediment transport model on unstructured flexible meshes. They tested their predictions of flow and sediment transport variables in a channel characterised by a sharp 180° bend by comparing to observations by Fuhrman et al. (2010) in a laboratory flume. Two simulations with different sediment sizes (0.0236 mm and 0.079 mm), and Rouse parameters (0.06 and 0.672, respectively) were undertaken. They found that the prediction of vertical profiles of sediment concentration corresponded well to the shape of the theoretical Rouse profile. While validations of sediment transport models to laboratory observations offer promise, the applicability of these sediment transport models across the wide range of forcing conditions of real environmental systems is still incomplete.

Turbulence within the water column influences the aggregation and break up of clusters of fine cohesive particles (flocs), the size and composition of which causes variations in settling velocity. For practical applications, models tend to rely on commonly implemented turbulence closure schemes. However, predictions of sediment transport have been found to be sensitive to the selection of turbulence closure scheme in multiple cases (e.g. Puleo et al., 2004; Warner et al., 2005; Amoudry and Souza, 2010, 2011). For example, Puleo et al. (2004) use laboratory data to assess the performance of one-dimensional wave bottom boundary layer models and found that the bed shear stress, and consequently sediment transport, was strongly dependent on the closure scheme. More precisely, they compared six different models (laminar, linear, parabolic, k-L one-equation turbulence closure, k-ϵ two-equation turbulence

closure, and k-ω two-equation turbulence closure) which differ in their estimation of the turbulent eddy viscosity, over smooth and rough beds. Overall, they found that the simpler models, which prescribe the shape of the eddy viscosity vertical profile (laminar, linear and parabolic) gave similar results to the one- and two-equation turbulence closure models in reproducing the general velocity profiles. They even observed that using a linear profile of eddy viscosity was not only less computationally intensive but also led to better results in terms of velocity profiles than the more sophisticated k-ω turbulence closure model. Nevertheless, in order to predict the turbulent kinetic energy, the bed shear stress and sediment transport, the more sophisticated k-ω turbulence closure model was found to be the most accurate. Similarly, Warner et al. (2005) also showed that the SSC was contingent on the selection of the turbulence closure scheme. They developed three test cases in ROMS (Regional Oceanographic Modeling System) to compare three two-equation turbulence closures (k-kl, k-ϵ and k-ω), modelling (a) a steady barotropic flow in a rectangular channel, (b) a stratified fluid with the presence of wind and (c) a flow in a rectangular channel subjected to a stratified pressure gradient. Their results demonstrated that larger relative differences appeared in SSC compared to salinity, showing that suspended sediment transport intensified the differences inherent to the closure schemes, because (a) sediments at low to moderate concentrations do not influence mixing, hence a lack of correlation between sediment and sediment diffusivity, (b) the deposition/resuspension of sediment depends on the bottom stress, governed by the closure scheme and (c) the balance between turbulent diffusive mixing and gravitational sinking drives the resuspension of sediment (i.e., if an area is well mixed in terms of salinity and temperature, the suspended sediment will be sensitive to small variations in diffusive mixing, unlike the salinity and temperature).

Past studies have shown that, in general, two-equation turbulence closure schemes yield more accurate predictions of sediment transport than one-equation turbulence closure schemes. Amoudry and Souza (2010) used the

three-dimensional POLCOMS (Proudman Oceanographic Laboratory Coastal Ocean Modeling System) coupled with GOTM (General Ocean Turbulence Model) to study the effects of turbulence closure schemes on sediment transport and on the morphological evolution of an idealized rectangular estuary. When a one-equation closure scheme was implemented, the model failed to reproduce realistic results, and could not predict the estuary turbidity maximum or accurately reproduce the isohalines. They also showed that two-equation closure schemes produced different results to one another in terms of sediment transport including bed level changes but could not conclude which turbulence closure scheme performed better due to a lack of data. In a further study (Amoudry and Souza, 2011), model results were compared with observations of velocity profiles, SSC and trench migration from a laboratory flume and only slight differences were found in predicted velocity profiles between the turbulence closure schemes, but the differences in bed shear stresses were significant. Along with the sediment-induced stratification and the erosion parameterization, they showed that the closure schemes had a large effect on the SSC and on the bed evolution, which were mainly due to differences in computing the turbulent length scale L.

In the present work, we further explore the dependence of model predictions of sediment transport on turbulence closure scheme in a tidal river, the heavily sediment-laden Kaipara River in New Zealand. By comparing with Lagrangian observations, we explore the balance of advection and erosion and deposition processes at a high spatial resolution along a $\sim$15-km stretch of river. The unique Lagrangian dataset offers an excellent opportunity to explore transport processes without the need to consider the effects of a time lag in adjusting to upstream (antecedent) conditions. The model builds on a Delft3D model developed in a previous study, Dejeans et al. (2022), which was used to demonstrate that the Lagrangian approach offered a more stringent validation of hydrodynamics compared to the classical Eulerian validation. Deficiencies in model performance were revealed, in particular in predictions of

dissipation rates of turbulence kinetic energy around bends. Additional work, Dejeans, Mullarney, and MacDonald (Dejeans et al.), also showed that while model performance was not overly sensitive to the choice of either the k-ϵ of the k-L closure scheme, overall, the simpler one-equation k-L scheme was found to perform slightly better in predictions of speed and turbulence than the more sophisticated and more widely used k-ϵ scheme, hence saving computation time. The current chapter tests whether such a conclusion remains valid when including sediment transport.

4.2 Methodology

4.2.1 Study site and data collection

The present model was developed based on field observations in the tidally driven Kaipara River, located in the Southern part of the Kaipara Harbour, a 94,700-ha drowned-valley system in the North Island of New Zealand (MacDonald and Mullarney, 2015). Within the 15-km stretch of the river studied in this work, the maximum and average depths along the thalweg are 9.2 m and 4.5 m below MSL, respectively; the width of the river ranges from 50 to 200 m. The river is characterised by meandering bends of different sizes and directions. According to calibrated optical backscatter measurements, the SSC at $\sim$1.5 m below the water surface increases downstream, with values ranging from 100 to 850 mg.L^{-1} (MacDonald and Mullarney, 2015).

Lagrangian observations were collected by releasing three FlocDrifters, flow-following drifters mounted with a GPS, FlocCam, a pulse-coherent 2-MHz Nortek Aquadopp Acoustic Doppler Current Profiler (ADCP), a Nortek Vector Acoustic Doppler Velocimeter (ADV), an optical backscatter sensor (OBS) and a Sea-Bird Electronics SBE-37 MicroCAT Conductivity-Temperature-Depth (CTD) sensor measuring location, in-situ images of flocs, a short profile of 3D velocity components (at 8 Hz) and single-point velocities (with a sampling rate of 16 Hz), optical backscatter and the conductivity and temperature (sampling

rate of 0.167 Hz), respectively. The dissipation rates of turbulent kinetic energy, ϵ, were computed from the short profiles of velocities in beam coordinates and using the structure function of Wiles et al. (2006) over windows of 64 s (MacDonald and Mullarney, 2015). The voltage output by the OBS (V) was related to the SSC by a linear relationship:

$$SSC = GV + O, \tag{4.1}$$

where G is the sensor gain (unit of $\mathrm{g.L^{-1}.V^{-1}}$) and O is the sensor offset (unit of $\mathrm{g.L^{-1}}$). Each sensor gain and offset was determined by calibrating the sensor against a series of test suspensions of a known concentration in the laboratory. The sediment used in the calibration came from a ∼100-L water sample collected at the field site. The sediment in the 100-L sample was allowed to settle and the supernatant was removed to form concentrated slurry of fine sediment; this slurry of concentrated fine sediment was subsequently used in the calibration process. A linear regression was used to fit the linear relationship to the calibration dataset (sensor ouptut versus reference suspended solids concentration) to determine the sensor's gain and offset. SSC estimates derived from the laboratory calibration showed only small differences (usually less than 10 %) to the gravimetric analysis of 51 water samples collected during the field experiment, validating the laboratory estimates of SSC, which are used herein.

One drifter was released on October 1st and three drifters were released on both October 2nd and 3rd from three different locations, at the beginning of an ebb tide and drifted downstream for about four hours. The release locations and drifter tracks are shown in Figure 4.1. Additionally, two fixed-location Acoustic Doppler Current Profilers (ADCPs) were deployed during the field campaign, located upstream and further downstream the river domain (Figure 4.2) and the data were averaged over 10 minutes.

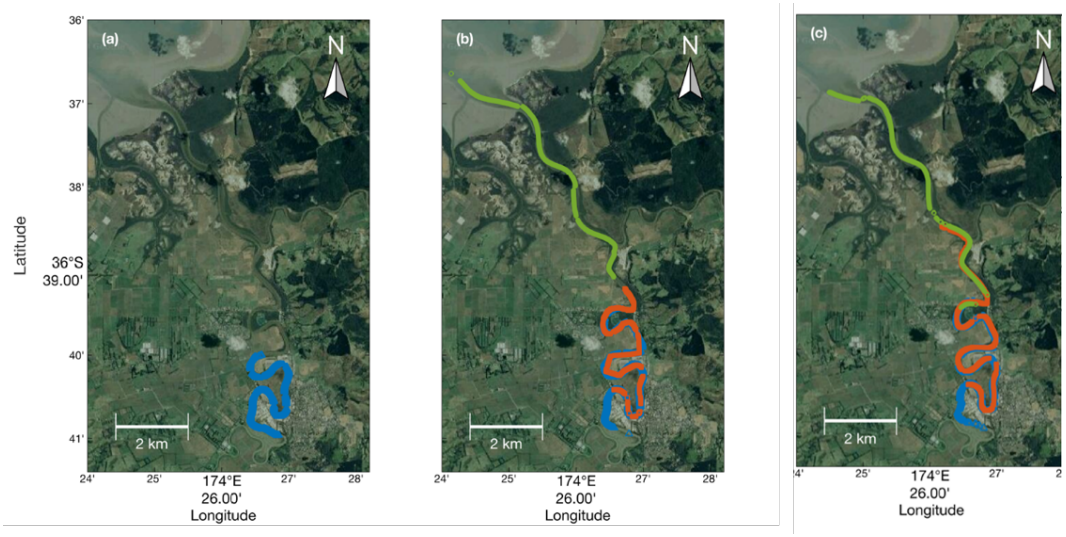

Figure 4.1: Drifter tracks on October (a) 1st, (b) 2nd and (c) 3rd. Each of the three colours correspond to a different drifter released around the same time from a different location along the Kaipara River, New Zealand. For the central drifter on October 2nd (orange, b), the locations are estimates (within $\leq$ 10 m of chase-boat locations) because of a malfunctioning GPS after 112 minutes on that day.

4.2.2 Model set up and simulations

A model of the Kaipara River was developed with the Delft3D-FLOW software package, which enables the simulation of hydrodynamic flows in coastal, estuarine and riverine environments and the inclusion of sediment transport. Delft3D is an integrated modelling system, resolved through the finite-difference scheme, which solves the RANS equations for an incompressible fluid through the application of the shallow water and Boussinesq assumptions (Deltares, 2020). Extensive validation of Delft3D used in coastal and estuarine waters has been undertaken across multiple environments (e.g. Roelvink and Van Banning, 1995; Elias et al., 2001).

The model grid encompasses about 15 km of the Kaipara river, from the location where the fixed upstream ADCP was deployed, which was artificially extended by about 20 m upstream, to the river mouth, which was artificially elongated by about 500 m into the estuary basin (Figure 4.2). The artificial extension of the model boundaries was implemented to provide an opportunity to

remove intertidal areas from the model boundaries, which greatly reduces the potential for numerical instability that can arise when boundaries are subject to wetting and drying. The Coriolis parameter was defined for a latitude of 37°S. In the horizontal direction, the grid is composed of 6770 along-river and 50 across-river rectangular grid cells whose size approximates 2.4×2.1 m. In the vertical direction, the water column was represented by 20-equally spaced (sigma) layers with each layer representing $\sim$5 % of the water depth (Deltares, 2020). The bathymetry was constructed by combining LIDAR data from the Auckland Regional Council and two single-beam echosounder surveys conducted in 2013 and 2017. At the upstream boundary, the model was forced by the currents speeds measured by the upstream fixed ADCP (see Section 4.2.1). The downstream boundary was forced by a time series of water levels collected by the Pouto Point tide gauge near the estuary mouth, which was corrected for tidal propagation with a phase offset.

At the boundary, salinity and temperatures were both set to be time-varying but uniform vertically for the full time series. Both background horizontal eddy viscosity and diffusivity were defined as $1\,\mathrm{m}^2.s^{-1}$ and the background vertical eddy viscosity and diffusivity were kept as zero (default values). All runs had a uniform Chézy roughness of $50\,\mathrm{m}^{1/2}.\mathrm{s}^{-1}$ and uniform background eddy viscosity and diffusivity both equal to $1\,\mathrm{m}^2.\mathrm{s}^{-1}$. The fresh and the saline settling velocities were both equal to $0.25\,\mathrm{mm.s}^{-1}$. The critical bed shear stress for sedimentation and the critical bed shear stress for erosion were set to the default values, i.e., $1000\,\mathrm{N.m}^{-2}$ and $0.5\,\mathrm{N.m}^{-2}$, respectively. The erosion parameter was $0.0001\,\mathrm{kg.m}^{-2}.\mathrm{s}^{-1}$.

The model was run for 23 days, in total, including the 3 days of the experiment (i.e., October 1-3) and 20 days of 'spin-up' time, at a time step of 0.04 min, in which the 3-day time series of water levels were repeated to create a quasi-periodic boundary conditions (noting tidal conditions were matched to ensure the time series had no discontinuities in water level). Each simulation took approximately 25 days to run on 64 cores on the New Zealand eScience

Infrastructure (NeSI) supercomputer.

Three scenarios were simulated, which differed in terms of sediment processes to allow for exploration of the roles of advection of sediment from upstream and the balance between deposition and erosion of the bed sediments. Given the limited time series data of SSC (no profile data was available) with which to force the model, this work uses idealised sedimentary boundary conditions (whilst staying within a realistic parameter space) in order to investigate the balance of the different processes which set the overarching pattern and magnitude of SSC along the river. Each case was simulated twice - to implement both the k-ϵ (runs 1-3) and the k-L (runs 4-6) closure schemes, resulting in a total of six runs. The first and the fourth cases comprised a mobile bed composed of muddy sediment but no sediment input from upstream; the second and fifth cases had a fixed no-slip bottom boundary with a constant upstream sediment input of $0.1\,\mathrm{kg.m^{-3}}$, while the third and the sixth cases implemented both a mobile bed and the constant upstream sediment input of $0.1\,\mathrm{kg.m^{-3}}$ (Table 4.1). A value of $0.1\,\mathrm{kg.m^{-3}}$ was used based on single point observations close to the upper boundary and initial values from the drifter measurements (MacDonald and Mullarney, 2015).

Table 4.1: Summary of numerical simulations.

Case	Turbulence closure scheme	Initial sediment thickness (m)	Upstream sediment input ($\mathrm{kg.m^{-3}}$)
Case 1	k-ϵ	10	0
Case 2	k-ϵ	0	0.1
Case 3	k-ϵ	10	0.1
Case 4	k-L	10	0
Case 5	k-L	0	0.1
Case 6	k-L	10	0.1

4.2.3 Data processing

At each time step, the predicted quantities of interest were extracted from the grid cell matching the observed location of the drifter (as provided by the GPS) at that time (both horizontally and vertically). The extracted values

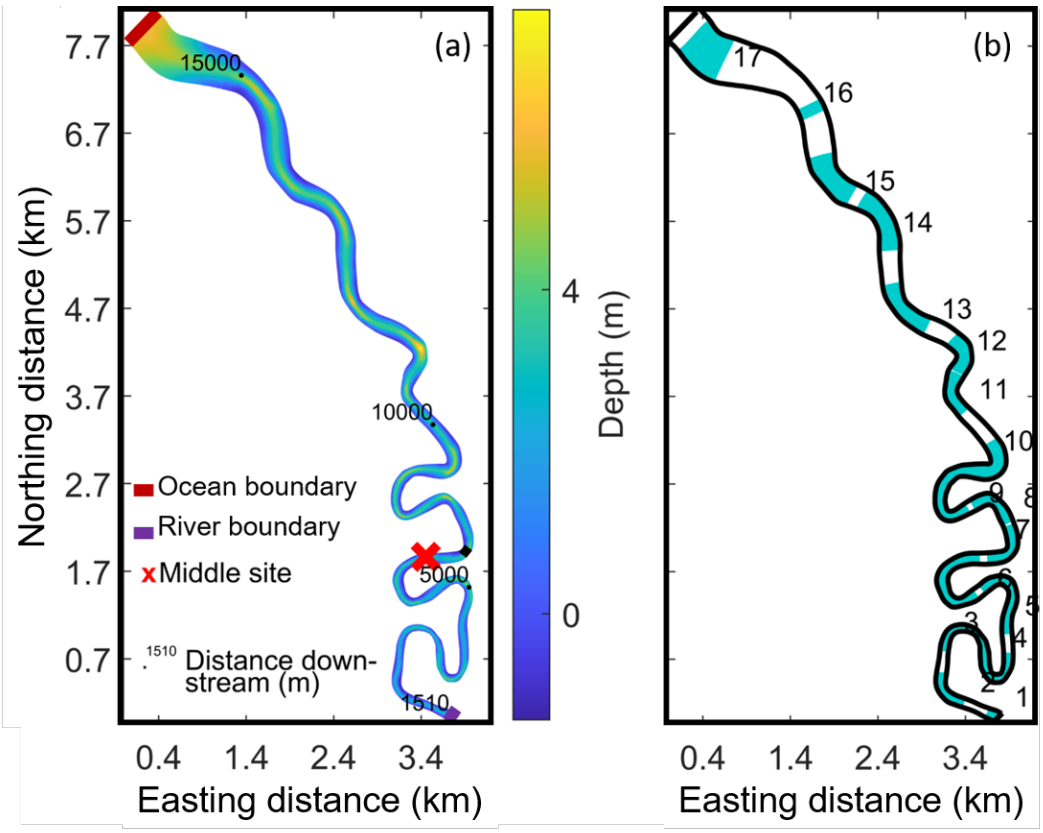

Figure 4.2: (a) Bathymetry and location of the fixed ADCP ('middle site', red cross) and (b) location of the river bends (blue shading). The river (upstream, purple) and ocean (downstream, dark red) boundaries are outlined on (a).

are therefore 'quasi' Lagrangian, so any errors in velocity do not lead to compounded errors in location and other quantities as the drifter moves along the river. When the model was implemented using the k-L turbulence closure scheme, the dissipation rate of turbulent kinetic energy, ϵ, was not directly provided as an output variable in the Delft3D software, so was calculated from the eddy viscosity ν and the turbulent kinetic energy k as follows (Deltares, 2020):

$$\epsilon = c_D \frac{k\sqrt{k}}{L}, \tag{4.2}$$

with

$$c_D \approx 0.1925, \tag{4.3}$$

and

$$L = \frac{\nu}{c'_\mu \sqrt{k}}, \tag{4.4}$$

where

$$c'_{\mu} = 0.09^{\frac{1}{4}}. \tag{4.5}$$

Shear velocities were calculated from the predictions of dissipation rate of turbulent kinetic energy as

$$u_* = (\epsilon \kappa z)^{1/3}, \tag{4.6}$$

where $\kappa = 0.4$ is the von Karman's constant and z is the height above the bed.

Moreover, the river was partitioned into meander bends and straight sections, to investigate the potential effect of channel geometry on SSC. First, a local sinuosity index, SI, was computed for each grid cell along the river domain. The index SI is equal to the ratio of the along-channel length by the distance of the corresponding straight line between two points (if SI equals 1, then the section in completely straight). A threshold of 1.0007 was selected to categorise the river domain, dividing the river into 16 bends and 15 straight sections, as can be seen in Figure 4.2b. A more detailed explanation of the sinuosity index and river typology is given in Dejeans et al. (2022).

4.3 Results

Given the performance of the model in terms of its ability to reproduce the flow speeds and turbulent structure was the focus of Dejeans et al. (2022) and Dejeans, Mullarney, and MacDonald (Dejeans et al.), we predominantly focus here on the results concerning the predictions of SSC. However, given the slight changes in model setup, we nonetheless include a brief synopsis of the predictions of flow speeds and dissipation rates of turbulent kinetic energy for completeness. Following the classification scheme of Sutherland et al. (2004), the model performance was assessed as 'excellent' in an Eulerian frame-of-reference by comparing predictions and observations of water levels and currents from the centre of the model domain (red cross on Figure 4.2a).

As in Dejeans et al. (2022), the model results were further analysed by comparison with Lagrangian (flow-following) observations (drifters). Figure

4.3a shows an example of the observed Lagrangian speeds (black dots) and the corresponding model output, predicted by the model with the k-ϵ and the k-L turbulence closure schemes for the three cases simulated. Similarly, Figure 4.3b gives an example of the distribution of the dissipation rates of turbulent kinetic energy for the same drifter release. As in Dejeans et al. (2022), in all scenarios, the model is able to reproduce the larger-scale along-river patterns of flow speeds along the river, and in general, also the right order of magnitude for the dissipation rates of turbulent kinetic energy. However, smaller-scale variability is not captured. Model performance across all the drifter releases (all drifters for all three days) is summarised in Appendix B, in Table B.1, which shows the root mean squared error statistics. There are minimal differences in model performance between the k-ϵ and the k-L closure schemes across the three different cases simulated. However, in contrast to Dejeans, Mullarney, and MacDonald (Dejeans et al.), the more sophisticated turbulence closure scheme, the two-equation k-ϵ model here, performs slightly better than the simpler k-L model. However, in all cases, the model was considered sufficiently robust in terms of hydrodynamic performance to allow for examination of the sediment transport processes.

Figure 4.4 shows the Lagrangian observations of suspended sediment concentrations for days 2 and 3 (for which the full complement of three drifters were deployed), and the corresponding model predictions for the three cases, for the k-ϵ and the k-L turbulence closure schemes. The observations indicate that, during the time of the experiment (ebb tide), the observed suspended sediment concentration varied between 0 and about 850 $\mathrm{mg.L^{-1}}$ and the flow-following Lagrangian distribution exhibited an increase in concentrations as the drifters are advected downstream. There are some regions in which SSC is locally augmented; this is particularly evident for the SSC estimates observed by two upstream drifters (see distances between 7,000 and 10,000 m in Figure 4.4a, b, d, and e).

Model results for a movable sediment bed but no input from upstream

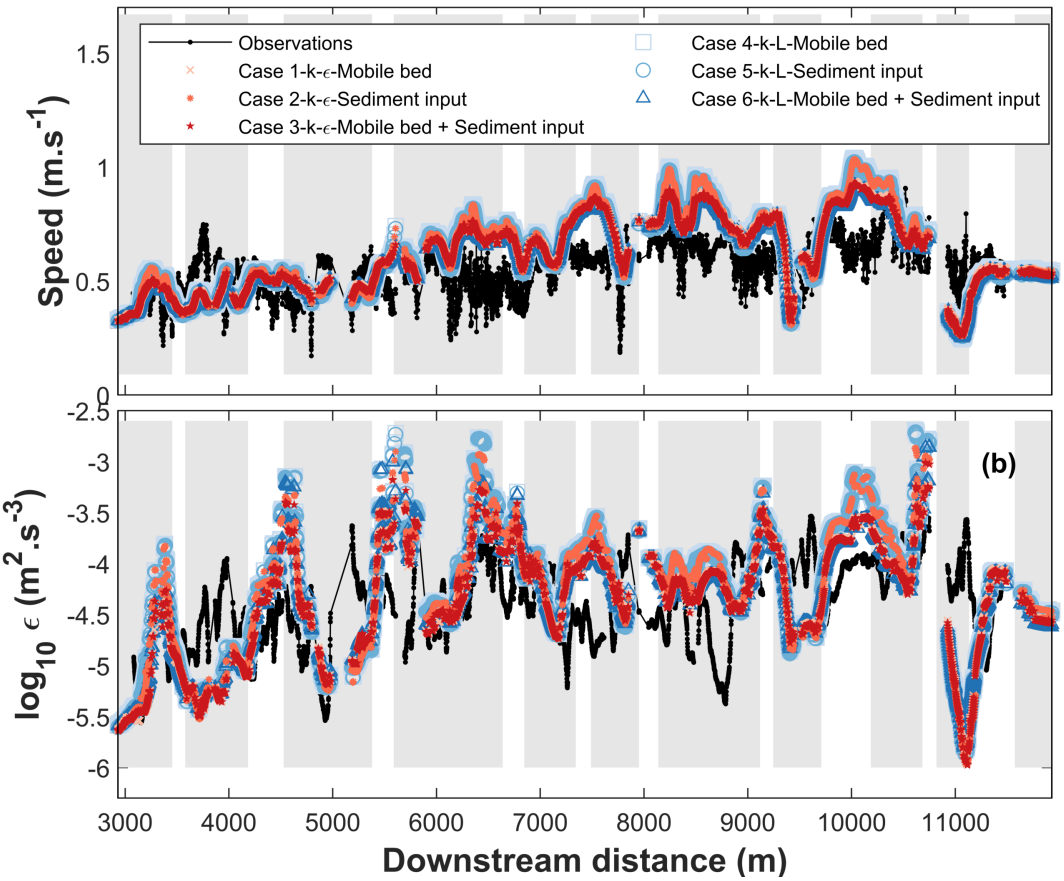

Figure 4.3: (a) Observed (black dots) horizontal flow speeds from the drifter released in the middle of the river on day 3 (we note that values are depth-averaged over a 73-cm profile) and the corresponding predictions, according to (red markers) the k-ϵ turbulence closure scheme for cases 1, 2, and 3 (crosses, asterisks, and stars, and light to darker shades, respectively), and (blue markers) the k-L turbulence closure scheme for cases 4, 5 and 6 (squares, circles, and triangles, and light to darker shades, respectively). The grey shaded areas correspond to the locations of the bends.

(for both the k-ϵ and the k-L turbulence closure scheme, cases 1 and 4) show increasing sediment concentrations downstream as velocities increase (Figure 4.5) (e.g., Vanoni, 1975). Starting from a clear water mass (SSC=0), sediment is resuspended off the bed increasing concentrations in the water column. In general, after an initial adjustment period, rates of SSC increase are similar to those observed for the drifters upstream (Figure 4.5a, b, d, and e), particularly in the upstream sections of the river. In the downstream section, the model predictions tend to overestimate SSC (Figure 4.5c and f). While the general downstream trend is reasonably well reproduced, the model fails to reproduce

the mid-scale (O(km)) variability such as the locally enhanced SSC at 7,000-8,000 m or reductions (e.g., at 7,900 m) shown in Figure 4.4b. For runs with upstream sediment input, and a fixed bed, for both the k-ϵ and the k-L formulations (cases 2 and 5), the predictions show that the sediment discharged from the upstream boundary is gradually deposited and advected downstream for around 5,000 m until concentrations level off (panels a and d of Figure 4.4). The predictions corresponding to the drifters released from the middle location show minimal variation in SSC, with a slight amount of resuspension occurring during mid-tide (which corresponds to distances around 6,000-10,000 m) and subsequent deposition toward the end of the ebb tide (distances around 10,000-12,000 m). For the cases 2 and 5 (upstream sediment input and fixed bed) and for the drifter released at the furthest downstream location, SSC predictions over the entire track remain close to zero. Under these conditions, there is minimal availability of deposited sediment to resuspend as the majority of the sediment released at the upstream boundary has settled out before reaching this section of the river.

The differences in predicted SSC between the k-ϵ and the k-L turbulence closure schemes for each set of forcing conditions are shown in Figure 4.6. The differences between case 4 and case 1 (mobile bed, no sediment input) are the largest whereas the differences between case 5 and case 2 (fixed bed, upstream sediment input) are the smallest (which was expected given the total SSC values are small). The differences between closure schemes are however relatively consistent along the river, with differences typically increasing with distance downstream. Overall, differences between closure schemes remain below 40 mg.L^{-1} (4.7 %) and are usually below 15 mg.L^{-1} (1.8 %). The largest differences are observed on day 3, between cases 4 and 1 (mobile bed, no sediment input), and increase downstream (reaching a maximum of 50 mg.L^{-1}) until about 12,000 m, beyond which the river straightens out (see Figure 4.4).

To examine what drives the local (km-scale) variability in the model, the longer-scale along-river trend both in SSC and shear velocity was removed from

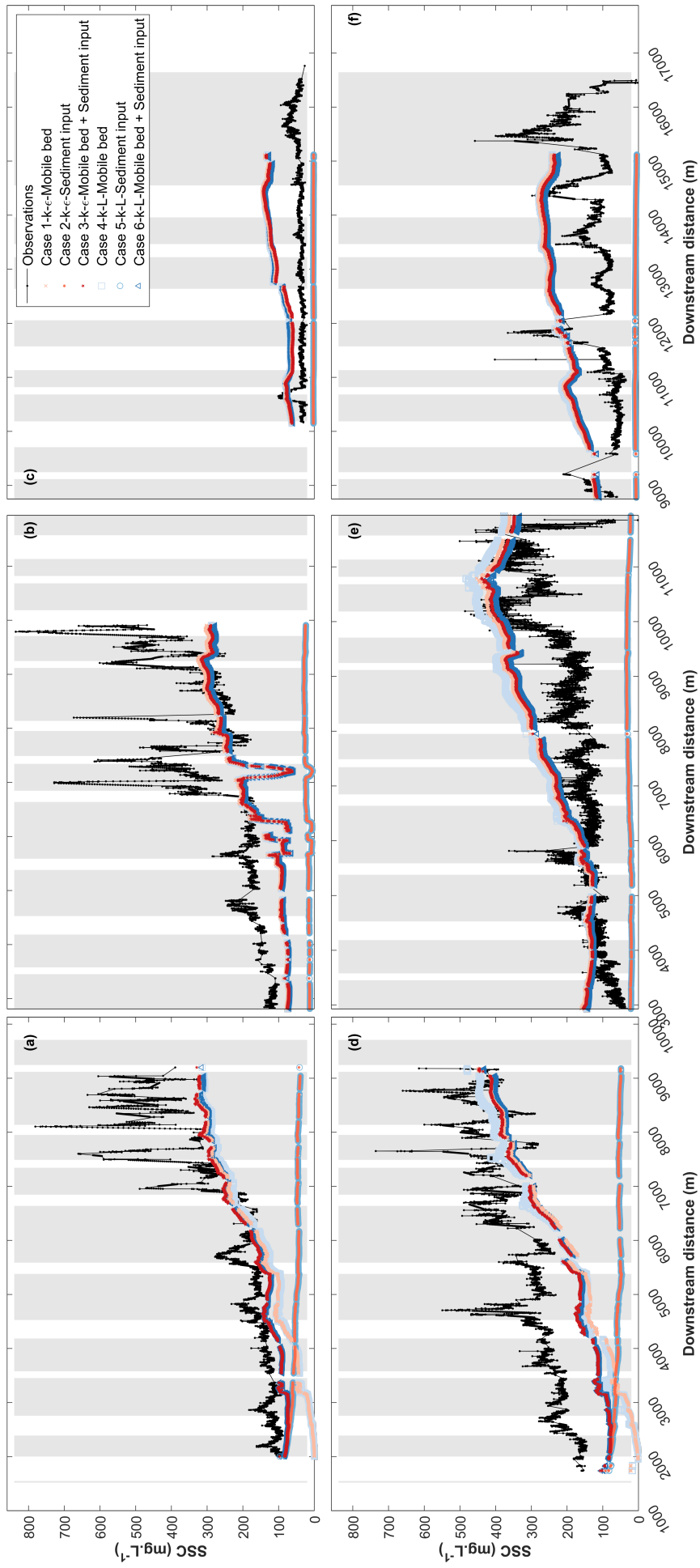

Figure 4.4: Observed (black dots) suspended sediment concentration (SSC) from the drifters released on (a-c) day 2 and (d-f) day 3 and the corresponding predictions, according to (red markers) the k-ϵ turbulence closure scheme (case 1 (crosses), case 2 (asterisks), and case 3 (stars)) and (blue markers) the k-L turbulence closure scheme (case 4 (squares), case 5 (circles), and case 6 (triangles)). The grey shaded areas correspond to the locations of the bends.

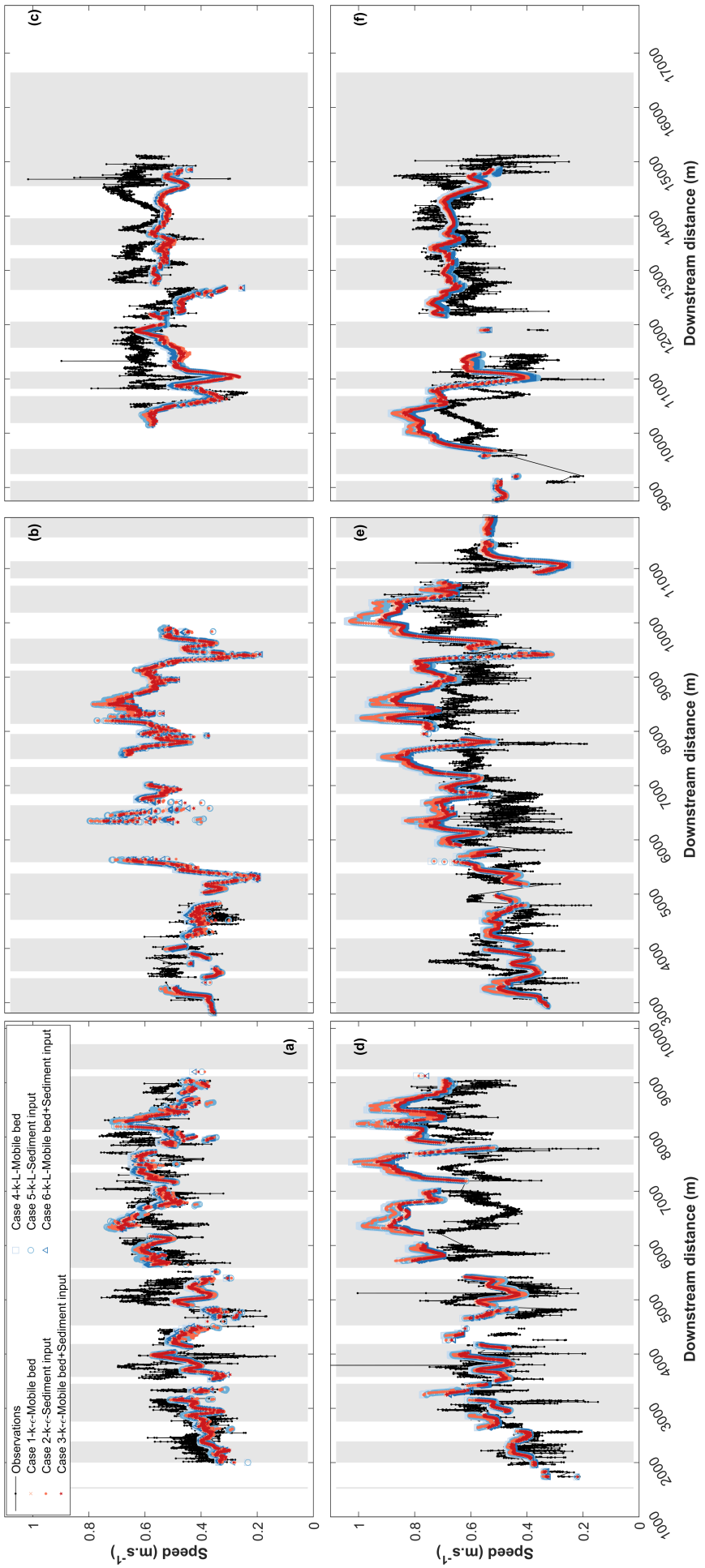

Figure 4.5: Observed (black dots) horizontal flow speeds from the drifters released on (a-c) day 2 and (d-f) day 3 (we note that values are depth-averaged over a 73-cm profile) and the corresponding predictions, according to (red markers) the k-ϵ turbulence closure scheme (case 1 (crosses), case 2 (asterisks), and case 3 (stars)) and (blue markers) the k-L turbulence closure scheme (case 4 (squares), case 5 (circles), and case 6 (triangles), respectively). The grey shaded areas correspond to the locations of the bends. We note the absence of observed speeds after about 5,000 m for the drifter released from the middle location on day 2 (b) due to a defective GPS.

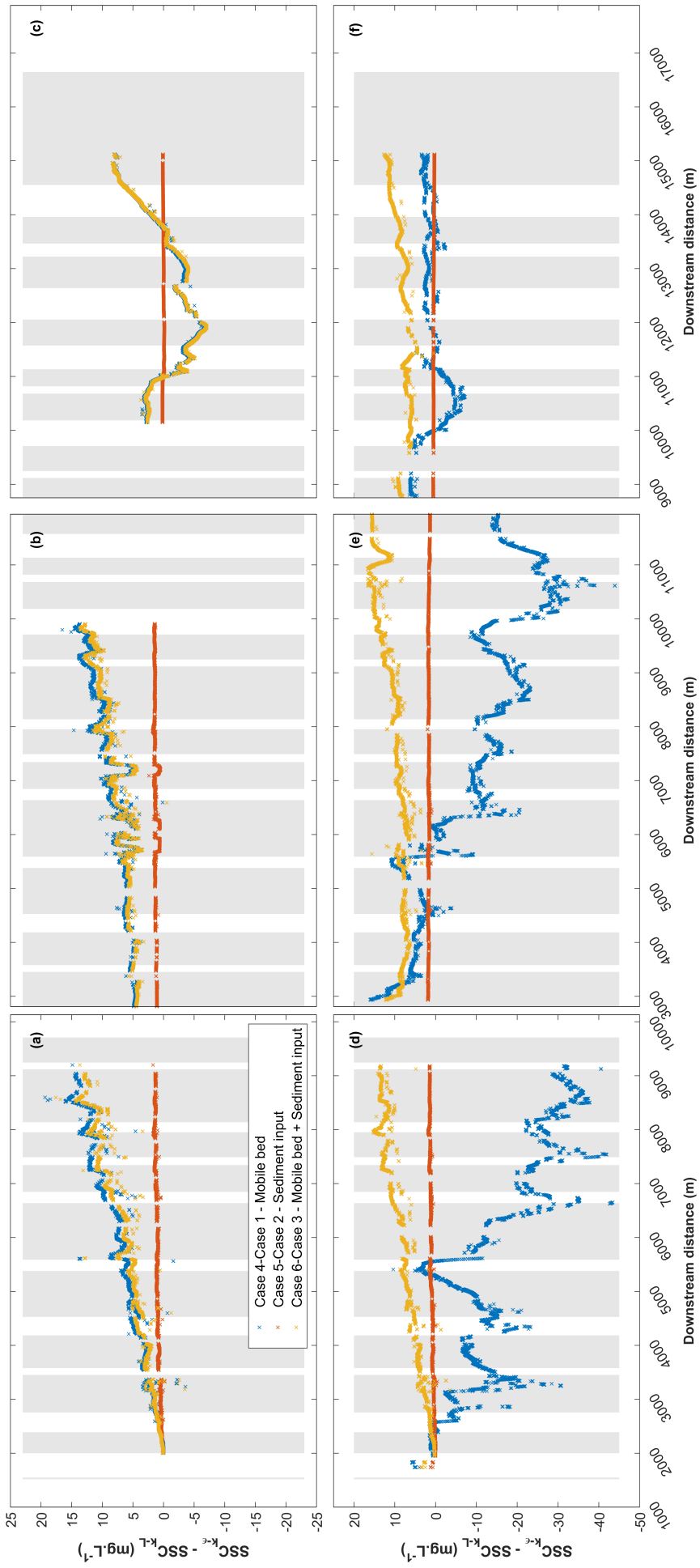

Figure 4.6: Difference between the suspended sediment concentration predicted by case 1, case 2 and case 3 (k-ϵ turbulence closure scheme) and case 4, case 5 and case 6 (k-L turbulence closure scheme), respectively. Example of the drifter released in the middle of the domain on day 3. We note the difference in range of the y-axis between the two rows (smaller range on day 2 (a, b, and c) compared to day 3 (d, e and f)).

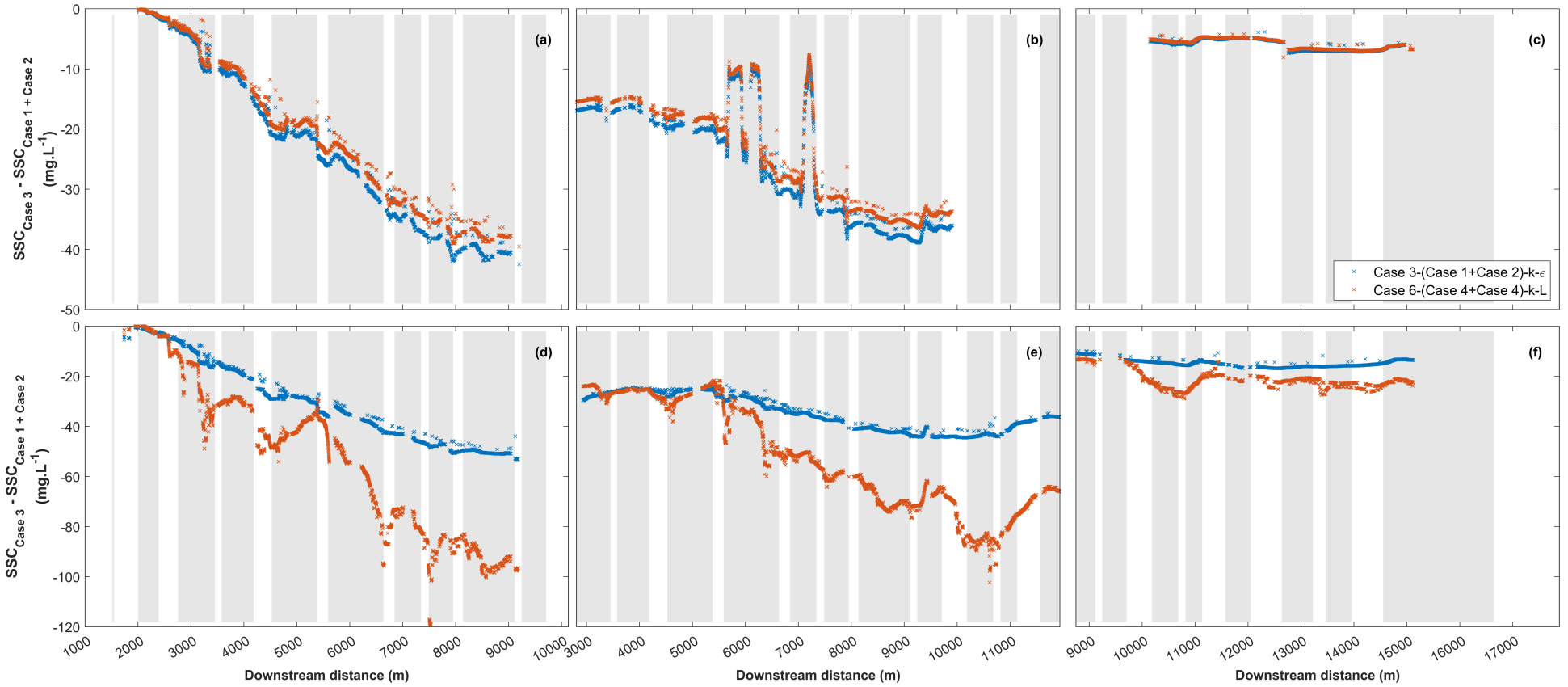

Figure 4.7: Difference (blue) between the suspended sediment concentration predicted by case 3 and the sum of case 1 and case 2, as predicted by the k-ϵ turbulence closure scheme and difference (orange) between the suspended sediment concentration predicted by case 6 and the sum of case 4 and case 5, as predicted by the k-L turbulence closure scheme. We note the difference in range of the y-axis between the two rows (smaller range on day 2 (a, b and c) compared to day 3 (d, e and f)).

the signal (by subtracting the moving average over windows of 1,000 m). Figure 4.8 shows an example of the km-scale variability from the model predictions (case 3, upstream sediment input and movable bed, k-ϵ turbulence closure scheme). Panel (c) shows a linear fit between the shear velocity and SSC. Of note, the variability in u_* over the km scales ($\sim 0.06\,\mathrm{m.s^{-1}}$ over 1 km) is around twice the gradual along-river change ($\sim 0.03\,\mathrm{m.s^{-1}}$ over 9 km).

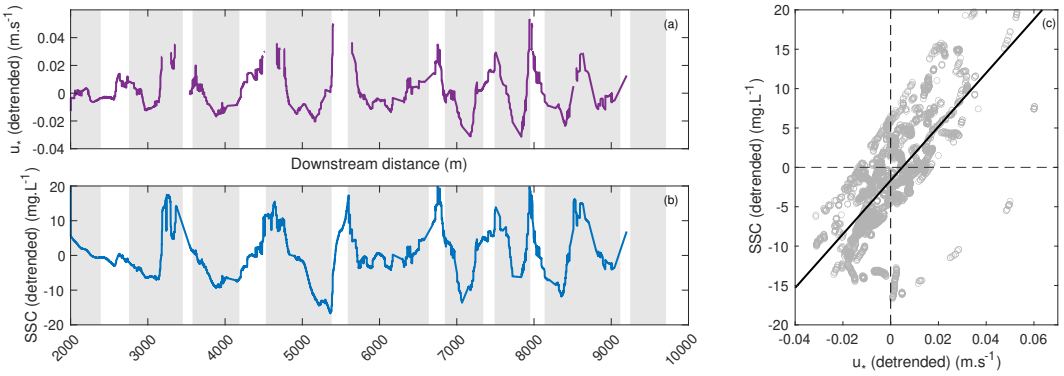

Figure 4.8: (a) Modelled along-river distribution of detrended (a) shear velocity u_*, and (b) SSC from the drifter released in the upstream section of the domain for case 3 (k-ϵ turbulence closure scheme, upstream sediment input and mobile bed). (c) Comparison of SSC and u_*. The black lines corresponds to a linear fit ($r^2 = 0.512$, p-value$\ll$0.01). The grey shaded areas correspond to the locations of the bends.

4.4 Discussion

The results presented here demonstrate that the predominant source of sediment in suspension in the water column within our model of the Kaipara River is sediment which has been eroded from the river bed. For model runs with a fixed bed and sediment input at the upstream boundary (cases 2 and 5), suspended sediment concentrations were much smaller than observed, and the sediment entering through the upstream boundary was initially deposited (in the first 5,000 m). While the forcing was idealised to a constant flux, values were around those observed in the field in the upper portion of the domain ($100\,\mathrm{mg.L^{-1}}$). Conversely, for model simulations with a movable bed, after an

initial adjustment period at the beginning of the ebb tide in which flow speeds increased, suspended sediment concentrations were similar to those observed in the field and the model did an excellent job of capturing the overall trend of increase (with both time and distance) along the river, noting that the model is not expected to reproduce the exact distribution of SSC since the upstream forcing is idealised. Given the importance of resuspension, SSC values are unsurprisingly positively correlated with horizontal flow speeds and, consequently, bed shear stresses (we note that we do not have observations of bed shear stresses from the field experiment). This correlation implies that, when flows are overpredicted, the SSC is also likely to be overestimated (e.g., Figure 4.4b). Decreases in SSC from both observations and model predictions further downstream (from about 10,000 m on Figure 4.4c and f) are thus associated with slower flow speeds (and hence less resuspension) as the cross-sectional area of the river becomes larger.

The broad-scale along-river SSC patterns shown in the model results are relatively consistent between the simulations across the different days, with low concentrations and minimal variability in SSC for distances up to ∼5,000 m (corresponding to concentrations around 50-100 $mg.L^{-1}$), beyond which concentrations increase close to linearly up to 10,000 m (corresponding to SSC up to 400 $mg.L^{-1}$) (Figure 4.4). The general trends in SSC are well represented in the numerical model results, which is especially notable given the number of simplifications applied in model setup. However, much of the smaller-to-medium scale (O(100-1,000 m)) variability seen in the observations is not captured. Some features, such as the local and brief augmentations in suspended sediment concentrations around 8,000 and 9,800 m in Figure 4.4, appear consistently at the same location, regardless of the day or the tidal stage (i.e., for different drifters). These features are thus likely owing to fixed geographic features such as the presence of a small river (e.g., at 8,000 m). Such increases are not reproduced by any of the model cases as additional river inputs are not included in the model. However, additional freshwater inputs can locally

increase SSC both by inputting sediments and also by promoting sediment resuspension by enhancing flow speeds (e.g., Shenliang et al., 2003).

Variability between the observed SSC from different days (despite tidal and river forcing being relatively similar across days) is likely owing to processes which are not represented in the model. All three cases fail to reproduce the local large (about 500 $\mathrm{mg.L^{-1}}$) increases of suspended sediment concentration on day 2 (e.g., around 7,000-8,000 m in Figure 4.4b). These local and temporary increases in SSC could be explained by the presence of winds. While local winds were not measured during the experiment, hourly wind data from two nearby weather stations revealed that winds were overall light during the drifter deployment (Dejeans et al., 2022). However, on day 2, wind gusts (with speeds reaching 9.7 $\mathrm{m.s^{-1}}$) occurred around the time of the increases in SSC during day 2. Wind-induced waves in shallower regions of the river may also have promoted some local resuspension, which then drains into the central portion of the channel.

While the predictions of SSC in model runs with both upstream input and resuspended sediments from the bed closely resemble those from the runs with bed resuspension alone (cases 1 and case 4), the resulting SSC predictions are not a simple linear superposition of the runs with the two processes (Figure 4.6, which shows the difference between the concentrations from the cases with both a mobile bed and upstream sediment input and the sum of the concentrations from the cases with the mobile bed and upstream input applied separately). The differences in predictions of the runs with both inputs compared to the sum of the individual processes are more pronounced when using the k-L turbulence closure scheme. While the reason for these differences are not clear, the result nonetheless implies that there exists some nonlinear interaction between the advection and resuspension processes.

Particles within the model are represented by a single size class ($\mathrm{d_{50}}$=10 μm) and no parameterisation is included for flocculation. Observations from the cameras on the FlocDrifters revealed that, in the field, the median floc size

increased with suspended sediment concentration (MacDonald and Mullarney, 2015), thus it might be anticipated that SSC in the model would be overpredicted for times with larger concentrations (as the individual particles had slower settling velocities). However, this overprediction did not occur; in general, model predictions of SSC were underpredicted for those times when larger flocs were present in the observations. While this result appears counter-intuitive, these times also correspond to times with faster flow speeds, hence hydrodynamic conditions may have been sufficient to keep even the larger flocs in suspension. To verify this explanation, we compare the settling velocity of the flocs observed in the field to the shear velocity predicted by the model.

Following Khelifa and Hill (2006) (their equation 18), we estimate the floc settling velocity, w_f as

$$w_{\mathrm{f}} = \frac{1}{18}\theta g \frac{\rho_s - \rho_w}{\mu} d_{50}^{3-F} \frac{D_{50}^{F-1}}{1 + 0.15\mathrm{Re}^{0.687}}\phi, \tag{4.7}$$

in which D_{50} and d_{50} are the median diameters of the flocs and primary particles, respectively, θ is a particle shape factor, μ is the dynamic viscosity of waster, ϕ is a size distribution shape factor (= 1 for monosized particles), and Re is the particle Reynolds number of the flocculated particle ($D_{50}w_f/\nu$), where ν is the kinematic viscosity. F is the fractal dimension of the floc and decreases with floc size following the power law approximation given in Khelifa and Hill (2006). Setting $\theta = \phi = 1$, $\rho_s = 2300\,\mathrm{kg.m^{-3}}$, $\rho_w = 1020\,\mathrm{kg.m^{-3}}$, $\mu = 1 \times 10^{-3}\,\mathrm{kg.m^{-1}s^{-1}}$, $\nu = 1 \times 10^{-6}\,\mathrm{m^2.s^{-1}}$ and $d_{50} = 10\,\mu\mathrm{m}$ yields estimated values of $w_f = 0.36$ to $5\,\mathrm{mm.s^{-1}}$. In general, we find that the shear velocities (at the height of the drifter in the model) are 20-100 $\mathrm{mm.s^{-1}}$, which is at least one order of magnitude larger than the floc settling velocity, indicating that vertical mixing is sufficiently strong to reduce settling. We note that Delft3D can include a parameterisation for flocculation which implements a variable settling velocity as a function of salinity. However, observations from several field experiments (e.g., Eisma et al., 1980, 991a,b) have shown no consistent

evidence in support of salinity-driven flocculation, hence this approach was not explored further at this time, but the sensitivity of the sediment transport predictions to such a parameterisation could be examined in future work. Additionally, some smaller scale variability in observations may be due to the influence of turbulence on floc size, either enhancing floc formation and increasing settling velocity, or for regions of more intense turbulence, inducing floc breakup and promoting smaller particle staying in suspension (the data is weakly suggestive that maximum floc size increased with ϵ up to $10^{-5}\,\mathrm{W.kg^{-1}}$, but decreased for larger values of ϵ).

The strong correlation between the variability in shear velocity and SSC (Figure 4.8) over length scales of order of 1 km indicates that either vertical mixing and/or additional resuspension from the bed exerts a strong local control over the near-surface SSC. These moderate changes in SSC (around $40\,\mathrm{mg.L^{-1}}$) and large changes in shear velocities ($0.05\,\mathrm{m.s^{-1}}$) are associated with changes in river geometry: the slower shear velocities and smaller SSC occur at bends, while the locally elevated SSC and faster u_* occur in the straighter sections of the river (Figure 4.9). One particularly striking feature of these changes is that they occur over remarkably short length scales ($\sim$100 m). While noisier, the same pattern of enhanced SSC in the straighter sections is also seen in the observations (Figure 4.9c), although the magnitude of the SSC and the variability is much larger (likely owing to winds on this day as noted previously). This result is consistent with the field observations showing smaller dissipation rates of turbulent kinetic energy at the bends (Dejeans et al., 2022) (noting no measurement of depth below the instruments were obtained, thus an equivalent u_* could not be calculated).

4.5 Conclusion

We have presented observations and numerical modelling of SSC along the fluvial-to-marine stretch of a muddy tidal river. Data was collected during

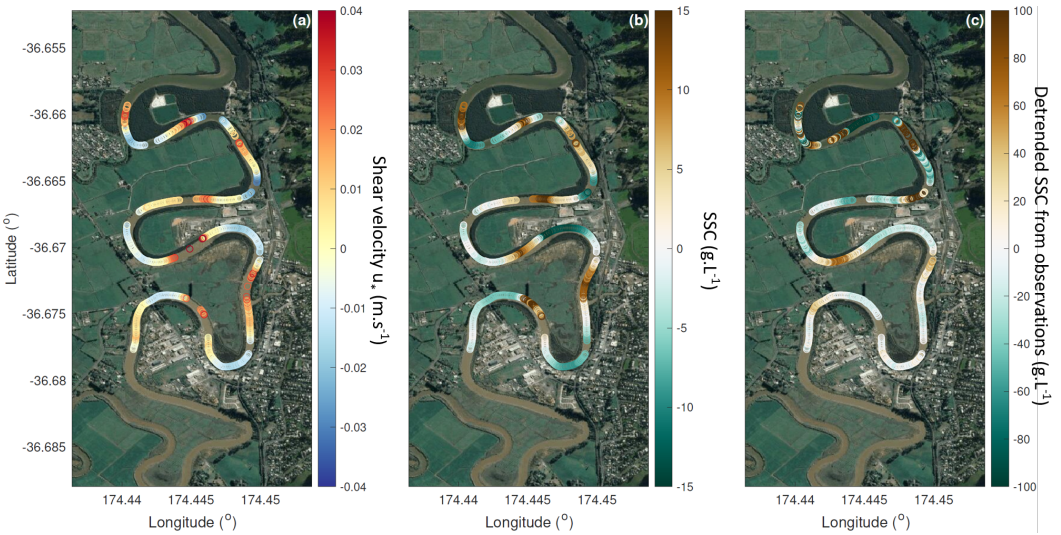

Figure 4.9: Modelled along-river distribution of detrended (a) shear velocity u_*, and (b) SSC from the drifter released in the upstream section of the domain for case 3 (the k-ϵ turbulence closure scheme, upstream sediment input and mobile bed). (c) Detrended SSC from observations. Note in (c), at three locations the detrended SSCs are off-scale on the colourbar (values reach up to 350 mg.L^{-1} so appear saturated), to prevent the variability in upstream sections on the river being obscured.

ebb tide using a novel flow-following frame of reference. Numerical results demonstrated that sediment in suspension was predominantly resuspended from the bed with minimal amounts advected from upstream. Observations revealed that suspended sediment concentrations, velocities, horizontal flow speeds, and floc sizes increased in the downstream direction (changing in both space and time). Local changes in SSC were strongly correlated with shear velocities which were much larger (several times) in straight sections of the river. Despite simplified forcing conditions, the model was able to reproduce the larger-scale along-channel structure of SSC. In particular, the model was not found to be sensitive to the lack of parameterisation of the flocculation process, as turbulence and velocities remained sufficiently high to transport the larger flocs and reduce settling, at least over the conditions observed during the experiments.

Chapter 5

Conclusions

5.1 Review of major concepts and key findings

5.1.1 Review of major concepts

The research presented in this thesis aimed to enhance our understanding of the physical processes and the modelling of hydrodynamics, turbulence and sediment transport within a tidally influenced river. In Chapter 1, the aims of the thesis were divided into three sets of research questions.

1. Is there any advantage to using a Lagrangian approach for the validation of a hydrodynamic model? Can a hydrodynamic model reproduce (a) overall trends and (b) small-scale variability in Lagrangian observations of flow speeds and dissipation rates of turbulent kinetic energy when using the commonly applied k-ϵ turbulence closure scheme? Can we distinguish between different controls on the large- and the small-scale hydrodynamics?

Previous work has shown the importance of meander bends (both in terms of curvature and amplitude) and bathymetry on flow behaviour in rivers. The focus of Chapter 2 is on predictions of flow speed and turbulence within the fluvial-to-marine transition zone of a meandering river by a three-dimensional

numerical model, using the k-ϵ turbulence closure scheme. More precisely, the present work aimed to investigate the performance of a model, developed with the Delft3D suite, in terms of flow speed and ϵ. The model was first calibrated using a standard Eulerian approach and the model results were compared with high-resolution Lagrangian observations.

After the 'standard' Eulerian calibration, model results were compared with observations in a Lagrangian frame of reference, with the drifters being advected downstream. More precisely, observations averaged over a small profile (73 cm) were compared to predictions from the corresponding model layer. Generally, both observations and predictions showed slower speeds around the bends and faster speeds along straighter sections of the channel. In general, the overall order of magnitude and the changes in flow speeds downstream are relatively well predicted by the model. Thus, a Lagrangian approach was found to offer a more stringent validation than standard Eulerian approaches.

Generally, the model also predicted the right order of magnitude in terms of dissipation rates of turbulent kinetic energy with regards to the observations. Nevertheless, the model tended to underpredict the values of ϵ (the average and the maximum differences between model predictions and observations are about $7.25 \times 10^{-5}\,\mathrm{m^2.s^{-3}}$ and $1.5 \times 10^{-3}\,\mathrm{m^2.s^{-3}}$, respectively), and was not able to reproduce the smaller scale variability in ϵ. The largest errors in predicting ϵ were localised around the bends, where the predictions were smaller than the observations. Observed differences in overlapping sections (same location, different day) were also not reproduced by the model, which predicts similar values at similar locations across the three days.

The model predictions of velocities and dissipation rates of turbulent kinetic energy for the same locations but for different days were relatively consistent despite variations in tidal and freshwater forcing. This consistency between days suggests that the bathymetry and the geometry of the river are the main factors controlling turbulence in our model. The model was not able to fully reproduce the variability observed across different days, which is likely due

to the presence of winds, not included in the model. Model performance was also worse in regions with bends, which is in agreement with the findings of previous studies who also found that the RANS approach was not able to accurately predict the secondary flows and the streamwise vorticity field in an Eulerian frame of reference.

While drifters have been used in past studies for a variety of measurements in shallow environments, combining the use of drifters and model predictions of turbulence is a relatively new approach, and the similarities between Lagrangian observations and model predictions increase the confidence in the model performance. Indeed, using flow-following observations allows the examination of the model performance over a wide range of scales, from the full river domain (approximately 15 km) to meander bends (a few meters). In particular, the Lagrangian observations not only highlighted that ϵ could fluctuate over up to two orders of magnitude across the whole river domain but also that ϵ could substantially vary over smaller sections (e.g., a few meters), and especially around the bends. An Eulerian approach would require a significant number of instruments to come to the same conclusions, which means that using a Lagrangian approach is an effective and economic strategy to validate numerical models.

2. Is the more sophisticated two-equation k-ϵ turbulence closure scheme better at reproducing Eulerian and Lagrangian speeds and dissipation rates of turbulent kinetic energy than the simpler one-equation k-L turbulence closure scheme?

Research in Chapter 3 extended the work of Chapter 2 to compare the model results using the k-L turbulence closure scheme with the model results using the k-ϵ turbulence closure scheme. Although it is typically more common to use a more sophisticated model, such as k-ϵ, simpler formulations (e.g., algebraic) have sometimes been shown to being able to better predict some of the anisotropic characteristics of turbulence. As in the previous chapter,

this comparison was based on a Lagrangian frame of reference and results with both turbulent closure schemes are examined in contrast with the flow-following observations collected within the Kaipara River.

Like with the k-ϵ turbulence closure scheme, the standard Eulerian calibration of the model using the k-L turbulence closure scheme was classified as 'excellent'. Moreover, the results of flow speeds were similar with both closure schemes, which reproduced the right order of magnitude and overall right pattern of flow speeds when compared to Lagrangian observations but could not predict the smaller scale variations, especially around the bends. In a similar manner, the model results of dissipation rates of turbulent kinetic energy exhibited strong similarities when computed with the k-ϵ and the k-L turbulence closure schemes. Both models could reproduce the right order of magnitude and the general pattern of ϵ along the river domain. However, neither of the models could predict the smaller scale variations of ϵ, especially around the bends.

In Chapter 3, the river domain was divided into bends and straights, which quantitatively showed that larger errors were found in the bends with higher sinuosities. Both the k-L and the k-ϵ models showed the same trends and similar error values for the flow speeds, confirming that the model results of flow speeds were not sensitive to the turbulence closure scheme. While results were not particularly sensitive to closure scheme, we nonetheless found that, in terms of ϵ, the simpler k-L turbulence closure scheme tended to predict relatively smaller errors within the bends than the more sophisticated k-ϵ turbulence closure scheme. This result suggests that, instead of using the default closure scheme (i.e., k-ϵ), users of Delft3D who study hydrodynamics, especially in tidally driven meandering river, could use simpler formulations (e.g., k-L for Delft3D) in order to save time and computational resources.

3. What are the dominant controls on suspended sediment transport in a tidally influenced river? Does the Lagrangian approach allow for examination

of the processes involved in the erosion and deposition of sediment in the river? Do flocculation processes strongly influence the distribution of suspended sediment concentration in the water column?

The work of Chapter 4 is an extension of the work of Chapter 2 and Chapter 3, which includes sediment transport processes in order to assess the controls on transport, deposition, and erosion of particles. A numerical modelling approach allowed for systemic inclusion and exclusion of different physical processes. Here, we considered bed exchange and advection processes, at first separately and them combined.

Model predictions show that the main source of suspended sediments comes from resuspension of the river bed. Although the model forcing was idealised in terms of upstream sediment input, the model reproduced the along-channel patterns of the observations of SSC, and also the trend of enhanced SSC in the straight sections and reduced SSC around the bends. However, the model underpredicted the magnitudes of these local changes, likely owing to the omission of some processes in the model (e.g. wind-induced waves). Some of the additional smaller-scale behaviours appearing in the observations were also not captured by the model and were likely due to the presence of external geographic features (e.g., freshwater input). Unexpectedly, since the median floc sizes were observed to augment with suspended sediment concentrations, model predictions of SSC were generally underestimated by the model, thus implying that fast flow speeds were sufficient to prevent settling for even the largest flocs observed.

5.1.2 Key findings

A number of findings presented in this thesis have practical applications. Firstly, the combination of the Lagrangian and Eulerian approaches requires the use of a smaller number of instruments than a sole Eulerian approach to cover the same strech of river. Combining Lagrangian and Eulerian strategies has therefore been proven to be an effective and economic strategy for numer-

ical model validation. Secondly, when dealing with hydrodynamics alone, the use of the simpler k-L has been proven to be satisfactory, performing as well as the more sophisticated k-ϵ turbulence closure scheme. This finding suggests that, when studying hydrodynamics, users of Delft3D could use the simpler k-L turbulence closure scheme, instead of the default more sophisticated k-ϵ, thereby saving computational time and resources. We note that this finding does not remain when including sediment transport. For these simulations, the more sophisticated k-ϵ turbulence closure scheme performed better than the simpler formulations. Finally, along the majority of the river, conditions were sufficiently energetic that even the flocculated particles did not settle out. This result suggests that, under similar riverine conditions, a simple representation of particles (i.e., a fixed particle size and settling velocity) may be sufficient for modelling and management purposes.

5.1.3 Limitations of the work

The work presented in this thesis has several limitations, which need to be acknowledged. Firstly, some of the model set up could be improved, provided more resources (both funding and time). For example, a set of more refined bathymetry data could be collected. Additionally, model boundary conditions could be improved by collecting supplementary data at the exact location of the model boundary rather than using freely accessible datasets which were located further away from the grid. Secondly, some processes, such as winds and waves were not included in the model, although these are likely to have an impact on the hydrodynamics within the river. Moreover, like every model, Delft3D uses simplifications. We note that one of those simplifications is the hydrostatic assumption, which was found to work well in environments with sharp bends. Indeed, Parsapour-Moghaddam and Rennie (2017) modelled a meandering river in Delft3D and found that a hydrostatic model could reproduce the vertical distribution of streamwise velocity better than a nonhydrostatic model, because (a) the interaction between the secondary flow and

the vertical distribution of the streamwise velocity is significant (Blanckaert and De Vriend, 2004, 2010) and (b) the main secondary flow is dominated by advective momentum transport, which is responsible for redistributing the streamwise velocity (Blanckaert and Graf, 2004); the 3D hysdrostatic formulation takes into account the advective momentum transport by the secondary flow. Other modelling approaches, such as LES, could have led to a more accurate representation of turbulence, however thes approaches would have been outside the scope of this project, which aimed at assessing the performance of Delft3D, as this package is commonly used by practitioners. Additionally, above 400 mg.L-1, flocs were not able to be resolved by the FlocCam, so there remains a gap in knowledge for these large SSC regimes (MacDonald and Mullarney, 2015).

5.2 Recommendations for future research

5.2.1 River system modelling

Numerical modelling is a powerful tool to investigate hydrodynamics, and particularly turbulence, as well as sediment transport in shallow waters. We note, however, that we simplified the model to allow for first order investigation of the underlying dynamics, which means that several processes were not included. For future work, a sensitivity analysis could be undertaken in order to quantify to what extent, and over which regions of the parameter space, these additional processes can be neglected.

In particular, in chapter 2, results revealed that the model did not predict differences in ϵ between days and it was suggested that these unresolved differences could be explained by the absence of wind forcing. Indeed, wind has been previously shown to create vertical mixing and promote destratification in the water column (e.g., Chao, 1988). Moreover, the breaking of waves, which can be generated by wind, was also observed to create turbulence (e.g., Craig and Banner, 1994). The inclusion of wind forcing should therefore be considered

in order to improve the performance of the model. The relative effects of wind on different sections of the river, and especially the bends versus the straighter regions of the river with longer fetch, should be investigated. To undertake this analysis, new measurements at multiple different locations along the river would be particularly useful.

Additionally, another area in which the model did not perform particularly well was in salinity predictions. Future work could be undertaken to improve the accuracy of these salinity predictions. Errors likely arose from boundary conditions, hence these could be refined. Indeed, rather than using vertically constant salinity at the boundary, a profile of salinity could be applied. Moreover, such a step would require the collection of a more complete dataset at the location of the boundary (salinities time series from multiple heights or time series profiles over at least a few tidal cycles). The incorporation of this data would likely require a new calibration of the model to include salinity in the calibration stage, thus additional data of the middle site would also be needed. The addition of wind forcing is likely to affect the salinity at the surface, due to the generation of mixing.

5.2.2 Flocculation

Another process that was neglected in the model was flocculation. Flocculation makes sediment transport modelling more complex by changing the settling velocity of particles, which influences the resuspension and deposition of sediments. Flocculation has been shown to be particularly sensitive to turbulence (e.g., Winterwerp, 1998) but also to other parameters including salinity (e.g., Mietta et al., 2009). However, the extent of this dependence remains an active area of research. In Delft3D, flocculation can be implemented via a simple parameterisation, which includes the selection of two different settling velocities, based on salinity. The first settling velocity, WS0, corresponds to the settling velocity of the sediment fraction in fresh water (salinity equal to 0) whereas the second settling velocity, WSM, is the settling velocity of the sedi-

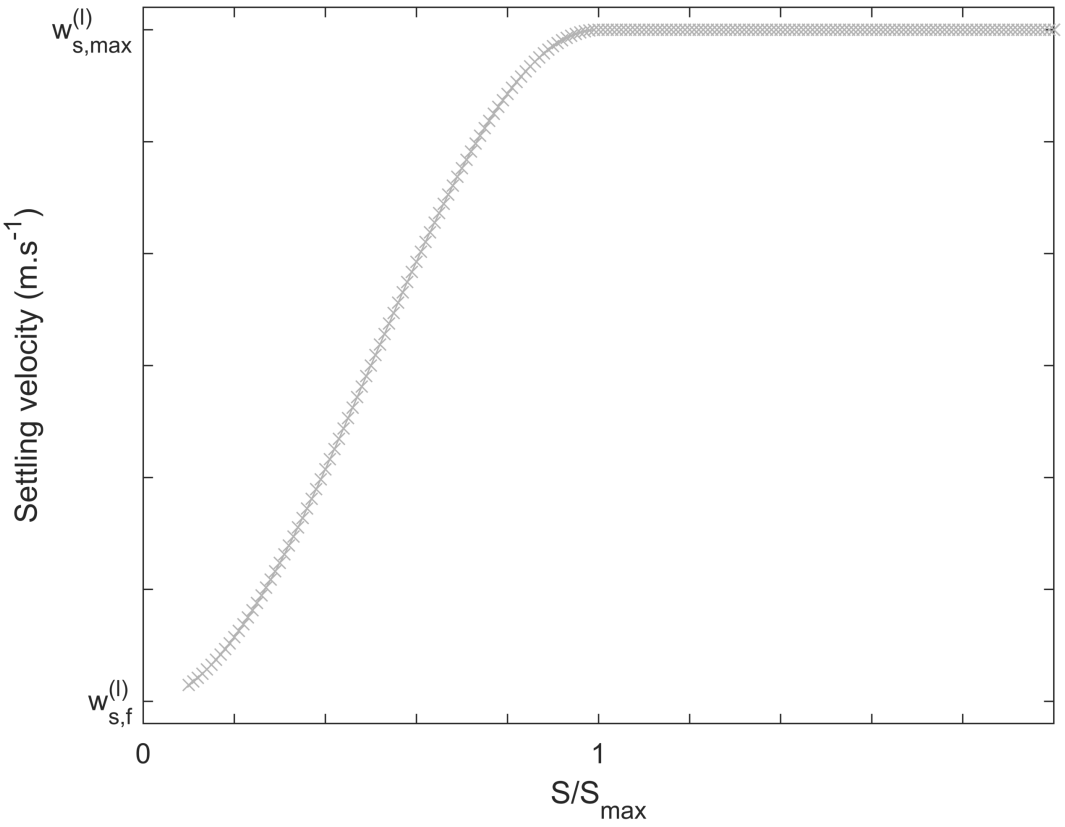

Figure 5.1: Settling velocity of the sediment fraction as a function of the salinity. The values $w_{s,max}^{(l)}$ and $w_{s,f}^{(l)}$ are the settling velocity of the sediment fraction (l) at the salinity concentration SALMAX and the freshwater settling velocity of (l), respectively. S is the salinity and S_{max} is the salinity at which WSM (settling velocity of (l) in saline water) is specified.

ment fraction in saline water, where the salinity is equal to a specific salinity, SALMAX. The settling velocity of the sediment fraction is then calculated using (Deltares, 2020):

$$w_{s,0}^{(l)} = \begin{cases} \frac{w_{s,max}^{(l)}}{2}\left(1 - cos(\frac{\pi S}{S_{max}})\right) + \frac{w_{s,f}^{(l)}}{2}\left(1 + cos(\frac{\pi S}{S_{max}})\right), \text{when S} \leq \text{S}_{max}, \\ w_{s,max}^{(l)}, \text{when S} > \text{S}_{max}, \end{cases} \tag{5.1}$$

where $w_{s,0}^{(l)}$ is the settling velocity of the sediment fraction (l), $w_{s,max}^{(l)}$ is the settling velocity of the sediment fraction (l) at the salinity concentration SALMAX, $w_{s,f}^{(l)}$ is the freshwater settling velocity of the sediment fraction (l), S is the salinity and S_{max} is the maximal salinity at which WSM is specified (Figure 5.1).

The addition of flocculation in the model may lead to a different distribution of the deposition/resuspension of cohesive sediment, especially in a parameter space where very large (macroflocs were formed), and simulations could be used to shed light on the importance of the flocculation process under different parameter spaces. However, the salinity distribution was not well reproduced in our model, so prior to implementing any form of parameterization of flocculation, it would be better to prioritise improving the predictions of salinity as mentioned in the previous section. In general, even this existing parameterization of flocculation still neglects turbulent processes and the influence of turbulence on the break-up of particles, thus flocculation processes remain an understudied area of sediment transport modelling.

5.2.3 Climate change and sea level rise

Coastal environments have been shown to be vulnerable to climate change and global warming, particularly through the intensification of storm surges and global sea-level rise (SLR). Storm surges can raise the level of the sea by more than 1 m, and cause severe damages to the surrounding environments, including river overflow (e.g., Cheikh and Momen, 2020). Church and White (2006) estimated the global SLR to be approximately $1.7 \pm 0.3\,\mathrm{mm.yr^{-1}}$. A study by Gehrels et al. (2008) revealed that the sea level in New Zealand has remained relatively constant over the past 7,000 years. However, they noted a significant increase in the last century, with a SLR of about $2.8 \pm 0.5\,\mathrm{mm.yr^{-1}}$.

Among the issues caused by SLR are flooding and salinisation, which have been shown to occur and pose a particular threat for riverine systems (e.g., Bhuiyan and Dutta, 2012). Water quality can be dramatically altered in case of flooding as a large quantity of water has the risk of carrying contaminants to the receiving environments. Moreover, model results simulating SLR in riverine environments have shown that higher sea levels would lead not only to an increase in tidal range but also to an increase in river salinity, stratification, and salinity intrusion moving upstream (Bhuiyan and Dutta, 2012; Hong et al.,

2020). Salt intrusion not only endangers fresh water availability, necessary for agriculture, industry and households but also jeopardizes the ecosystems of fresh water environments, such as freshwater fish species (e.g., Miah et al., 2004; Zhang et al., 2011).

In order to simulate the effect of sea level rise, the water level in the model can be artificially raised. Elevating the water level would likely also affect the salinity in the river. Indeed, the fresh-to-marine transition zone might move further upstream. Furthermore, the increase in water depth, especially during storm surges, could also lead to an increase in flow speeds, which can, in turn, lead to an increase in turbulence or a change in turbulence structure (Cheikh and Momen, 2020). The relative importance of these processes could be investigated and the feedback mechanisms could be examined.

5.3 Summary

This thesis investigates the performance of a hydrodynamic and sediment transport model in terms of flow speed, turbulence, and sediment transport. Although presenting a number of logistical and analytical challenges, the use of the combination of a Lagrangian approach with a more standard Eulerian approach offers a number of advantages. Eulerian measurements are particularly useful for longer time scales, while the intensive Lagrangian observations and modelling over a few tides provide the opportunity to obtain and analyse results across multiple length-scales. The results presented within this thesis offer insights into the complexities of modelling turbulence and hydrodynamics along the fluvial-to-marine transition zone and the associated influences on sediment transport in these regions.

Appendices

Chapter A

Model sensitivity analysis and validation for Chapter 2

A.1 Sensitivity analysis

A sensitivity analysis was performed on the grid refinement. We note that the most refined model would take around 215 days to run, which is not practical. We therefore concluded that our current model refinement was satisfactory, both in terms of running time and RMSE (Table A.1).

Table A.1: Sensitivity analysis on grid refinement.

	Vertical	Along-stream	Across-stream	RMSE (middle site)			Rough running time
				Water level (m)	U_m $(m.s^{-1})$	V_m $(m.s^{-1})$	
Unrefined H	20	3,386	26	1.7970	0.2392	0.0036	7 days
Unrefined V	10	6,770	50	0.2103	0.015	0.00079	20 days
Current model	20	6,770	50	0.232	0.024	0.002	36 days
Refined	20	13,358	90	-	-	-	214.5 days

A.2 Model validation

In order to validate further our modelling, we conducted a comparison of predictions by Delft3D with laboratory observations. To do so, we created a Delft3D model to reproduce numerically the flume experiment conducted by Blanckaert (2009). The grid was created so that the aspect ratios (horizontal to vertical) were close to those used in the Kaipara model of the present paper

(Table A.2, Figure A.1a).

A schematic of the grid is given in Figure A.1a. The depth-average streamwise and transverse velocity along the centreline of the channel predicted by Delft3D show good agreement with the observations made by Blanckaert (2009), despite an overall slight under-prediction (Figures A.1h-k and A.2). The RMSE between the model predictions and the observations made by Blanckaert (2009) are also presented in Table A.3 and Table A.4. Our results align well with previous RANS-based modelling of the laboratory experiments of Blanckaert (2009); in particular the detailed comparisons made by Zeng et al. (2008). The model captures the broad distribution and magnitudes of streamwise velocity within the bend and the shifting of flow maximum towards the outer bend (see cross sections in Figure A.2 and corresponding RMSE in Table A.5). However, as also observed in Zeng et al. (2008), our model cannot reproduce the streamwise vortices and secondary flow maximum near the inner bank.

Our model captures production of turbulent kinetic energy as the flow enters bend; however, while patterns are reproduced, the model tends to overestimate the turbulent kinetic energy, especially inside the sharp bend (e.g., cross-sections at 120° and 150°, Figures A.3b, f and c, g and Table A.5). Given the aim of the present study is to assess model performance against Lagrangian observations in a natural river (in which bends are not as strongly curved as the validation case), we conclude that while some discrepancies remain, model performance is sufficiently satisfactory for this purpose.

Table A.2: Comparison of grid cell sizes.

	Model after Blanckaert (2009)		Kaipara Model	
	Number of cells	Average size (m)	Number of cells	Average size (m)
Vertical	20	7×10^{-3}	20	0.225
Along-stream	239	0.067	6770	2.4
Across-stream	20	0.065	50	2.1

Table A.3: RMSE from the vertical profiles of the normalized streamwise velocity between the observations made by Blanckaert (2009) and Delft3D predictions.

RMSE	Inflow	Bend entrance	Bend exit	Averaged over bend	Outflow
v_s/U_s [-]	0.1909	0.1364	0.1546	-	0.2217
$(v_n - U_n)/U$ [-]	-	-	0.9533	0.9879	-
$k/u^2_{*,0}$ [-]	0.3830	-	-	0.3711	-

Table A.4: RMSE of streamwise distribution along the centreline between the observations made by Blanckaert (2009) and Delft3D predictions.

RMSE	Streamwise distribution	Figures compared
U_s/U [-]	0.0034	A1h and A1i
U_n/U [-]	0.0022	A1j and A1k
$v^2_s/u^2_{*,0}$ [-]	0.2119	A1l and A1m
$v^2_n/u^2_{*,0}$ [-]	0.0350	A1l and A1m

Table A.5: RMSE of cross-sectional distribution of normalised streamwise velocity and normalised turbulent kinetic energy between the observations made by Blanckaert (2009) and Delft3D predictions.

RMSE	Normalised streamwise velocity	Normalised turbulent kinetic energy
Cross-section 30°	0.0663	0.3829
Cross-section 120°	0.0452	0.3744
Cross-section 150°	0.0431	0.3763
Cross-section downstream	0.0513	0.3506

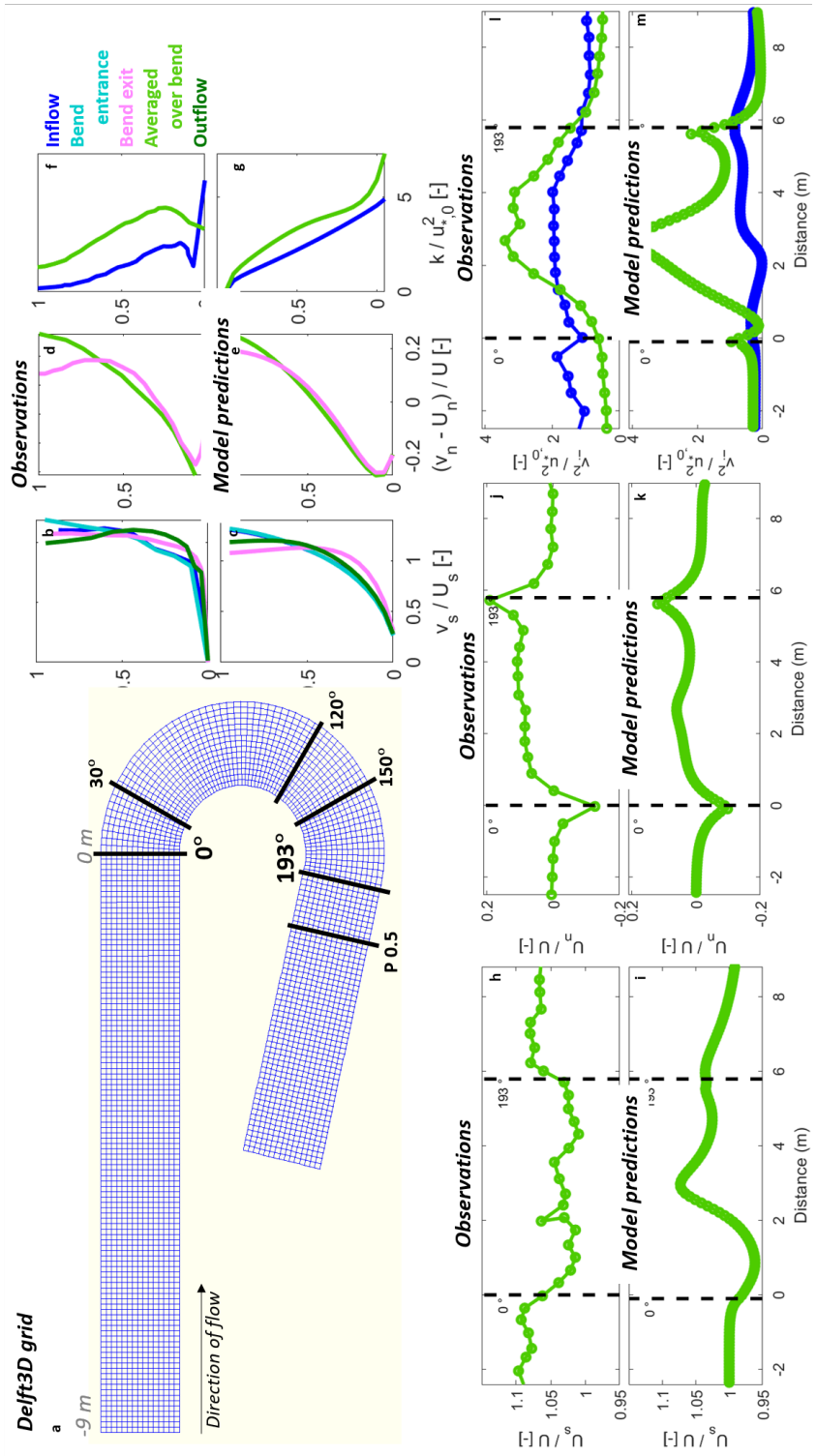

Figure A.1: (a) Model grid developed by Delft3D. Comparison of vertical profiles of the normalized streamwise velocity (b, d, f) observed by Blanckaert (2009) with (c, e, g) the results predicted by Delft3D, respectively. Comparison of the streamwise distribution along the centreline of (h, j, l) the depth-averaged streamwise velocity normalized with the cross-sectional averaged streamwise velocity, the normalized depth-averaged transverse velocity and the normalized depth-averaged turbulent normal stresses observed by Blanckaert (2009) with (i, k, l) the results predicted by Delft3D, respectively.

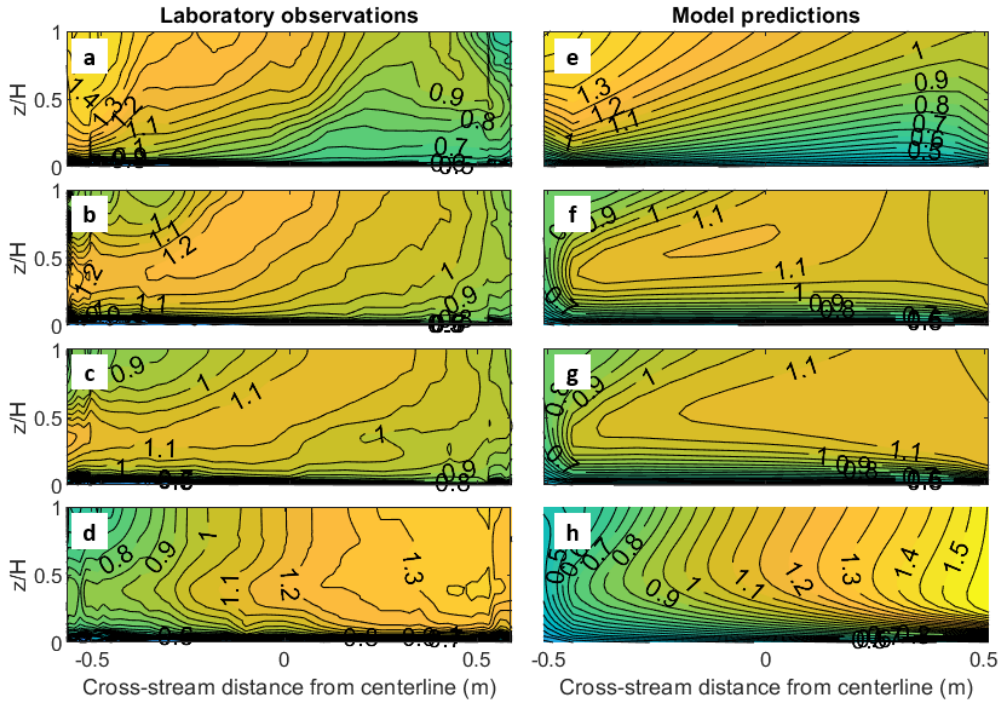

Figure A.2: Observations (left) and model predictions (right) of the cross-sectional distribution of the normalised streamwise velocity at (a, b) 30°, (c, d) 120°, (e, f) 150° and (g, h) further downstream (location P 0.5, see Figure 13 a).

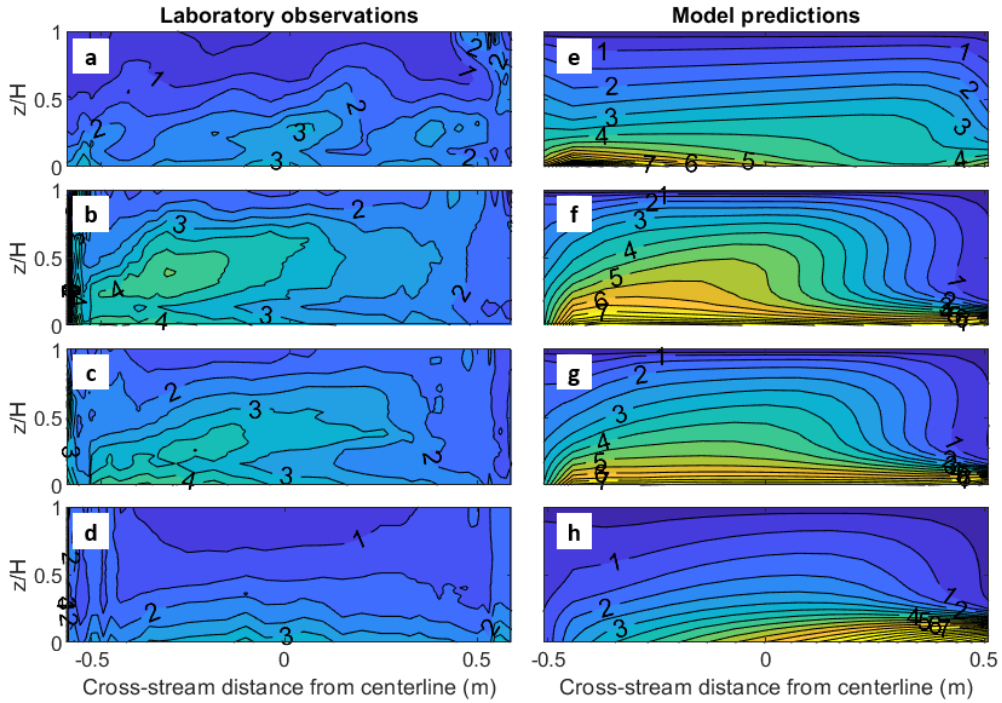

Figure A.3: Observations (left) and model predictions (right) of the cross-sectional distribution of the normalised turbulent kinetic energy at (a, b) 30°, (c, d) 120°, (e, f) 150° and (g, h) further downstream (location P 0.5, see Figure 13 a).

Chapter B

Root Mean Squared Error statistics for model calibration in Chapter 4

The Root Mean Squared Errors for horizontal flow speeds and dissipation rates of turbulent kinetic energy quantifying the calibration of the model for the 6 numerical simulations in Chapter 4 are shown in Table B.1.

Table B.1: Root Mean Square Errors (RMSE) for speed and $\log_{10}(\epsilon)$ between the observations and the model predictions by the k-ϵ and k-L turbulence closure schemes for the three cases (all drifters, all days).

Turbulence closure scheme	Case	Processes	RMSE speed ($m.s^{-1}$)
k-ϵ	Case 1	Mobile bed	0.1304
	Case 2	Sediment input	0.1401
	Case 3	Mobile bed + Sediment input	0.1288
k-L	Case 4	Mobile bed	0.1390
	Case 5	Sediment input	0.1365
	Case 6	Mobile bed + Sediment input	0.1260
Turbulence closure scheme	Case	Processes	RMSE $\log_{10}(\epsilon)$ ($m^2.s^{-3}$)
k-ϵ	Case 1	Mobile bed	0.5325
	Case 2	Sediment input	0.6317
	Case 3	Mobile bed + Sediment input	0.5335
k-L	Case 4	Mobile bed	0.5932
	Case 5	Sediment input	0.6449
	Case 6	Mobile bed + Sediment input	0.5362

References

Abad, J. D. and M. H. Garcia (2009). Experiments in a high-amplitude kinoshita meandering channel: 1. Implications of bend orientation on mean and turbulent flow structure. *Water Resources Research 45*(2).

Abad, J. D., B. L. Rhoads, İ. Güneralp, and M. H. García (2008). Flow structure at different stages in a meander-bend with bendway weirs. *Journal of Hydraulic Engineering 134*(8), 1052–1063.

Amoudry, L. and A. Souza (2010). Influence of turbulence closure on estuarine sediment dynamics and morphodynamics. *Coastal Engineering Proceedings* (32), 78–78.

Amoudry, L. O. and A. J. Souza (2011). Impact of sediment-induced stratification and turbulence closures on sediment transport and morphological modelling. *Continental Shelf Research 31*(9), 912–928.

Bhuiyan, M. J. A. N. and D. Dutta (2012). Assessing impacts of sea level rise on river salinity in the Gorai river network, Bangladesh. *Estuarine, Coastal and Shelf Science 96*, 219–227.

Blanckaert, K. (2009). Saturation of curvature-induced secondary flow, energy losses, and turbulence in sharp open-channel bends: Laboratory experiments, analysis, and modeling. *Journal of Geophysical Research: Earth Surface 114*(F3).

Blanckaert, K. (2010). Topographic steering, flow recirculation, velocity redis-

tribution, and bed topography in sharp meander bends. *Water Resources Research 46*(9).

Blanckaert, K. (2011). Hydrodynamic processes in sharp meander bends and their morphological implications. *Journal of Geophysical Research: Earth Surface 116*(F1).

Blanckaert, K. and H. J. De Vriend (2004). Secondary flow in sharp open-channel bends. *Journal of Fluid Mechanics 498*, 353–380.

Blanckaert, K. and H. J. De Vriend (2010). Meander dynamics: A nonlinear model without curvature restrictions for flow in open-channel bends. *Journal of Geophysical Research: Earth Surface 115*(F4).

Blanckaert, K., A. Duarte, Q. Chen, and A. J. Schleiss (2012). Flow processes near smooth and rough (concave) outer banks in curved open channels. *Journal of Geophysical Research: Earth Surface 117*(F4).

Blanckaert, K. and W. H. Graf (2001). Mean flow and turbulence in open-channel bend. *Journal of Hydraulic Engineering 127*(10), 835–847.

Blanckaert, K. and W. H. Graf (2004). Momentum transport in sharp open-channel bends. *Journal of Hydraulic Engineering 130*(3), 186–198.

Bomers, A., R. M. J. Schielen, and S. J. Hulscher (2019). The influence of grid shape and grid size on hydraulic river modelling performance. *Environmental Fluid Mechanics 19*(5), 1273–1294.

Braithwaite, K., D. Bowers, W. Nimmo Smith, and G. Graham (2012). Controls on floc growth in an energetic tidal channel. *Journal of Geophysical Research: Oceans 117*(C2).

Broomans, P. (2003). Numerical accuracy in solutions of the shallow-water equations. *Master of science dissertation, Technical University of Delft*.

Burchard, H. and K. Bolding (2001). Comparative analysis of four second-moment turbulence closure models for the oceanic mixed layer. *Journal of Physical Oceanography 31*(8), 1943–1968.

Burchard, H., P. D. Craig, J. R. Gemmrich, H. van Haren, P.-P. Mathieu, H. M. Meier, W. A. M. N. Smith, H. Prandke, T. P. Rippeth, E. D. Skyllingstad, et al. (2008). Observational and numerical modeling methods for quantifying coastal ocean turbulence and mixing. *Progress in Oceanography 76*(4), 399–442.

Burchard, H. and O. Petersen (1999). Models of turbulence in the marine environment — A comparative study of two-equation turbulence models. *Journal of Marine Systems 21*(1), 29–53.

Burchard, H., O. Petersen, and T. P. Rippeth (1998). Comparing the performance of the Mellor-Yamada and the k-ε two-equation turbulence models. *Journal of Geophysical Research: Oceans 103*(C5), 10543–10554.

Chao, S.-Y. (1988). Wind-driven motion of estuarine plumes. *Journal of Physical Oceanography 18*(8), 1144–1166.

Charria, G., P. Lazure, B. Le Cann, A. Serpette, G. Reverdin, S. Louazel, F. Batifoulier, F. Dumas, A. Pichon, and Y. Morel (2013). Surface layer circulation derived from Lagrangian drifters in the Bay of Biscay. *Journal of Marine Systems 109*, S60–S76.

Cheikh, M. I. and M. Momen (2020). The interacting effects of storm surge intensification and sea-level rise on coastal resiliency: a high-resolution turbulence resolving case study. *Environmental Research Communications 2*(11), 115002.

Chiari, M. and D. Rickenmann (2011). Back-calculation of bedload transport in steep channels with a numerical model. *Earth Surface Processes and Landforms 36*(6), 805–815.

Church, J. A. and N. J. White (2006). A 20th century acceleration in global sea-level rise. *Geophysical Research Letters 33*(1).

Church, M. (2006). Bed material transport and the morphology of alluvial river channels. *Annual Review of Earth and Planetary Sciences 34*, 325–354.

Church, M. (2007). 1 Multiple scales in rivers. *Developments in Earth Surface Processes 11*, 3–28.

Coufort, C., D. Bouyer, and A. Liné (2005). Flocculation related to local hydrodynamics in a Taylor–Couette reactor and in a jar. *Chemical Engineering Science 60*(8), 2179 – 2192. 5th International Symposium on Mixing in Industrial Processes (ISMIP5).

Craig, P. D. and M. L. Banner (1994). Modeling wave-enhanced turbulence in the ocean surface layer. *Journal of Physical Oceanography 24*(12), 2546–2559.

Dade, W. B. and P. F. Friend (1998). Grain-size, sediment-transport regime, and channel slope in alluvial rivers. *The Journal of Geology 106*(6), 661–676.

Davies, J. (1964). A morphogenic approach to world shorelines. *Zeitschrift fur Geomorphologie 8*, 127–142.

Davis, R. E. (1985). Drifter observations of coastal surface currents during CODE: The method and descriptive view. *Journal of Geophysical Research: Oceans 90*(C3), 4741–4755.

de Almeida, J. R. M. and J. J. Ota (2020). Comparative study between turbulence models in curved channels. *Brazilian Journal of Water Resources 25*.

Dejeans, B. S., J. C. Mullarney, and I. T. MacDonald. Evaluation of the performance of two turbulence closure schemes in a Lagrangian frame of reference along a fluvial-to-marine transition zone.

Dejeans, B. S., J. C. Mullarney, and I. T. MacDonald (2022). Lagrangian observations and modelling of turbulence along a tidally influenced river. *Water Resources Research e2020WR027894*, 21.

Dejeans, B. S., J. C. Mullarney, I. T. MacDonald, and G. M. Reeve (2017). Assessment of the performance of a turbulence closure model: along the tidally-influenced Kaipara River to the estuary, NZ. *Australasian Coasts & Ports 2017: Working with Nature*, 351.

Deltares, H. (2020). Delft3D-FLOW user manual. Technical report.

Demuren, A. and W. Rodi (1986). Calculation of flow and pollutant dispersion in meandering channels. *Journal of Fluid Mechanics 172*, 63–92.

Denman, K. (1973). A time-dependent model of the upper ocean. *Journal of Physical Oceanography 3*(2), 173–184.

Dyer, K. (1989). Sediment processes in estuaries: future research requirements. *Journal of Geophysical Research: Oceans 94*(C10), 14327–14339.

Eisma, D., P. Bernard, G. Cadée, V. Ittekkot, J. Kalf, R. Laane, J. Martin, W. Mook, A. Van Put, and T. Schuhmacher (1991a). Suspended-matter particle size in some West-European estuaries; part II: A review on floc formation and break-up. *Netherlands Journal of Sea Research 28*(3), 215–220.

Eisma, D., P. Bernard, G. Cadee, V. Ittekkot, J. Kalf, R. Laane, J. M. Martin, W. Mook, A. Van Put, and T. Schuhmacher (1991b). Suspended-matter particle size in some West-European estuaries; part I: Particle-size distribution. *Netherlands Journal of Sea Research 28*(3), 193–214.

Eisma, D., J. Kalf, and M. Veenhuis (1980). The formation of small particles and aggregates in the Rhine estuary. *Netherlands Journal of Sea Research 14*(2), 172–191.

Elias, E., D. Walstra, J. Roelvink, M. Stive, and M. Klein (2001). Hydrodynamic validation of Delft3D with field measurements at Egmond. In *Coastal Engineering 2000*, pp. 2714–2727.

Elliott, M. and V. Quintino (2007). The estuarine quality paradox, environmental homeostasis and the difficulty of detecting anthropogenic stress in naturally stressed areas. *Marine Pollution Bulletin 54*(6), 640–645.

Engel, F. L. and B. L. Rhoads (2017). Velocity profiles and the structure of turbulence at the outer bank of a compound meander bend. *Geomorphology 295*, 191–201.

Feddersen, F., J. H. Trowbridge, and A. Williams III (2007). Vertical structure of dissipation in the nearshore. *Journal of Physical Oceanography 37*(7), 1764–1777.

Ferziger, J. H., M. Perić, and R. L. Street (2002). *Computational methods for fluid dynamics*, Volume 3. Springer.

Fischer-Antze, T., N. Rüther, N. R. Olsen, and D. Gutknecht (2009). Three-dimensional (3D) modeling of non-uniform sediment transport in a channel bend with unsteady flow. *Journal of Hydraulic Research 47*(5), 670–675.

Franca, M. J. and M. Brocchini (2015). Turbulence in rivers. In *Rivers–Physical, Fluvial and Environmental Processes*, pp. 51–78. Springer.

Fuentes-Pérez, J. F., F. J. Sanz-Ronda, and J. A. Tuhtan (2022). An open surface drifter for river flow field characterization. *Sensors 22*(24), 9918.

Fuhrman, D. R., M. Dixen, and N. G. Jacobsen (2010). Physically-consistent wall boundary conditions for the k-ω turbulence model. *Journal of Hydraulic Research 48*(6), 793–800.

Gehrels, W. R., B. W. Hayward, R. M. Newnham, and K. E. Southall (2008). A 20th century acceleration of sea-level rise in New Zealand. *Geophysical Research Letters 35*(2).

Gholami, A., A. Akbar Akhtari, Y. Minatour, H. Bonakdari, and A. A. Javadi (2014). Experimental and numerical study on velocity fields and water surface profile in a strongly-curved 90 open channel bend. *Engineering Applications of Computational Fluid Mechanics 8*(3), 447–461.

Grady, A., L. Moore, C. D. Storlazzi, E. Elias, and M. Reidenbach (2013). The influence of sea level rise and changes in fringing reef morphology on gradients in alongshore sediment transport. *Geophysical Research Letters 40*(12), 3096–3101.

Haggitt, T., S. T. Mead, and M. Bellingham (2008). *Review of environmental information on the Kaipara Harbour marine environment.* Auckland Regional Council.

Harrison, E. T., R. H. Norris, and S. N. Wilkinson (2007). The impact of fine sediment accumulation on benthic macroinvertebrates: implications for river management. In *Proceedings of the 5th Australian Stream Management Conference*, pp. 139–144. Charles Sturt University Thurgoona, New South Wales, Australia.

Heath, R. (1975). Stability of some New Zealand coastal inlets. *New Zealand Journal of Marine and Freshwater Research 9*(4), 449–457.

Hedges, J. I. and R. G. Keil (1995). Sedimentary organic matter preservation: an assessment and speculative synthesis. *Marine chemistry 49*(2-3), 81–115.

Heer, T., M. G. Wells, P. R. Jackson, and N. E. Mandrak (2020). Modelling grass carp egg transport using a 3-d hydrodynamic river model: the role of egg retention in dead zones on spawning success. *Canadian Journal of Fisheries and Aquatic Sciences 77*(8), 1379–1392.

Hill, K., T. Dauphinee, and D. Woods (1986). The extension of the Practical Salinity Scale 1978 to low salinities. *IEEE Journal of Oceanic Engineering 11*(1), 109–112.

Hong, B., Z. Liu, J. Shen, H. Wu, W. Gong, H. Xu, and D. Wang (2020). Potential physical impacts of sea-level rise on the Pearl River Estuary, China. *Journal of Marine Systems 201*, 103245.

Horstman, E., M. Dohmen-Janssen, and S. Hulscher (2013). Modeling tidal dynamics in a mangrove creek catchment in Delft3D. In *Coastal dynamics*, Volume 2013, pp. 833–844.

Hung, M., T. Hsieh, C. Wu, J. Yang, et al. (2009). Two-dimensional nonequilibrium noncohesive and cohesive sediment transport model. *Journal of Hydraulic Engineering-ASCE 135*(5), 369–382.

Hut, R., T. Thatoe Nwe Win, and T. Bogaard (2020). Easy to build low-power gps drifters with local storage and a cellular modem made from off-the-shelf components. *Geoscientific Instrumentation, Methods and Data Systems 9*(2), 435–442.

Hyland, J. L., R. F. Van Dolah, and T. R. Snoots (1999). Predicting stress in benthic communities of southeastern US estuaries in relation to chemical contamination of sediments. *Environmental Toxicology and Chemistry: An International Journal 18*(11), 2557–2564.

James, S. C., C. A. Jones, M. D. Grace, and J. D. Roberts (2010). Advances in sediment transport modelling. *Journal of Hydraulic Research 48*(6), 754–763.

Johnson, A. C., M. C. Acreman, M. J. Dunbar, S. W. Feist, A. M. Giacomello, R. E. Gozlan, S. A. Hinsley, A. T. Ibbotson, H. P. Jarvie, J. I. Jones, et al. (2009). The British river of the future: how climate change and human activity might affect two contrasting river ecosystems in England. *Science of the Total Environment 407*(17), 4787–4798.

Johnson, D., R. Stocker, R. Head, J. Imberger, and C. Pattiaratchi (2003). A compact, low-cost GPS drifter for use in the oceanic nearshore zone, lakes,

and estuaries. *Journal of Atmospheric and Oceanic Technology 20*(12), 1880–1884.

Khanarmuei, M., K. Suara, and R. J. Brown (2019). Calibration and assimilation in hydrodynamic model of a micro-tidal estuary and comparison with Lagrangian drifter data. In *E-Proceedings of the 38th IAHR World Congress*, pp. 6359–6368. International Association for Hydro-Environment Engineering and Research (IAHR).

Khanarmuei, M., K. Suara, J. Sumihar, and R. J. Brown (2020). Hydrodynamic modelling and model sensitivities to bed roughness and bathymetry offset in a micro-tidal estuary. *Journal of Hydroinformatics 22*(6), 1536–1553.

Khelifa, A. and P. S. Hill (2006). Models for effective density and settling velocity of flocs. *Journal of Hydraulic Research 44*(3), 390–401.

Kim, J. S., D. Baek, and I. Park (2020). Evaluating the impact of turbulence closure models on solute transport simulations in meandering open channels. *Applied Sciences 10*(8), 2769.

Knox, J. C. (2000). Sensitivity of modern and Holocene floods to climate change. *Quaternary Science Reviews 19*(1-5), 439–457.

Koken, M., G. Constantinescu, and K. Blanckaert (2013). Hydrodynamic processes, sediment erosion mechanisms, and Reynolds-number-induced scale effects in an open channel bend of strong curvature with flat bathymetry. *Journal of Geophysical Research: Earth Surface 118*(4), 2308–2324.

Kraft, S., Y. Wang, and M. Oberlack (2011). Large eddy simulation of sediment deformation in a turbulent flow by means of level-set method. *Journal of Hydraulic Engineering 137*(11), 1394–1405.

Kraus, E. and J. Turner (1967). A one-dimensional model of the seasonal

thermocline II. the general theory and its consequences. *Tellus 19*(1), 98–106.

Kumar, R. G., K. B. Strom, and A. Keyvani (2010). Floc properties and settling velocity of San Jacinto estuary mud under variable shear and salinity conditions. *Continental Shelf Research 30*(20), 2067–2081.

Lai, Y. G. and K. Wu (2019). A three-dimensional flow and sediment transport model for free-surface open channel flows on unstructured flexible meshes. *Fluids 4*(1), 18.

Launder, B., A. Morse, W. Rodi, and D. Spalding (1973). Prediction of free shear flows: a comparison of the performance of six turbulence models. *NASA. Langley Res. Center Free Turbulent Shear Flows, Vol. 1*.

Lhermitte, R. and R. Serafin (1984). Pulse-to-pulse coherent doppler sonar signal processing techniques. *Journal of Atmospheric and Oceanic Technology 1*(4), 293–308.

Li, W., J. Zhu, L. Fu, Q. Zhu, Y. Guo, and Y. Gong (2021). A rapid 3D reproduction system of dam-break floods constrained by post-disaster information. *Environmental Modelling & Software 139*, 104994.

Lohrmann, A., B. Hackett, and L. P. Røed (1990). High resolution measurements of turbulence, velocity and stress using a pulse-to-pulse coherent sonar. *Journal of Atmospheric and Oceanic Technology 7*(1), 19–37.

MacDonald, I. T. and J. C. Mullarney (2015). A novel "FlocDrifter" platform for observing flocculation and turbulence processes in a Lagrangian frame of reference. *Journal of Atmospheric and Oceanic Technology 32*(3), 547–561.

Manning, A. and K. Dyer (1999). A laboratory examination of floc characteristics with regard to turbulent shearing. *Marine Geology 160*(1-2), 147–170.

Mardani, N., K. Suara, H. Fairweather, R. Brown, A. McCallum, and R. C.

Sidle (2020). Improving the accuracy of hydrodynamic model predictions using Lagrangian calibration. *Water 12*(2), 575.

Maurizi, A., A. Griffa, P.-M. Poulain, and F. Tampieri (2004). Lagrangian turbulence in the Adriatic Sea as computed from drifter data: Effects of inhomogeneity and nonstationarity. *Journal of Geophysical Research: Oceans 109*(C4).

McCave, I. (1984). Size spectra and aggregation of suspended particles in the deep ocean. *Deep Sea Research Part A. Oceanographic Research Papers 31*(4), 329–352.

McPhaden, M., D. Hansen, and P. Richardson (1991). A comparison of ship drift, drifting buoy, and current meter mooring velocities in the Pacific South equatorial current. *Journal of Geophysical Research: Oceans 96*(C1), 775–781.

Meybeck, M. and C. Vörösmarty (2005). Fluvial filtering of land-to-ocean fluxes: from natural Holocene variations to Anthropocene. *Comptes Rendus Geoscience 337*(1-2), 107–123.

Miah, M. Y., M. Mannan, K. Quddus, M. Mahmud, and T. Baida (2004). Salinity on cultivable land and its effects on crops. *Pakistan Journal of Biological Sciences (Pakistan)*.

Mietta, F., C. Chassagne, A. J. Manning, and J. C. Winterwerp (2009). Influence of shear rate, organic matter content, pH and salinity on mud flocculation. *Ocean Dynamics 59*, 751–763.

Milliman, J. D. and R. H. Meade (1983). World-wide delivery of river sediment to the oceans. *The Journal of Geology 91*(1), 1–21.

Moshonkin, S., V. Zalesny, and A. Gusev (2018). Simulation of the Arctic—North Atlantic ocean circulation with a two-equation k-omega turbu-

lence parameterization. *Journal of Marine Science and Engineering 6*(3), 95.

Mosselman, E. (2012). Modelling sediment transport and morphodynamics of gravel-bed rivers. In *Gravel-bed rivers: Processes, Tools, Environments*, pp. 101–115. John Wiley & Sons.

Mullarney, J. C. and S. M. Henderson (2012). Lagrangian measurements of turbulent dissipation over a shallow tidal flat from pulse coherent Acoustic Doppler Profilers. *Coastal Engineering Proceedings*, 1 (33).

Mullarney, J. C. and S. M. Henderson (2013). A novel drifter designed for use with a mounted Acoustic Doppler Current Profiler in shallow environments. *Limnology and Oceanography: Methods 11*(8), 438–449.

Nakanish, M. (2001). Improvement of the Mellor-Yamada turbulence closure model based on large-eddy simulation data. *Boundary-Layer Meteorology 99*(3), 349–378.

Odgaard, A. J. and M. A. Bergs (1988). Flow processes in a curved alluvial channel. *Water Resources Research 24*(1), 45–56.

Ottevanger, W., K. Blanckaert, and W. S. Uijttewaal (2012). Processes governing the flow redistribution in sharp river bends. *Geomorphology 163*, 45–55.

Papanicolaou, A. T. N., M. Elhakeem, G. Krallis, S. Prakash, and J. Edinger (2008). Sediment transport modeling review—current and future developments. *Journal of hydraulic engineering 134*(1), 1–14.

Parsapour-Moghaddam, P. and C. Rennie (2017). Hydrostatic versus nonhydrostatic hydrodynamic modelling of secondary flow in a tortuously meandering river: Application of Delft3D. *River Research and Applications 33*(9), 1400–1410.

Pascal, R. W., M. J. Yelland, M. A. Srokosz, B. I. Moat, E. M. Waugh, D. H. Comben, A. G. Cansdale, M. C. Hartman, D. G. Coles, P. Chang Hsueh, et al. (2011). A spar buoy for high-frequency wave measurements and detection of wave breaking in the open ocean. *Journal of Atmospheric and Oceanic Technology 28*(4), 590–605.

Postacchini, M., L. R. Centurioni, L. Braasch, M. Brocchini, and D. Vicinanza (2015). Lagrangian observations of waves and currents from the river drifter. *IEEE Journal of Oceanic Engineering 41*(1), 94–104.

Puleo, J. A., O. Mouraenko, and D. M. Hanes (2004). One-dimensional wave bottom boundary layer model comparison: specific eddy viscosity and turbulence closure models. *Journal of waterway, port, coastal, and ocean engineering 130*(6), 322–325.

Putzu, S., F. Enrile, G. Besio, A. Cucco, L. Cutroneo, M. Capello, and A. Stocchino (2019). A reasoned comparison between two hydrodynamic models: Delft3D-Flow and ROMS (Regional Oceanic Modelling System). *Journal of Marine Science and Engineering 7*(12), 464.

Rahuel, J., F. Holly, J. Chollet, P. Belleudy, and G. Yang (1989). Modeling of riverbed evolution for bedload sediment mixtures. *Journal of Hydraulic Engineering 115*(11), 1521–1542.

Ralston, D. K., G. W. Cowles, W. R. Geyer, and R. C. Holleman (2017). Turbulent and numerical mixing in a salt wedge estuary: Dependence on grid resolution, bottom roughness, and turbulence closure. *Journal of Geophysical Research: Oceans 122*(1), 692–712.

Rameshwaran, P. and P. Naden (2004). Three-dimensional modelling of free surface variation in a meandering channel. *Journal of Hydraulic Research 42*(6), 603–615.

Rijn, L. C. v. (1984). Sediment transport, part II: Suspended load transport. *Journal of Hydraulic Engineering 110*(11), 1613–1641.

Roelvink, J. and G. Van Banning (1995). Design and development of Delft3D and application to coastal morphodynamics. *Oceanographic Literature Review 11*(42), 925.

Roy, N. and R. Sinha (2014). Effective discharge for suspended sediment transport of the Ganga River and its geomorphic implication. *Geomorphology 227*, 18–30.

Sabet, B. S. and G. A. Barani (2011). Design of small GPS drifters for current measurements in the coastal zone. *Ocean & Coastal Management 54*(2), 158–163.

Safak, I., M. Allison, and A. Sheremet (2013). Floc variability under changing turbulent stresses and sediment availability on a wave energetic muddy shelf. *Continental Shelf Research 53*, 1–10.

Sander, J. (1998). Dynamical equations and turbulent closures in geophysics. *Continuum Mechanics and Thermodynamics 10*(1), 1–28.

Schmidt, W., B. Woodward, K. Millikan, R. Guza, B. Raubenheimer, and S. Elgar (2003). A GPS-tracked surf zone drifter. *Journal of Atmospheric and Oceanic Technology 20*(7), 1069–1075.

Scotti, A. (2010). Large eddy simulation in the ocean. *International Journal of Computational Fluid Dynamics 24*(10), 393–406.

Shenliang, C., Z. Guoan, and Y. Shilun (2003). Temporal and spatial changes of suspended sediment concentration and resuspension in the Yangtze River estuary. *Journal of Geographical Sciences 13*, 498–506.

Shih, L. H., J. R. Koseff, J. H. Ferziger, and C. R. Rehmann (2000). Scaling and parameterization of stratified homogeneous turbulent shear flow. *Journal of Fluid Mechanics 412*, 1–20.

Shuai, S. and R. K. Agarwal (2019). A one-equation turbulence model based on k-kl closure. In *AIAA Scitech 2019 Forum*, pp. 1879.

Siviglia, A. and A. Crosato (2016). Numerical modelling of river morphodynamics: Latest developments and remaining challenges. *Advances in Water Resources 93*(Part A), 1–3.

Spencer, D., C. Lemckert, Y. Yu, J. Gustafson, S. Lee, and H. Zhang (2014). Quantifying dispersion in an estuary: A Lagrangian drifter approach. *Journal of Coastal Research* (70), 29–34.

Stockdale, R., S. McLelland, R. Middleton, and T. Coulthard (2008). Measuring river velocities using GPS river flow tracers (GRiFTers). *Earth Surface Processes and Landforms 33*(8), 1315–1322.

Suara, K. A., H. Wang, H. Chanson, B. Gibbes, and R. J. Brown (2018). Response of GPS-tracked drifters to wind and water currents in a tidal estuary. *IEEE Journal of Oceanic Engineering 44*(4), 1077–1089.

Sukhodolov, A. N. (2012). Structure of turbulent flow in a meander bend of a lowland river. *Water Resources Research 48*(1).

Sutherland, J., A. Peet, and R. Soulsby (2004). Evaluating the performance of morphological models. *Coastal Engineering 51*(8-9), 917–939.

Symonds, A. M., T. Vijverberg, S. Post, B.-J. Van Der Spek, J. Henrotte, and M. Sokolewicz (2016). Comparison between Mike 21 FM, Delft3D and Delft3D FM flow models of western Port Bay, Australia. *Coastal Engineering 2*, 1–12.

Taye, J. and B. Kumar (2022). Hydrodynamics and turbulence anisotropy for complex flow in a sinuous channel. *Acta Geophysica 70*(5), 2269–2282.

Tennekes, H. and J. L. Lumley (1972). *A first course in turbulence*. MIT press.

Thomson, J. (2012). Wave breaking dissipation observed with "SWIFT" drifters. *Journal of Atmospheric and Oceanic Technology 29*(12), 1866–1882.

Thorpe, S. (1995). Dynamical processes of transfer at the sea surface. *Progress in Oceanography 35*(4), 315–352.

Tinka, A., M. Rafiee, and A. M. Bayen (2012). Floating sensor networks for river studies. *IEEE Systems Journal 7*(1), 36–49.

Ullmann, S. (2008). Three-dimensional computation of non-hydrostatic free-surface flows. *Delft University of Technology, Delft*.

Van Manh, N., N. V. Dung, N. N. Hung, M. Kummu, B. Merz, and H. Apel (2015). Future sediment dynamics in the Mekong Delta floodplains: Impacts of hydropower development, climate change and sea level rise. *Global and Planetary Change 127*, 22–33.

Van Sabben, A. (2010). Sharp bend flow: Comparison of Delft3D-FLOW with LES and measurements for sharp bends. *Master of Science Dissertation: Technical University of Delft*.

Vanoni, V. A. (1975). River dynamics. *Advances in Applied Mechanics 15*, 1–87.

Vieira, D. A. and W. Wu (2002). One-dimensional channel network model cche1d version 3.0: User's manual. *National Center for Computational Hydroscience and Engineering, University of Mississippi, Oxford, MS*.

Walling, D. (2006). Human impact on land–ocean sediment transfer by the world's rivers. *Geomorphology 79*(3-4), 192–216.

Walling, D. and D. Fang (2003). Recent trends in the suspended sediment loads of the world's rivers. *Global and Planetary Change 39*(1-2), 111–126.

Wang, S., Y. Yan, and Y. Li (2012). Spatial and temporal variations of suspended sediment deposition in the alluvial reach of the upper Yellow River from 1952 to 2007. *Catena 92*, 30–37.

Warner, J. C., C. R. Sherwood, H. G. Arango, and R. P. Signell (2005). Performance of four turbulence closure models implemented using a generic length scale method. *Ocean Modelling 8*(1-2), 81–113.

Whiting, P. J. and W. E. Dietrich (1993a). Experimental studies of bed topography and flow patterns in large-amplitude meanders: 1. Observations. *Water Resources Research 29*(11), 3605–3614.

Whiting, P. J. and W. E. Dietrich (1993b). Experimental studies of bed topography and flow patterns in large-amplitude meanders: 2. Mechanisms. *Water Resources Research 29*(11), 3615–3622.

Wijesekera, H., J. S. Allen, and P. Newberger (2003). Modeling study of turbulent mixing over the continental shelf: Comparison of turbulent closure schemes. *Journal of Geophysical Research: Oceans 108*(C3).

Wiles, P. J., T. P. Rippeth, J. H. Simpson, and P. J. Hendricks (2006). A novel technique for measuring the rate of turbulent dissipation in the marine environment. *Geophysical Research Letters 33*(21).

Wilson, C., P. Bates, and J.-M. Hervouet (2002). Comparison of turbulence models for stage-discharge rating curve prediction in reach-scale compound channel flows using two-dimensional finite element methods. *Journal of Hydrology 257*(1), 42 – 58.

Winterwerp, J. C. (1998). A simple model for turbulence induced flocculation of cohesive sediment. *Journal of Hydraulic Research 36*(3), 309–326.

Winterwerp, J. C. and W. G. van Kesteren (2004). Flocculation processes. In *Developments in Sedimentology*, Volume 56, pp. 87–119. Elsevier.

Wormleaton, P. R. and M. Ewunetu (2006). Three-dimensional k-ϵ numerical modelling of overbank flow in a mobile bed meandering channel with floodplains of different depth, roughness and planform. *Journal of Hydraulic Research 44*(1), 18–32.

Wu, W., W. Rodi, and T. Wenka (2000). 3D numerical modeling of flow and sediment transport in open channels. *Journal of Hydraulic Engineering 126*(1), 4–15.

Yokosi, S. (1967). The structure of river turbulence. *Bulletin of the Disaster Prevention Research Institute, Kyoto University 17(2)*(121).

Yuan, D., D. Yang, T. L. Wade, and Y. Qian (2001). Status of persistent organic pollutants in the sediment from several estuaries in China. *Environmental Pollution 114*(1), 101–111.

Zedel, L., A. E. Hay, R. Cabrera, and A. Lohrmann (1996). Performance of a single-beam pulse-to-pulse coherent Doppler profiler. *IEEE Journal of Oceanic Engineering 21*(3), 290–297.

Zeng, J., G. Constantinescu, K. Blanckaert, and L. Weber (2008). Flow and bathymetry in sharp open-channel bends: Experiments and predictions. *Water Resources Research 44*(9).

Zhang, E., H. H. Savenije, H. Wu, Y. Kong, and J. Zhu (2011). Analytical solution for salt intrusion in the Yangtze Estuary, China. *Estuarine, Coastal and Shelf Science 91*(4), 492–501.